A Study on Passive Methods of Vortex Induced Vibrations Suppression

by

Ricardo A. Galvao

Submitted to the Department of Aeronautics and Astronautics
in partial fulfillment of the requirements for the degree of

Master of Science in Aeronautics and Astronautics

at the

MASSACHUSETTS INSTITUTE OF TECHNOLOGY

June 2008

Author .....
Department of Aeronautics and Astronautics
May, 2008

Certified by .....
Michael S. Triantafyllou
Professor of Ocean Engineering, MIT
Thesis Supervisor

Accepted by .....
David Darmofal
Associate Prosessor of Aeronautics and Astronautics, MIT
Chairman, Department Committee on Graduate Students

A Study on Passive Methods of Vortex Induced Vibrations Suppression

by

Ricardo A. Galvao

Submitted to the Department of Aeronautics and Astronautics
on May, 2008, in partial fulfillment of the
requirements for the degree of
Master of Science in Aeronautics and Astronautics

Abstract

A number of engineering systems, including those found in offshore operations, are often affected by vortex-induced vibrations (VIV). This phenomenon is caused by the interaction between a structure and shed vortices which can result in large amplitude vibrations of the structure that may lead to severe damage over time. Repairs to these systems are costly and time-consuming. Significant effort has been expended to develop a means of eliminating the need of repairs from vibrations. An investigation was undertaken to find a method of suppressing vortex-induced vibrations of a cylinder in a fluid flow. Passive methods of altering the flow behavior around the structure to mitigate the hydrodynamic forces that cause VIV were considered. Structural enhancements to a cylinder were attempted to accomplish this goal. The study also aimed to reduce drag below that encountered for a bare cylinder in comparable flow in addition to reducing flow induced vibrations. A number of approaches attempted succeeded in accomplishing this goal.

Thesis Supervisor: Michael S. Triantafyllou
Title: Professor of Ocean Engineering, MIT

Acknowledgments

I am indebted to many people upon the culmination of my research efforts here at MIT.

My advisors, Professor Michael Triantafyllou and Professor Franz Hover, have been invaluable throughout my work. Their constant support and advice have shaped and driven my research efforts over the past year and a half. Their generosity of time and encouragement is greatly appreciated.

My research experience was greatly enhanced by the many people I interacted with each day at the MIT Towing Tank Lab. Jason Dahl has been of tremendous assistance in providing me with guidance and a wealth of knowledge. Additional members of the lab, current and former, who have become good friends and supported me through my endeavors include Brad Simpson, Stephen Licht, David Farrell and Evan Lee. A substantial thanks is owed to Rachel Price who served as a UROP in the lab during much of my time there. Her assistance in performing and setting up for experiments was incredibly helpful and is greatly appreciated. Thanks for the cookies!

My time at MIT was made more enjoyable by the many people I met and friends I have made over the past two years. I thank them for there friendship and comraderie.

A special thanks is extended to members of my family who have provided me with tremendous support and guidance long before coming to MIT. They have encouraged me to pursue my dreams and provided me with whatever assistance that they could. Who I have become has been greatly influenced by them.

My fiance is probably the person in my life who has most had to hear my complaints as I struggled to complete a problem set or worked late to stay on track with my research. Her encouragement allowed me to continue on through those tough times. I am excited to start a new chapter in my life with her by my side as I conclude my time at MIT.

Contents

List of Figures

List of Tables

Chapter 1

Introduction

The phenomenon of vortex induced vibrations, often referred to as VIV, has been studied extensively throughout centuries. This physical occurrence is the result of interactions between fluid flow and a submerged object. Understanding how to control these interactions is of great interest due their prevalent existence in many engineering systems. The fluid-structure interaction of interest in this thesis manifests itself as a vibration of the body which often results in costly damage to the system. As such, a means of suppressing VIV altogether and thus, eliminating all its consequences, is something that is eagerly sought. Much work has been completed in order to better understand and predict the effects of these interactions. However, despite the efforts of many researchers, much is still left to be investigated due to the the complexity of the problem.

1.1 Research Motivation

The consequences of VIV can be observed in many different applications ranging from "strumming" of power lines due to airflow, visible vibrations of pipes and cables immersed in water, all the way to the well-known and catastrophic failure of the Tacoma Narrows Bridge caused by the wind. A particular area of application for a solution to this problem is that of water immersed structures. Such systems often have low damping that allows for VIV to occur in a damaging manner. The problems

brought about by this reality are especially felt by companies exploring and extracting natural resources from deep-water reservoirs. The significance of this activity only continues to grow as the need for these resources expands rapidly. Conventional means of meeting demand are no longer sufficient making a method of safely and cost-effectively performing deep-water resource extraction crucial to meeting global long-term energy needs.

The particular object of interest in this research is a cylinder which serves as a model for many components used in offshore operations such as risers, towing and mooring lines. In particular, the riser is the pipeline connecting the wellhead embedded into the sea floor with the platform at the sea's surface. Ocean currents can lead to vortex-induced vibrations of this pipeline. Over time this motion will weaken the riser and ultimately cause fractures. Replacement of the pipeline is expensive and time consuming. Another factor to be considered is the drag force imparted on the pipeline which will cause it to flex along its length. Drilling must be suspended if the pipeline flexes severely enough, limiting the time available to pump oil. Therefore, it is desirable to address these issues and produce practical and viable solutions.

1.2 Vortex Induced Vibration Overview

Over a century ago, Lord Rayleigh observed that vortex induced vibrations of an immersed body occur in a plane normal to the direction of flow. This phenomenon is often observed for bluff bodies in flows and, as the name suggests, results in periodic movement of the body caused by vortex shedding. A body is referred to as being "bluff" if it experiences separated flow over most of its surface while immersed in a fluid stream. In particular, this results in two separate shear layers, one from either side of the body, with opposite directions of vorticity. This is an an unstable arrangement where perturbations in the system will cause the shear layer to "roll up" into the wake deficit behind the body and shed compact, well-defined regions of rotating flow. These regions, or vortices, are shed in a progression with alternating sign in a periodic fashion. This pattern is often referred to as the Von Kármán

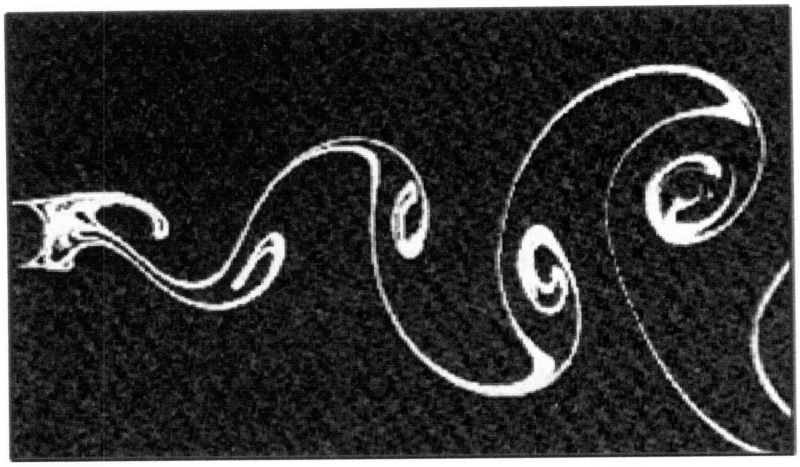

Figure 1-1: Image of typical Von Kármán Street shedding. Vortices of alternating rotation are show to shed periodically from the cylinder's surface and travel downstream. [28]

Street. Each time a vortex is shed from the cylinder, the pressure field around the body is altered causing a net moment to act on the cylinder with the same time-varying behavior as the shedding itself. This is the fundamental forcing mechanism for vibrations of a bluff body in a flow.

The behavior of a flow around a cylinder can be broken up into four regimes determined by the speed of the flow. A nondimensional parameter is used to characterize flow speed and is defined as

$$Re = \frac{UD}{\nu} \tag{1.1}$$

where U is the free stream velocity, D is a characteristic length such as a cylinder's diameter and ν is the dynamic viscosity of the fluid. Initially, at very low Reynolds number, Re ≤ 5, the flow resembles that of potential flow and remains attached to the cylinder surface producing a steady wake. Unfortunately, most natural flows due to not occur in this Reynolds number range. As we increase the Reynolds number, the wake becomes unstable and vortices begin shedding from the cylinder. This is followed by the subcritical regime where a transition begins to occur in the separated shear layers. Drag remains fairly independent of Reynolds number within this regime. Ultimately the critical regime is reached where a complete transition to turbulent flow

occurs at the boundary layer separation points with a minimal drag experienced in this stage. The boundary layer then becomes fully turbulent before separation as Reynolds number is increased further.

There are numerous dimensionless number used in literature when discussing VIV. Two such parameters used to characterize the phenomenon are Strouhal number (St) and Reynolds number (Re). The first of these two was named in honor of Vincenc Strouhal who studied vibrations of a wire in a free stream of air in the late 1800s. For a cylinder, the Strouhal number is defined as

$$St = \frac{f_s D}{U} \tag{1.2}$$

where f_s is the vortex shedding frequency, D is the cylinder diameter and U is the free stream velocity. It has been experimentally determined that the Strouhal number is relatively constant over a large range of Reynolds number. An additional parameter of significance is nominal reduced velocity which characterizes the fluid-structure coupling. This parameter is defined as

$$Vr = \frac{U}{f_n D} \tag{1.3}$$

where f_n is the natural frequency of the system.

A system will experience large amplitude vibrations when the frequency of vortex shedding is close to the natural frequency of the system. Vibrations can be sustained because the shedding behind an oscillating cylinder is similar to that which occurs from a stationary cylinder. However, one key component of VIV is that it is stable and self-limiting due to the counteraction of forcing by fluid damping. As a result, the amplitude of oscillations will usually not exceed by much the cylinder's diameter. Other fluid induced vibrations, such as galloping due to geometrical asymmetry, are unstable and can grow to catastrophic magnitudes.

For a situation in which a structure is allowed to vibrate in only the transverse direction, VIV can be modeled as a damped, one-degree of freedom spring mass system by

$$m\ddot{y} + b\dot{y} + ky = L \tag{1.4}$$

In such a setup, the system's natural frequency can be defined as

$$\omega_n = \sqrt{\frac{k}{m}} \tag{1.5}$$

where k is a stiffness coefficient and m is the mass of the system. It is important to remember that the total mass of a system submerged in a dense fluid, such as water, must also include an added mass contribution. During vibrations, the cylinder accelerates and results in a continually changing added mass contribution. This acceleration of surrounding fluid leads to a forcing of the cylinder that is in phase with the inertial forces and is aptly referred to as the added mass force.

From experiments, it has been determined that the motion and forcing of the cylinder can be described as a sinusoid in the following manner

$$y = A_y \sin(\omega t) \tag{1.6}$$

$$L = F_y \sin(\omega t + \phi) \tag{1.7}$$

where L can be broken down into the following two components

$$L = F_y \sin(\phi)\cos(\omega t) + F_y \cos(\phi)\sin(\omega t) \tag{1.8}$$

The first component of the lift force is in phase with the velocity of the structure, while the second is in phase with acceleration (added mass force). During higher amplitude VIV, this force is also in phase with motion. The phase between the added mass force and motion increases and leads to lower amplitude vibrations as flow speed is increased and vortex shedding transitions to a different pattern. Additional parameters of importance include amplitude ratio, frequency ratio, added mass ratio, drag coefficient and lift coefficient (Table 1.1). These are all measured parameters that are functions of Reynolds number [5]. Detailed reviews of VIV and derivation of

Reynolds Number	$Re = \frac{UD}{\nu}$	$\frac{InertialForce}{ViscousForce}$
Amplitude Ratio	$\frac{A_y}{D}$	$\frac{MotionAmplitude}{CylinderDiameter}$
Frequency Ratio	$\frac{\omega}{\omega_n}$	$\frac{ExcitationFrequency}{NaturalFrequency}$
Nominal Reduced Velocity	$V_r = \frac{U}{f_n D}$	$\frac{FreeStreamVelocity}{(NaturalFrequency)(CylinderDiameter)}$
Added Mass Ratio	$C_m = \frac{m_a}{\rho\pi\frac{D^2}{4}S}$	$\frac{EffectiveAddedMass}{DisplacedFluidMass}$
Drag Coefficient	$C_D = \frac{F_x}{\frac{1}{2}\rho U^2 DS}$	$\frac{DragForce}{(StagnationPressure)(ProjectedArea)}$
Lift Coefficient	$C_L = \frac{F_y}{\frac{1}{2}\rho U^2 DS}$	$\frac{LiftForce}{(StagnationPressure)(ProjectedArea)}$

Table 1.1: Non-dimensional parameters related to VIV.

related equations can be found in Sarpkaya [21] and Bearman [1].

Mitigating the occurrence of VIV by adjusting the natural frequency of the system to a domain away from likely vortex shedding frequency may seem simple, but this is not the case for a hydrodynamic system. This is because the behavior of the structure will affect its effective added mass which alters the natural frequency of the system. This mechanism has a tendency to bring the effective natural frequency closer to the forcing frequency, thus ensuring lock-in and large scale amplitude oscillations. This coupled relationship between fluid and structure can also affect the frequency of vortex shedding and bring about lock-in. Consequently, large-scale amplitude oscillations can be seen over a wider range of conditions than one would initially expect. It is this aspect of VIV in hydrodynamic systems that brings about difficulty in minimizing its consequences.

1.3 VIV Suppression Methods

In addition to the research conducted into understanding the phenomenon of VIV, much has been done to determine ways of suppressing it. A detailed overview of a wide range of suppression technologies can be found from the work of Zdravkovich

[29]. A number of methods have been developed that successfully reduce VIV. However, factors such as cost and difficulty of implementation have often restricted the application of these approaches with the exception of strakes. This is despite their high cost and the need to strengthen the structure in order to resist larger bending moments from increased drag [18]. One benefit of strakes is their omnidirectionality which means that they perform regardless of the direction of incoming flow.

Suppression methodology can be broken into two broad categories, passive and active. An active method is characterized as an approach that requires power input to perform its function. A passive method, on the other hand, is mostly attempted through structural modification without the need for power. Overall, three identified mechanisms exist for mitigating vortex induced vibrations. These are:

- Alteration of separation lines and/or separated shear layers through surface modification such as helical strakes, wires, studs, etc.
- Alteration of the entrainment layers through the use of a shroud or axial rods.
- Enhancements that prevent interaction of the entrainment layers. This includes splitter plates, guiding vanes, slits in the bluff body, etc.

Of the methodologies mentioned, omnidirectionality is only found in the first two groups and unidirectional approaches can be found in the first and third groups. A couple of straight forward approaches to inhibiting vortex induced vibrations are to modify the structure in order to change its natural frequency or to provide a means of energy absorption. Alteration of the natural frequency to a value at which vortex shedding will not occur is effective and can be accomplished through increased stiffness or a redistribution of mass. However, this is not always a possible solution, especially for many common offshore applications. Energy absorption can be accomplished though the addition of structural dampers, but this leads to issues of added forces on the structure that must be contended with.

Two particular flow elements are important to keep in mind and have spawned a multitude of approaches at suppressing VIV. These components are the "entrainment

layer", one on each side of the cylinder, and the "confluence point". The rotational fluid within the shear layers is what supports the growth of vortices. However, the entrainment layers provide an additional source of irrotational fluid for vortex development. Cutting off this source would lead to a substantial reduction in the strength of vortices. The confluence point marks the location where the entrainment layers come together. The period of the vortex shedding is determined by the time it takes for the confluence point to switch from one side of the wake's axis to the other. Modifying the unsteady behavior of the confluence point would affect the vortex shedding behavior. If properly undertaken, this process could result in weaker VIV behavior.

Another consideration in designing VIV suppression techniques is the correlation of vortex shedding along the length of the bluff body. A significant amount of evidence exists to suggest that the correlation length of vortex shedding plays an important role in determining the resultant oscillating lift force [12]. Vortices are shed in cells along a cylinder in lengths that can be related to the Reynolds number of the flow. The correlation length refers to the length of these cells. The intensity of in phase lift forces produced by vortex shedding is less significant if the cylinder is long compared to the correlation length [12]. Thus, breaking up vortex shedding into shorter length cells using vortex generators or other mechanisms is an approach that has been investigated and further explored in this thesis.

A multitude of various methods of suppressing VIV can be found in literature. A sampling of these approaches will be described to provide concrete means of implementing the approaches outlined in this section. Figure 1-2 provides graphical representation of numerous attempts at influencing VIV. A number of the depicted concepts have been shown to provide positive results in reducing vibrations and even concurrently reducing drag somewhat in many cases.

Surface protrusions play a prominent role in VIV suppression methods due to the inclusion of the common helical strake in this category. Research has found that a three-start helical strake with a pitch of $5D$ and strake height of $0.12D$ provides optimum performance [29]. However, even in this preferred configuration for VIV reduction, drag on the body remains high at a fairly consistent drag coefficient value

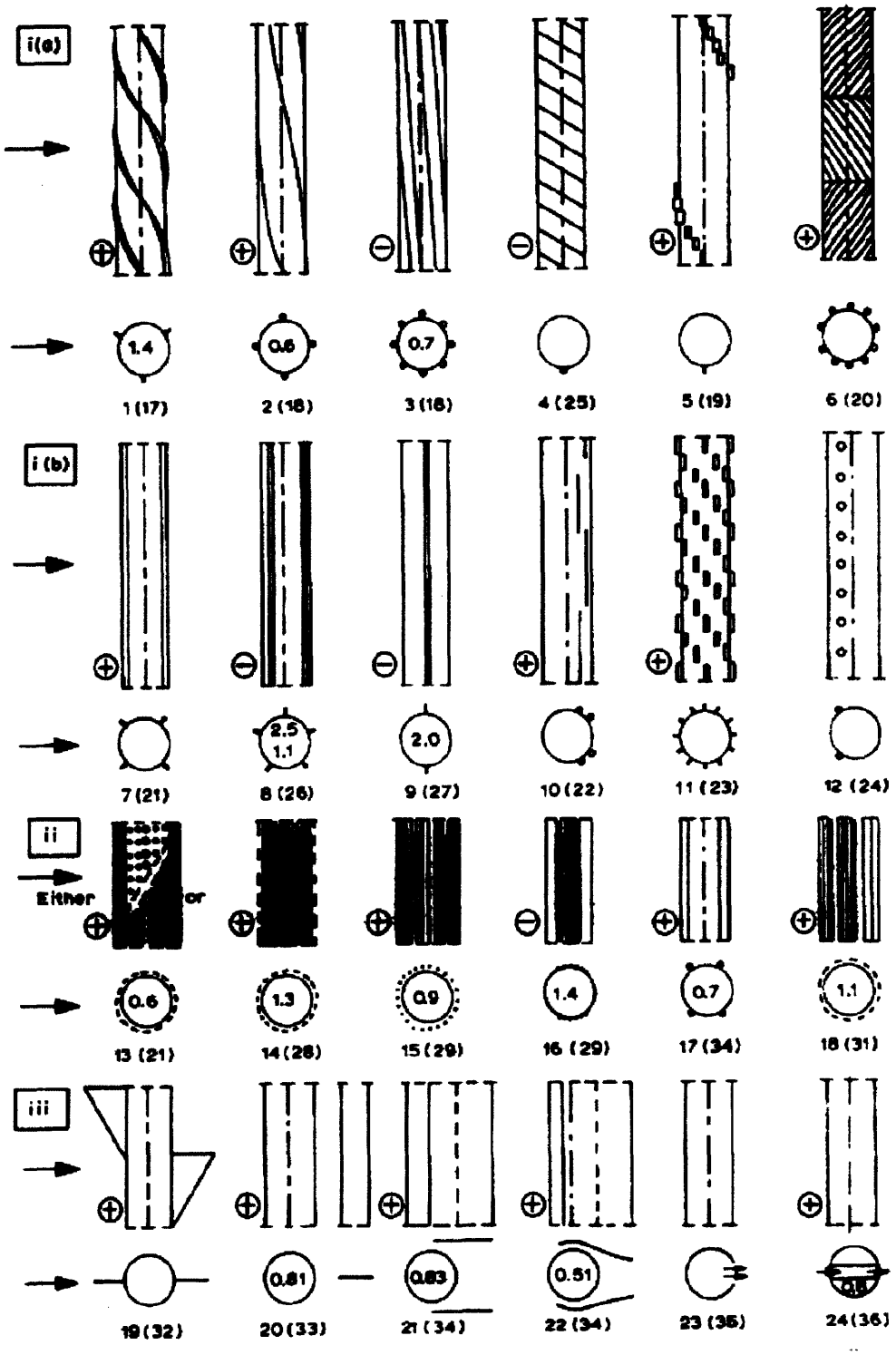

Figure 1-2: Aerodynamic and hydrodynamic means for interfering with vortex shedding: (i) surface protrusions ((a) omnidirectional and (b) unidirectional), (ii) shrouds, (iii) nearwake stabilisers (+ effective, - ineffective) [29]

of 1.45 across most Reynolds number flows. This is a substantial increase in drag for some cases such as in the critical regime where the coefficient of drag approaches a value of 0.5 for a bare cylinder [29].

An extension of the strake method is the helical wire. In this approach, thin wires are wrapped around the cylinder in a helical configuration. With this method, the pitch and number of wires is critical since tests have shown a marked increase in the amplitude of oscillations with some configurations. The optimum configuration for helical wires has been shown to consist of four wires with a helix pitch of $8 - 16D$, a clear deviation from the parameters for rectangular strakes.

The approach referred to as a shroud comprises many different designs. The use of a perforated shroud with circular holes has been explored by multiple researchers such as Price and Walsh. Investigations of the flow behavior revealed that vortices peel off the modified structure in rows. They were also noticeably smaller and formed several diameters further downstream. A reduction of the drag coefficient to 0.6 was seen over an extended range of Reynlods numbers [29]. Other approaches using a shroud were investigated by others in which square holes or a fine-mesh gauze were used. Extensions of the full shroud include axial-rod and axial-slat shrouds. In these approaches, thin rods or slats are arranged around the cylinder through which the flow has to travel. The thought is that individual vortex streets form and interact with one another in a destructive manner. It is also suggested that the axial-slat shroud acts to "impel" fluid between the slats and eject it into the downstream wake and "stabilize" it [29].

Another approach made toward achieving VIV suppression uses a nearwake stabilizer. The first use of this approach is credited to Hoerner where a triangular cylinder was attached to the test cylinder with its wedge pointing downstream. This resulted in a decrease of the drag coefficient to 0.89. Roshko [19] also explored nearwake stabilizers by testing long and short splitter plates attached to the downstream side of the cylinder. It was concluded that this approach delayed the formation of voritces by "extending the separated shear layers downstream of its trailing edge" [29]. This work was continued by many other researchers including Grimminger [7] who used

guiding vanes along the cylinder's boundaries. Plates were aligned parallel to one another on either side of the cylinder and inline with the flow. This resulted in a reduction in the drag coefficient to 0.83. This was further improved by using curved guiding vanes and extending them forward to introduce the vanes upstream of the cylinder. One further nearwake stabilizer approach was explored by Igarashi [10] in which a centerline slit was cut along the length of the cylinder to allow for a "self-injection of fluid into the nearwake" [29]. This served to extend the separated shear layers similar to the introduction of a physical barrier.

Many more methods have been attempted in an effort to reduce VIV, both passive and active. Active methods include using a rotationally oscillating circular cylinder by Lee [13] and internal acoustic excitation by Huang[8]. The work of the research described within this thesis sought to add to the list of successful candidates of VIV suppressors and perhaps provide a means that is more cost-effective and practical for widespread dispersion. The work of many researchers was considered in designing passive methods for investigation. In particular, the methods decided upon sought to make use of nearwake, entrainment layer modification and correlation length techniques. The approaches take into account the realization that vortex shedding is a phenomenon that cannot be completely eliminated, but its characteristics that cause VIV to arise can be targeted and altered.

Chapter 2

Experimental Setup

Two sets of experiments were conducted in this investigation of a passive method for the suppression of vortex-induced vibrations. All experiments were performed at the MIT Towing Tank Facility. Small-scale tests were conducted in a small glass-enclosed tank while large-scale tests took pace in the MIT Towing Tank. The equipment and test procedure are described in the proceeding sections of this chapter.

2.1 Small-Scale Towing Tank

2.1.1 Tank and Carriage

Some of the tests described in this thesis were performed in a 2.4 m x 0.75 m x 0.75 m glass-walled tank equipped with a towing carriage. The main structural component of the carriage system, shown in Figure 2-1, was a rolling platform mounted on the upper lip of the tank. This platform was attached to a motor driven chain that provided for its controlled motion along the length of the tank. A force sensor was attached to a cantilevered arm that extended out over an opening in the center of the platform. The mounting piece for the test object was attached to the load side of this 6-axis force sensor. The amplified force sensor output was differentially captured at 1 kHz with a National Instruments USB-6211 DAQ card.

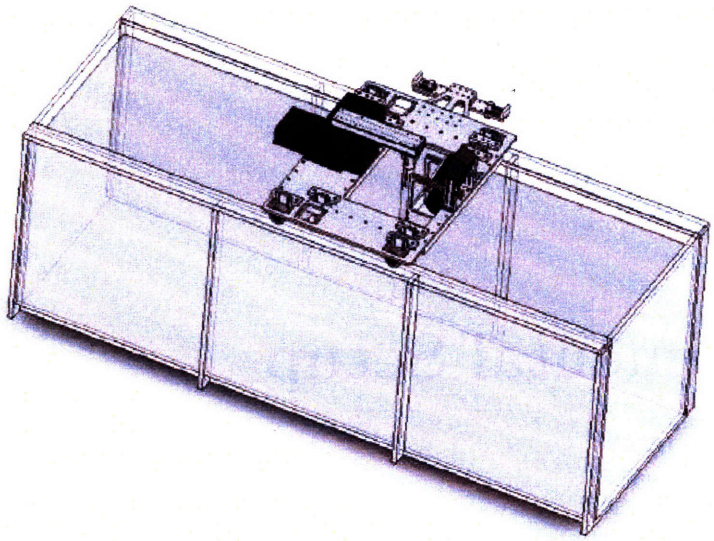

Figure 2-1: Computer generated model of the small tank setup.

2.1.2 Particle Image Velocimetry (PIV) System

Particle Image Velocimetry is a common technique used for visualizing flow behavior. The technique incorporates the use of a laser, high-speed camera, seeding particles and PIV processing software. Optics are utilized to create a thin sheet of laser light from a standard laser beam. This sheet of light is used to illuminate a plane within the flow of interest. This flow is seeded with small and reflective particles that will reflect the laser light. A camera is positioned and focused to film the plane of illuminated particles. Sequential images are captured at a high framerate speed to capture the movement of particles over short periods of time. This displacement of particles from frame to frame is analyzed using a PIV software package. The observed path of the particles provides a means of determining the directionality and speed of the flow being studied. A complete picture of the flow can then be generated from these motion vectors.

A PIV system was integrated into the assembly by mounting a high-speed LaVision Imager Pro camera onto the platform directly behind the test object. The

camera lens was directed into a water tight box with an acrylic viewing glass as its bottom. The bottom portion of the box was slightly submerged to eliminate an air to water interface through which the camera would film. This eliminated distortion that would be problematic were such an interface to exist. The system utilized a Quantronix Nd:YLF Laser to produce a laser sheet that was projected in an orientation perpendicular to the long axis of the test structure. Silver-coated particles with a mean size of 43 were dispersed throughout the water within the tank. High-speed images of these illuminated particles were taken within the range of 450 - 480 frames per second. The commercially available DaVis La Vision PIV software package was used to process these images and determine the flow vector fields. A 32x32 window size with an average of eight particles within a processing window was used. Studies have shown that these parameters provide an estimated error in reported velocities of approximately 4% [22].

2.1.3 Force Sensor

The force sensor used in small tank tests was a 6-axis load cell from JR3, Inc., with a linear load capacity of 110 N and moment capacity of 5.65 N-m. The factory calibration of the sensor was not suitable for the tests performed due to the distance from the sensor at which forces were applied. The factory calibration was determined in tests where forces and moments were independently applied at the sensor attachment point. The resulting calibration matrix representing voltage change in each channel as a function of applied force and moment did not provide proper accuracy when forces were applied far from the sensor attachment point. Thus, an independent calibration was performed in order to accurately measure forces and moments under the required conditions. This was performed by attaching a cylinder to the force sensor. Calibration weights of various masses were hung from the cylinder at various distance and the voltage response of each sensor channel was recorded. Forces and moments were applied in all directions with the exception of the z-axis. Forces in this direction were deemed to be inconsequential for the purposes of this work and thus, the force channel was not calibrated.

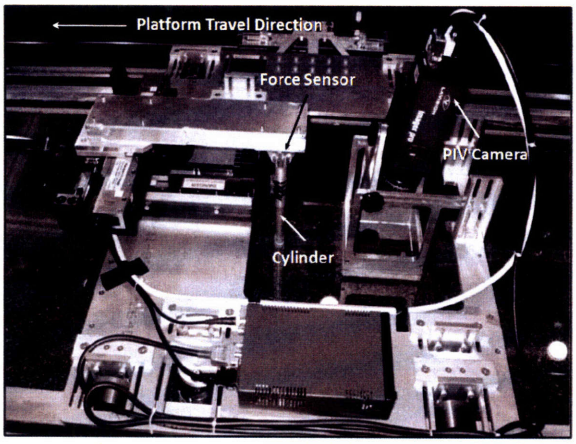

(a)

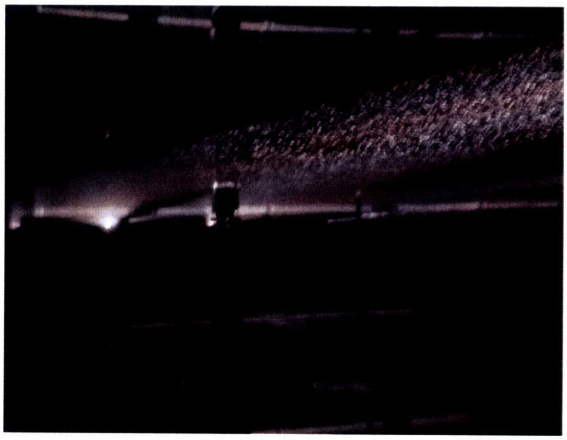

(b)

Figure 2-2: (a) The small tank carriage platform with major components labeled. (b) An example of the laser sheet entering the tank, providing a illuminated plane perpendicular to the cylinder along its length.

The calibration matrix for the JR3 force sensor was obtained from recorded voltages of the force/moment applications (Figure 2-4)using the equation

$$F = C * V \tag{2.1}$$

The calibration matrix, C, can be determined using the relation $C = F * V^{-1}$ since F is known and V is measured. The resulting C matrix from the calibration is provided in Table 2.1.3.

The linearity of the sensor response was verified to assess its behavior across a range of applied forces and moments. Figure 2-5 illustrates the relation between the

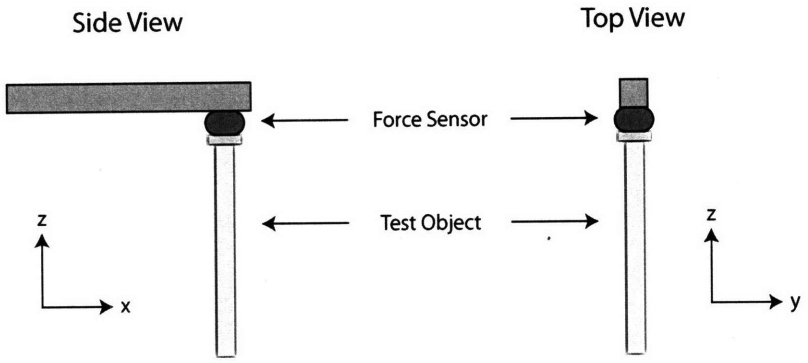

Figure 2-3: Orientation of axes for the JR3 load cell integrated into the small tank setup.

$$\begin{bmatrix} 12.971 & -0.233 & -1.608 & -1.007 & -0.264 & 0.985 \\ 0.030 & 13.104 & -4.779 & 0.208 & -1.467 & 1.067 \\ 0 & 0 & 0 & 0 & 0 & 0 \\ -0.112 & 0.012 & -4.664 & 0.486 & 0.112 & 0.195 \\ 0.050 & -0.005 & 2.139 & 0.073 & 0.627 & -0.104 \\ 0.036 & 0.027 & 1.776 & 0.060 & -0.055 & -0.701 \end{bmatrix}$$

Table 2.1: Calibration matrix for the JR3 load cell integrated into the small tank setup.

measured forces and moments from the calibration as determined using the resulting calibration matrix. A line with a slope of unity is shown for each channel to represent the ideal case where measured quantities would be equal to the applied forces and moments. The responses for F_x, F_y, M_x and M_y show linearity and agreement with expectations across the range of forces and moments of interest in this work. However, the response for readings of M_z shows increasing deviation as the moment about the z-axis is increased. Non-linearities in cross coupling with this channel seem to contribute to this growing error. The calibration was still deemed adequate since the measurement of this moment was not of significant importance. Further inquiry into the error in M_z measurements was not made.

2.1.4 Testing Procedure

A mount was designed to attach to the force sensor incorporated in the assembly while holding a cylinder with a diameter of 1.5 inches. Tests were performed of both

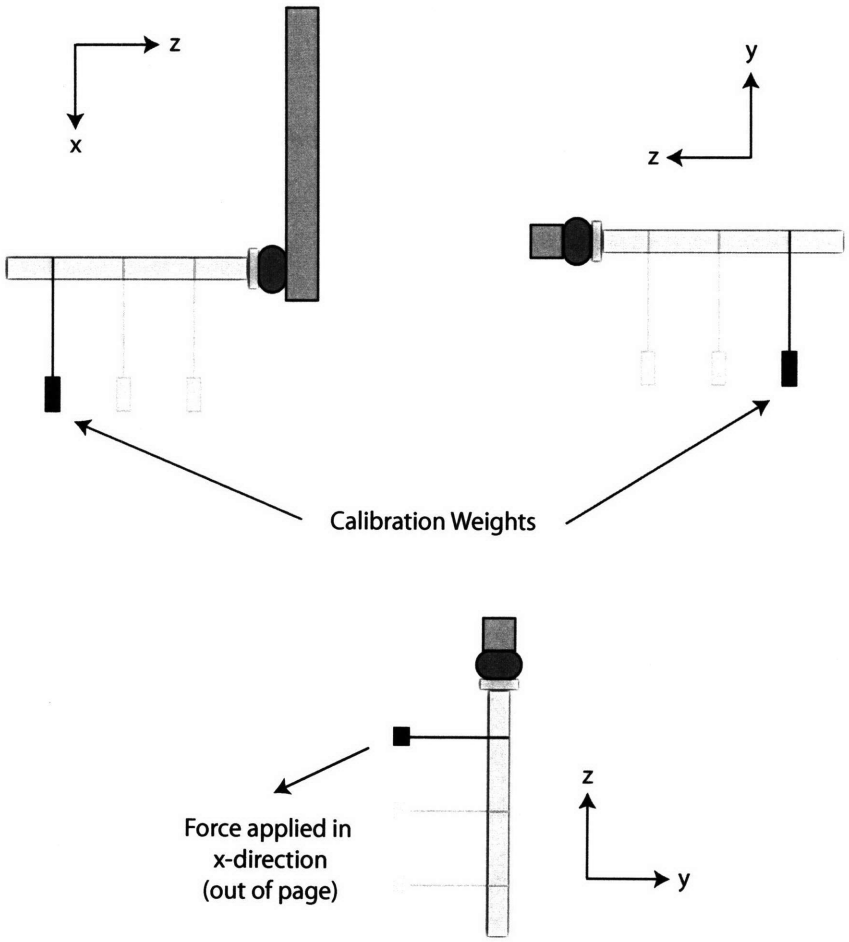

Figure 2-4: Depiction of the load cell calibration process. Weights were hung along the length of the attached cylinder producing a force in the x-direction and a moment about the y-axis. The orientation of the sensor/cylinder combination was changed so that forces were applied in the negative y-direction with a moment produced about the x-axis. Finally, a force was applied in the x-direction with a moment produced about the z-axis.

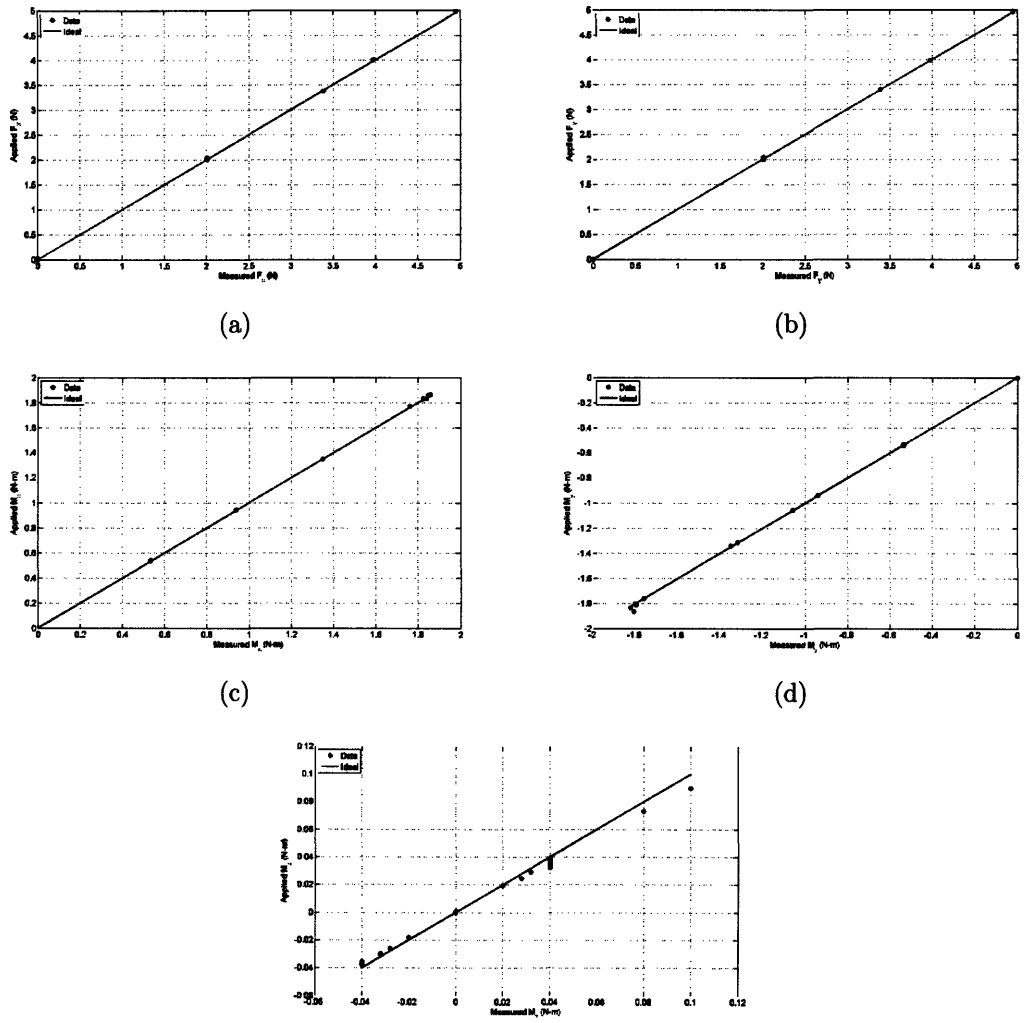

Figure 2-5: Assessment of the calibration for the force sensor channels (a) F_x, (b) F_y, (c) M_x, (d) M_y and (e) M_z.

a bare and modified cylinders in the same fashion. The test object was attached to the force sensor. The platform was engaged and propelled at a constant speed of 0.25 m/s. The laser was fired and images of the flow were captured following a delay of a few seconds after initial motion of the platform.

2.2 Towing Tank

The towing tank used in large-scale, free-vibration tests is the principle experimental apparatus in the MIT Towing Tank Facility. The tank has a total length of 22.5 m, a width of 2.4 m and a maximum depth of 1.2 m. A rail system incorporating a motor is mounted along the length of the tank. A carriage is connected to this rail system allowing for motion along the length of the tank at a prescribed speed. The carriage consists of two main components: a structural framework which is directly attached to the rail and a connected spring-mounted oscillating rig. The oscillating rig consists of its own framework incorporating two spars, one on either side of the tank, that extend downward into the water. The cylinder is mounted underwater between these two spars. The mount points for the cylinder incorporate Kistler piezo-electric force sensors that allow for the measurement of forces acting on the cylinder.

The oscillating rig structure is mounted on a roller bearing system (Figure 2-7). This allows for independent motion of the rig structure in the transverse direction. A linear motor assists the oscillation of the rig in order to counteract frictional forces introduced by the bearings. The motor is tuned to mimic a lightly damped "free-vibration" system. The structural damping of the overall system is measured and the oscillatory decay is recorded each time a cylinder is attached. This is done in order to ascertain the damping ratio of the system. This ratio varies across the amplitude of oscillations from about 1.5% to 11% with higher A/D amplitudes having lower damping ratios. A final component of the rig is a linear potentiometer that records the transverse motion of the oscillating rig. This provided a means of measuring the cylinder's oscillatory behavior.

2.2.1 Linear Motor Control

The linear motor integrated into the carriage system is meant to counteract frictional damping in the roller-bearing assembly. The goal is to mimic a mechanically un-damped system allowing the cylinder to behave under only hydrodynamically damped conditions. Hence, the linear motors work to force the cylinder assembly in the

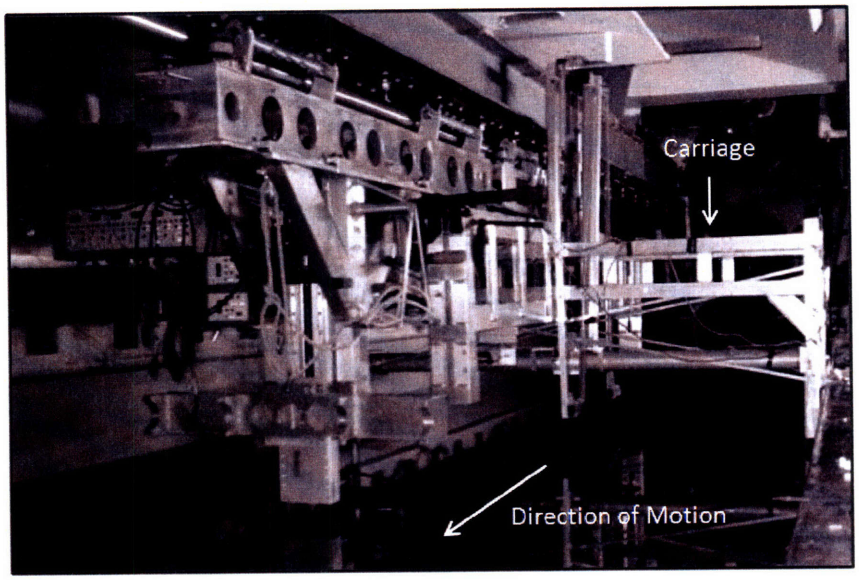

Figure 2-6: Image of the full carriage assembly in the MIT Towing Tank.

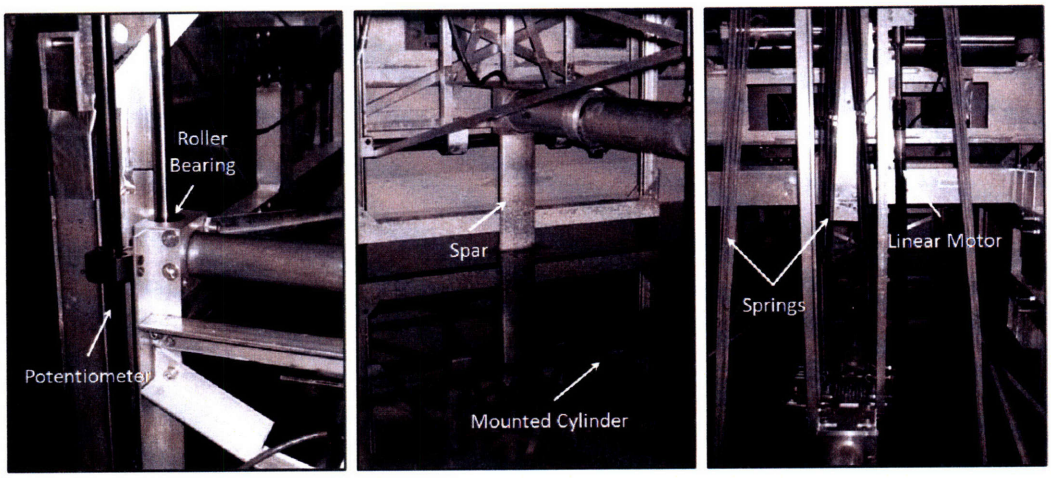

(a) (b) (c)

Figure 2-7: Components of the tow tank carriage structure. (a) The potentiometer is used to measure the vertical position of the test objec as the rig moves along the roller bearing track. (b) The spar (one on either side of the tank) dips down into the water with attachment points at their end to which the test objec is mounted. The mounting points incorporate piezo-electric force sensors. (c) The springs and linear motor are used to create a lightly damped spring system.

direction of motion, thus countering friction within the bearing assembly. The control algorithm for the motor is designed and tested to ensure that energy is not being pumped into the system to force the cylinder's motion, but instead only assisting its desired behavior resulting from hydrodynamic forces.

The control principle for the motor involves monitoring the velocity and position of the oscillating rig. The amount of force imparted on the system by the motor is,

$$F(t) = \left\{ \begin{array}{ll} k_1 V(t) + k_2 V(t)^p & if\ V > V_{min} \\ k_1 V(t) + k_2 V(t)^p & if\ V_{min} < V < V_t\ and\ -Pos_t < Pos < Pos_t \end{array} \right\} \tag{2.2}$$

The forcing value will be determined by one set of constants, k_1 and k_2 for the case where the velocity, V, is greater than a chosen minimum value, V_{min}. However, once the amplitude of the oscillation has decayed sufficiently, the forcing needs to be adjusted to counter increasing static friction. Thus, the constants are changed in the forcing equation when the velocity is less than a threshold velocity, V_t, and the amplitude is between a normalized negative/positive position threshold, Pos_t, about the cylinder's equilibrium position.

2.2.2 Kistler Sensor Calibration

The force data is measured by a pair of Kistler piezo-electric sensors embedded in the test object mounting locations. These sensors experience drift over time and are sensitive to the forcing involved in changing out the test object. As a result, the sensors must be calibrated before each set of tests to ensure accurate readings.

Calibration of the sensors is carried out by loading the mounted object in both the lift and drag directions while recording measured voltages. Force application in the lift direction was completed by hanging a weight from the mid-span point of the cylinder. The loading in the drag direction is accomplished through means of a pivoting moment-arm system shown in Figure 2-8. These measurements are then used in a matrix form to solve the system

$$\overline{\overline{V}} \times \overline{\overline{C}} = \overline{\overline{F}} \tag{2.3}$$

where $\overline{\overline{C}}$ is the calibration matrix, $\overline{\overline{V}}$ is the voltage matrix and $\overline{\overline{F}}$ is the force matrix.

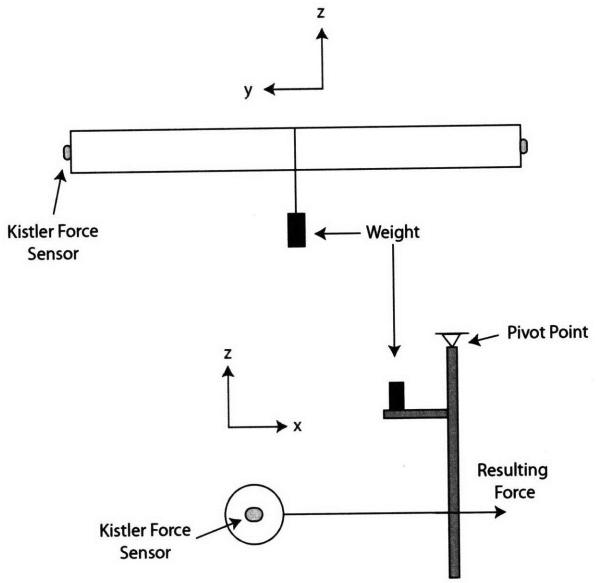

Figure 2-8: The calibration method used for the Kistler force sensors is depicted.

2.2.3 Testing Procedure

The steps followed in the tests conducted using the tow tank are as follows. A bare cylinder was attached to the rig and a pluck test was conducted. The term pluck test is used to describe the procedure used to determine the natural frequency and damping ratio of the system. The linear motors were engaged and the mounting rig was pulled up to its highest allowed position in the carriage assembly and allowed to oscillate back to a resting state. The time varying position of the cylinder was recorded during this period of oscillations. The data collected was analyzed to find the natural frequency and damping ratio of the system. The damping ratio was determined by analyzing the logarithmic decrement of the position sensor signal. Each pluck test was conducted with a bare cylinder to obtain this information for an unmodified system. Thus, any changes induced by the actual test structure were solely due to enhancements made to the control cylinder.

The test cylinder was run through a series of twenty reduced velocities ranging from 3.5 to 10.0 with the linear motors enabled during these tests. The speed was set for the given run and the carriage set in motion using a LabView control program for the system. Upon initial movement, the cylinder was given an initial perturbation to

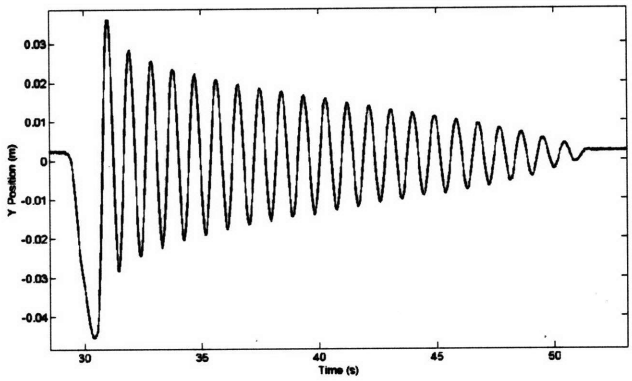

(a)

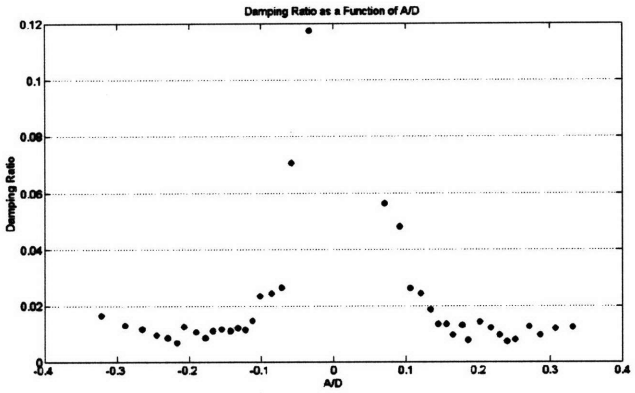

(b)

Figure 2-9: Sample of the position signal recording from a pluck test and the calculated damping ratio as a function of A/D.

begin an oscillatory motion. The vertical position of the cylinder and forces acting on it were recorded as it was towed the length of the tank. The carriage was then reset to the initial position and the procedure was repeated for each reduced velocity until the series had been completed for that configuration.

2.3 Modifications

The various modifications made to a bare cylinder in this investigation are defined and explained in their respective sections. The goal of these modifications was to modify the flow behavior so as to reduce vortex induced vibrations that are typically seen on bluff-bodies. The approaches used to accomplish this were to either guide the flow around the cylinder or produce competing fluid structures such as vortices to counteract the typical vortex shedding commonly observed for a bluff-body.

Chapter 3

Hydrofoil Vanes

3.1 Overview

One method of minimizing the effect of vortex shedding on the body is to delay the formation of vortices further downstream. This limits the interaction of these flow structures with the body. The approach considered to achieve this goal was to attach continuous hydrofoils along the length of the cylinder. In effect, these hydrofoils would function similar to the guiding vanes investigated by Grimminger [7]. The trailing edges of the foils would, in most cases, protrude slightly aft of the cylinder thus extending the shear layers somewhat. Also, the foils can serve to streamline the flow around the cylinder and reduce the momentum deficit in the wake and, in consequence, the drag force exerted on the body. The streamlined characteristics of the hydrofoil produce a different flow pattern than is typically observed for a bare cylinder. The resulting vorticity in the flow is not necessarily shed in an alternating pattern.

A further consideration of the hydrofoil design was that a gap exists between the cylinder surface and the hydrofoils. Fluid funneled into this region will be accelerated and injected into the wake. This could possibly serve to keep the shear layers separate from one another over a longer distance and minimize their interaction. It would also inject additional momentum into the wake, reducing the deficit responsible for drag on the body.

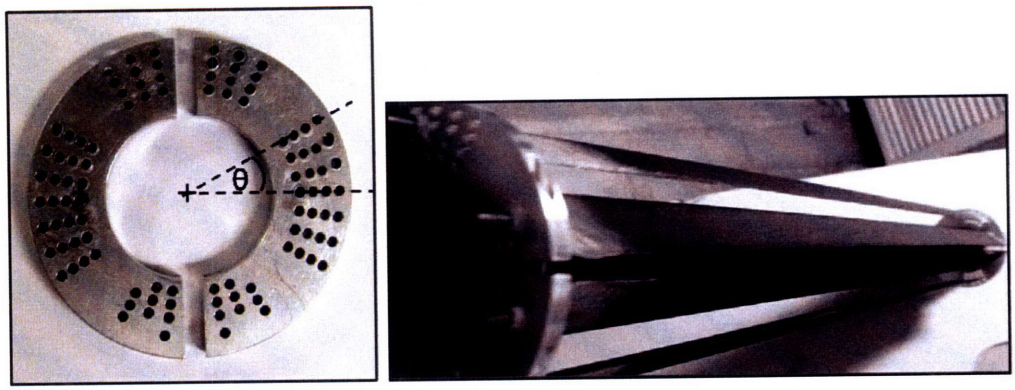

(a) (b)

Figure 3-1: (a) Clamps used to attach E423 hydrofoils to a bare cylinder and (b) a representative image of the quad foil configuration.

3.2 Hydrofoil Attachments

A bare aluminum cylinder with a 3.81 cm diameter and 20:1 length-diameter ratio was used as a starting structure and control case for this round of tests. Various modifications were made to the cylinder which included the addition of a downstream triangular fairing and parallel mounted hydrofoils. The triangular fairing was attached directly onto the downstream side of the cylinder and the hydrofoils were attached to the cylinder by means of specially made C-clamps depicted in Figure 3-1. These clamps had insert holes drilled through them in a circumferential pattern at various radial distances from the center of the cylinder. Hydrofoils with a E423 profile with chord lengths of 3.18cm and 2.41cm were made from epoxy hardened foam. A threaded post was imbedded in both ends of each foil and served as a means of attaching the foils between the two C-clamps situated and secured at opposing ends of the cylinder.

A number of different foil configurations were tested and are depicted in Figure 3-2. The cylinder, with and without the triangular fairing, was further modified by attaching a pair of hydrofoils. Each foil was attached in a manner to have it situated over the poles of the cylinder (the locations at which highest flow speed is attained). Furthermore, one configuration tested had two pairs of hydrofoils with different chord lengths simultaneously attached without the fairing. The pair of

smaller chord length foils was attached directly downstream of the cylinder while the larger pair was attached as previously mentioned.

Three major configuration parameters were defined for the cylinder and hydrofoil system. First, the attachment location of the hydrofoil can be located anywhere along the circumference of the cylinder. This parameter was defined as the swivel angle where a value of zero degrees places the attachment points directly above the poles of the cylinder. Positive swivel angle denotes that the attachment point was rotated closer to the downstream stagnation point. Second, the height of the hydrofoils was defined as the distance of the hydrofoil attachment point from the cylinder surface. Finally, the third parameter was the angle of attack of the hydrofoils relative to the free stream flow.

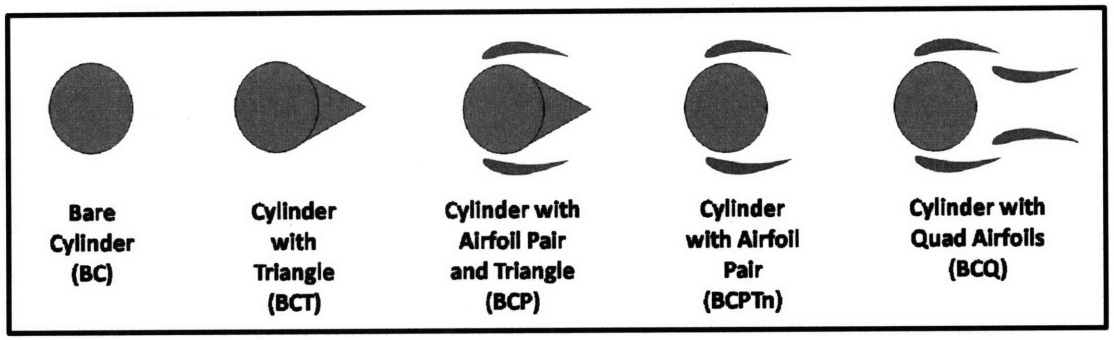

(a)

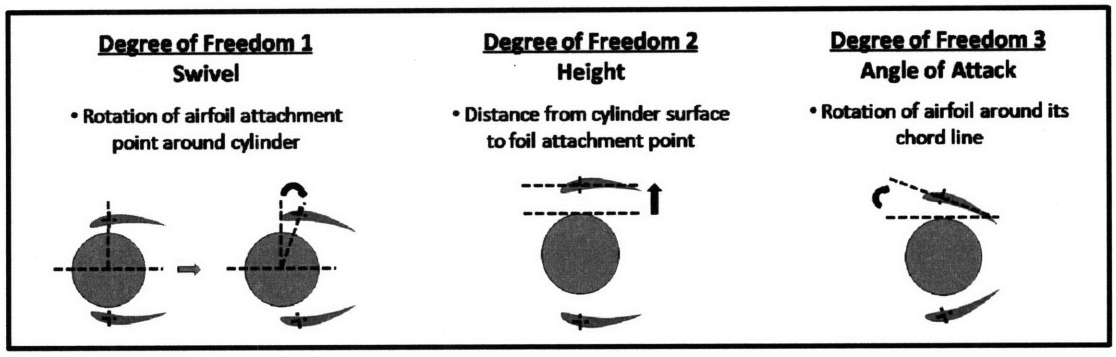

(b)

Figure 3-2: (a) Hydrofoil modifications made to a bare cylinder and (b) the controllable parameters of these configurations.

3.3 Configurations Tested

A total of fifty-six different configurations of the outlined parameters were investigated using a triangular fairing, single and dual hydrofoil pairs. Alterations in all possible parameters were made. The naming protocol for these configurations was chosen with the following prefixes

- *BC* : Bare cylinder with a diameter (D) of 3.81cm.
- *BCT* : *BC* modified with a triangular fairing of extension length D.
- *BCP* : *BCT* with a pair of hydrofoils (chord of 3.18cm).
- *BCPTn*: *BC* with a pair of hydrofoils (chord of 3.18cm).
- *BCQ* : *BC* with two pairs of hydrofoils - larger pair (chord of 3.18cm) and smaller pair (chord of 2.41cm) of hydrofoils.

A complete listing of tested configuration is provided in Figure 3-3. The effectiveness of the modifications described in this chapter were verified from tests conducted in the small tank. The test object was towed along the length of the small tank while measurements of forces acting in the inline and transverse directions were recorded. In addition, flow visualization of the wake directly behind the object was performed using the integrated PIV system. All tests were conducted at a Reynolds number of 8.5×10^3 based on the cylinder diameter.

A few configurations were selected for discussion in this chapter. These configurations are

- *BCP* : *BCT* with pair of hydrofoils (chord of 3.18cm) positioned at a height of 1/3×D, swivel angle of 10° and angle of attack of 0°.
- $BCPTn_1$: *BC* with a pair of hydrofoils (chord of 3.18cm) positioned at height of 1/3×D, swivel angle of 0° and angle of attack of 10°.
- $BCPTn_2$: *BC* with a pair of hydrofoils (chord of 3.18cm) positioned at height of 1/3×D, swivel angle of -20° and angle of attack of -10°.

- BCQ_1 : BC with two pairs of hydrofoils - larger pair (chord of 3.18cm) positioned at height of 1/6×D, swivel angle of 0° and angle of attack of -10° with a smaller pair (chord of 2.41cm) at height of 1/3×D, swivel angle of 60° and angle of attack of 0°.

- BCQ_2 : BC with two pairs of hydrofoils - larger pair (chord of 3.18cm) positioned at height of 1/6×D, swivel angle of -20° and angle of attack of -10° with a smaller pair (chord of 2.41cm) at height of 5/12×D, swivel angle of 70° and angle of attack of 0°.

3.4 Analysis of Streamlines

The flow visualization that was performed provides a means of assessing the flow behavior for tested configurations. Samples of time-spaced streamline patterns are shown in Figure 3-4. The results for the bare cylinder, BC, show the expected shedding pattern where vortices are shed off the cylinder and move downstream in a periodic pattern with alternating rotation. These vortices generate an assymetry in the wake and cause streamlines to bend and curve. This effectively results in a widening of the wake behind the cylinder which correlates to higher drag. Reducing this behavior would be a key step in approaching potential flow behavior.

The addition of the triangular fairing to the back of the cylinder resulted in a slightly more time constant and symmetric flow. The fairing does not seem to have provided a complete mechanism for eliminating an adverse pressure gradient for the flow as it moves past the cylinder poles. The streamlines do not appear to follow the contour of the body and separation seems to occur at approximately the same location as that seen for the bare cylinder. Some regions of defined rotation are still noted and have an effect on the flow behavior. However, flexing behavior of the wake is less pronounced than that seen for the unmodified cylinder. It may be that the separation of shear layers over a longer distance is causing defined vortex formation outside the view of the camera. The flexing of the wake that is observed occurs near

the perimeter of the available view. The flow maintains an undisturbed freestream pattern over a larger region of the view with the effects of the body confined to a more narrow band directly downstream. Delaying vortex formation is attributed to splitter plates and suggested to reduce VIV impact on a body. This flow modification by the triangular fairing is supported by this analysis and effects on forces will be mentioned in Section 3.5.

The addition of foils to the *BCT* configuration serve to further modify the flow toward a more potential-like behavior. The regions of circulation are predominantly confined to very small regions in comparison to the *BC* flow pattern. These regions occur near the trailing edges of the foils and do not seem to significantly spread outward into the wake over time. Furthermore, the foils act to direct flow around the cylinder body with the fairing acting to return the flow more gradually to free stream conditions. This combination allows for the flow to converge behind the cylinder and act to keep the two regions of circulation at the foil tips separate from one another. This pattern remains fairly consistent over time with a relatively symmetric behavior around the body. The injection of free stream fluid into the wake serves to reduce the momentum deficit that occurred with the bare cylinder. This particular case demonstrates well the potential of reducing instabilities in the velocity profile by modifying the flow with hydrofoils.

3.5 Vorticity and Force Analysis

A power spectral analysis was conducted on the lift data collected to assess the intensity of the unsteady lift force acting on the body. Reducing the intensity of these periodic fluctuations should serve to reduce forcing and thus, vibrations of the body. Therefore, minimization of the lift force fluctuations often guided the selection of hydrofoil height, swivel angle, and angle of attack. During the variation of these three parameters, cases where the unsteady lift force was amplified or reduced relative to the bare cylinder case were noted. Results for a few sample configurations are presented in Fig. 3-5. A predominant peak in the power spectral density results is

often noted near the natural frequency of the unmodified system as determined from the BC result. In some cases, such as BCQ_1, this peak at the fundamental frequency is dramatically reduced. However, it is noted that a higher harmonic peak was often seen with the foil configurations.

For the bare cylinder control case, typical alternating vortex shedding was seen with a corresponding peak in the PSD analysis at a Strouhal number of approximately 0.2. The vorticity field from the BCT configuration as depicted in Figure A-1 depicts that constant streams of vorticity shed off of the structure without clear alternate shedding of defined vortices. However, the triangular fairing does not completely eliminate the unsteady lift force, as seen in Figure 3-5. Nevertheless, the power content of the frequency observed in the PSD from the bare cylinder has about half the magnitude. This can be explained by considering the mean behavior of the wake. The "flexing" of the wake as seen for the bare cylinder is still noted for the BCT case. However, the point at which the wake begins to exhibit this behavior is further downstream. This may be the result for the reduced impact on the lift force intensity. Such an explanation confirms that moving vortex shedding, or in this case, cyclical shedding of the wake further downstream, can reduce the forcing that is responsible for VIV on the body.

The PSD analysis of the lift signal for the $BCPTn_1$ configuration (Figure 3-7) indicates minimal power content for all frequencies. As with BCT, fairly consistent streams of vorticity of both rotational directions are seen to leave the structure. One apparent influence of the hydrofoils in this configuration is the addition of leading-edge and trailing-edge vorticity from the hydrofoils into the wake that combines with the vortices shed from the cylinder. This mingling of flow structures seems to cancel out a distinct pattern of shedding and leads to a less coherent wake. Two factors appear to contribute to the interaction for this particular configuration. First, the positive angle of attack acts to direct shedding from the hydrofoils into the immediate vicinity directly behind the cylinder. Secondly, the directing of vortices into this area is affected by the swivel angle of the foils. The trailing edges of the foils protrude just beyond the curvature of the cylinder, thus allowing for more direct influence in the

near-surface wake region. The overall behavior of the wake remains fairly constricted and does not exhibit the flexing behavior as mentioned for the triangular fairing case.

In contrast, the $BCPTn_2$ case displayed well-defined alternating vortex shedding. This behavior is reminiscent of that observed for the bare cylinder but lacks the same pronounced consistency. A notable difference is that the vortices tend to wrap around the back-end of the cylinder and remain closer to its surface. This is coupled with a higher power spike in the PSD results. It seems that pushing the hydrofoils forward and orienting them with a negative angle of attack reduces their influence on the wake that was seen for $BCPTn_1$. Furthermore, a negative angle of attack has two results; the vorticity being shed off of the foils is weaker and not directed into the wake region directly behind the cylinder. This configuration does not considerably interfere with vortex shedding from the cylinder, but instead seems to amplify its effects on the lift force felt by the structure.

A change in flow behavior was found when the triangular fairing was combined with the hydrofoils (BCP). The case shown in Figure 3-8 is typical of this configuration. Generally, vorticity was seen to shed in streaks. Analysis of the PSD does not show a strong fundamental frequency of oscillation in the force signal, although a peak at a higher frequency is noted.

Two sets of PIV images from quad-foil configurations are provided in Figure 3-9 to demonstrate the effect of parameter adjustment on this configuration. The BCQ_1 configuration, in which the larger foils are located further downstream, shows a reduction in the intensity of lift signal fluctuations. Again, as with $BCPTn_1$, having the foils positioned further back allows for the flow structures from the foil tips to best interact with the cylinder wake. Furthermore, with the additional foils of smaller chord length now present, vorticity is shed from the set of larger foils and remains separated from the region located directly behind the cylinder. This leads to less significant influencing of the cylinder itself from these flow structures. It is noted that the wake pattern fluctuates upwards and downwards as described for the BCT configuration. Nevertheless, this occurs to a fairly minimal degree and leads to little power content in the PSD of the lift signal.

The BCQ_2 foil configuration for which the large foils have been moved forward to a swivel angle of negative twenty degrees exhibits different results. The smaller chord hydrofoils have also been moved slightly closer to one another with the adjustment of the swivel angle to seventy degrees. For this case, the vortices that shed off the larger foils exhibited a tendency wrap around and enter the relatively stagnant region between the two smaller hydrofoils aft of the cylinder. This wrap around occurred in a periodic fashion which may be the cause of the peak in the PSD analysis indicating a fluctuating lift signal. Even with this BCQ modification, the force analysis suggests forcing of the cylinder that could lead to VIV behavior. The BCQ approach provides different results driven by the chosen parameters of foil positioning.

Drag reduction was also investigated for the hydrofoil modified cylinders. The mean drag coefficient ratios between the modified configurations and the bare cylinder are shown in Figure 3-10. The drag coefficient for the control case, BC, is labeled as C_{Do} and has a value of 1.33. A respectable reduction of approximately 15% was seen for the BCT modification. Further reductions in drag differed depending on the cylinder modification with variations depending on the chosen parameters of foil height, swivel and angle of attack. Overall, most cases led to a reduction in drag with the exception of some cases. The greatest benefits were seen for the BCP configurations with a maximum reduction of 48%. This is coupled with the previous observation regarding the flow behavior and transverse forcing of this configuration. The flow exhibited less unsteadiness as seen in flow visualiztion and is supported by a power spectral analysis on the recorded lift force. This is noteworthy since it suggests that the structure will not tend to vibrate from unsteady lift forces. This makes the reduction in drag even more significant when factoring in that the drag coefficient for a bare cylinder undergoing transverse oscillations can exceed a vlue of three.

BC	BCT

BCP	H1							
	S-20		S0				S20	
	A-10	A0	A-10	A0	A10	A20	A10	A20

BCP	H3			
	S0		S20	
	A10	A20	A10	A20

BCPTn	H1				
	S-20		S0		
	A-10	A0	A-10	A0	A10

BCPTn	H3				
	S-20		S0		
	A-10	A0	A-10	A0	A10

BCQ	LH1							
	LS0, LS20							
	LA0, LA-10							
	SH3				SH4			
	SS60		SS70		SS60		SS70	
	SA0	SA-20	SA0	SA-20	SA0	SA-20	SA0	SA-20

Figure 3-3: The adjustable parameters are height (H), swivel angle (S) and angle of attack (A). The parameters for the *BCQ* configuration are similarly denoted with the addition of a preceeding S or L indicating whether the parameter value refers to the small or large hydrofoil pair, respectively.

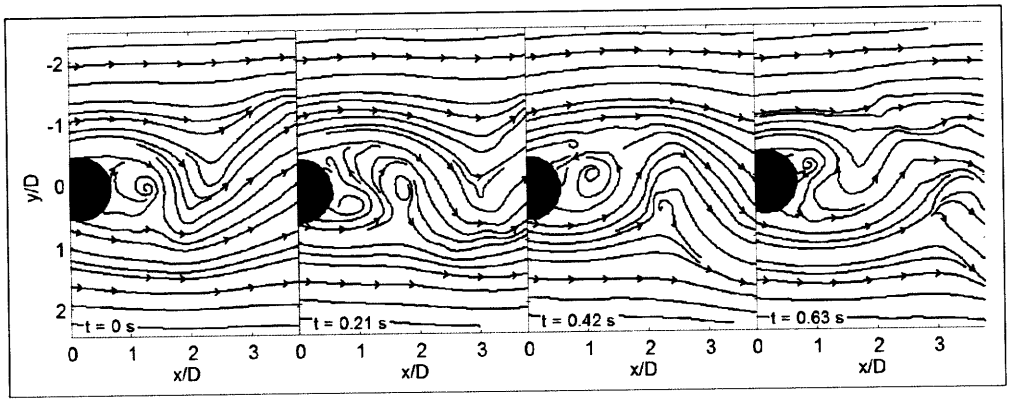

(a)

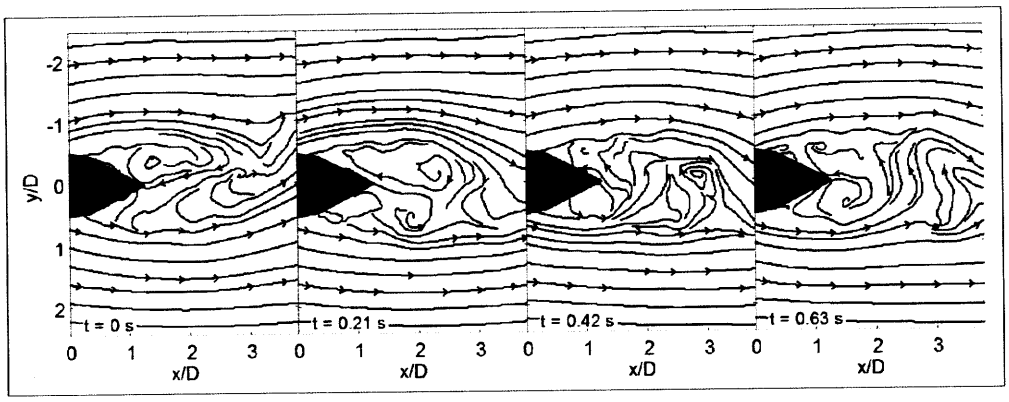

(b)

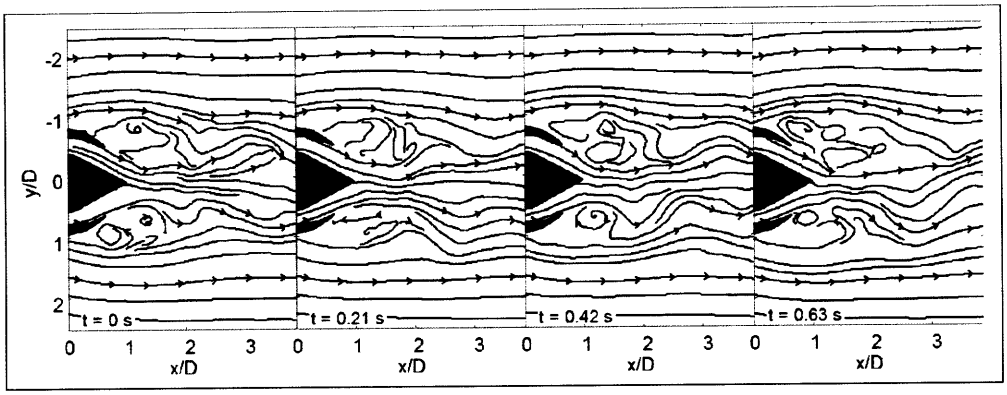

(c)

Figure 3-4: Time spaced captures of the streamlines for (a) BC, (b) BCT and (c) BCP configuration as constructed from flow visualization analysis.

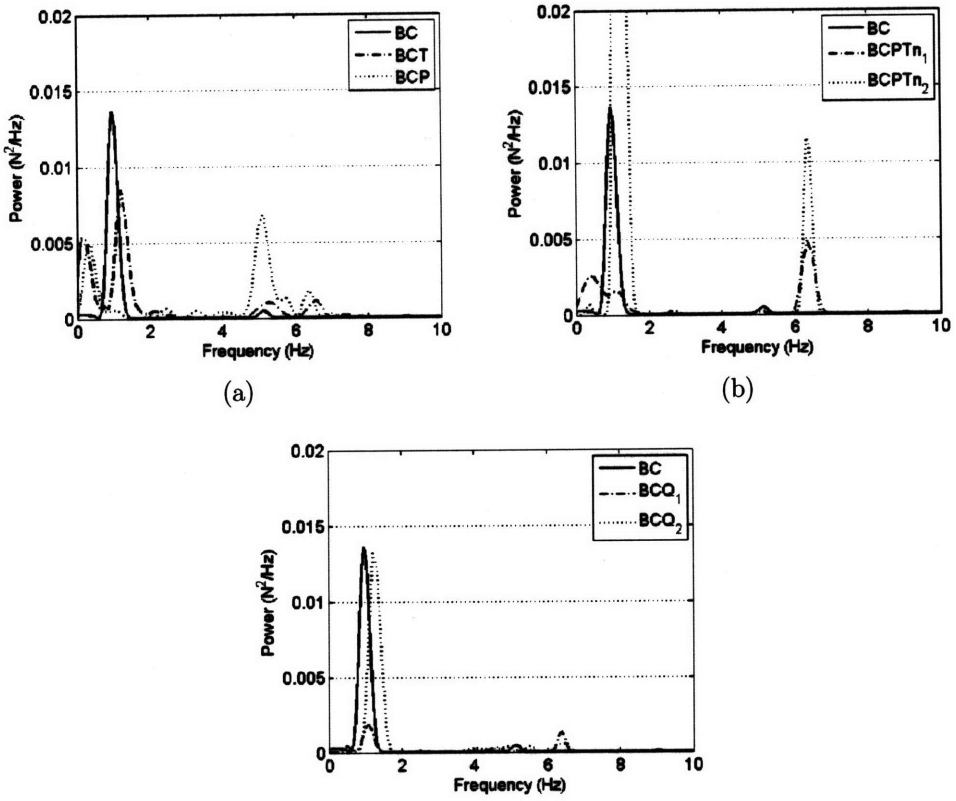

Figure 3-5: Power spectra for various hydrofoil configurations showing both positive and negative changes in behavior.

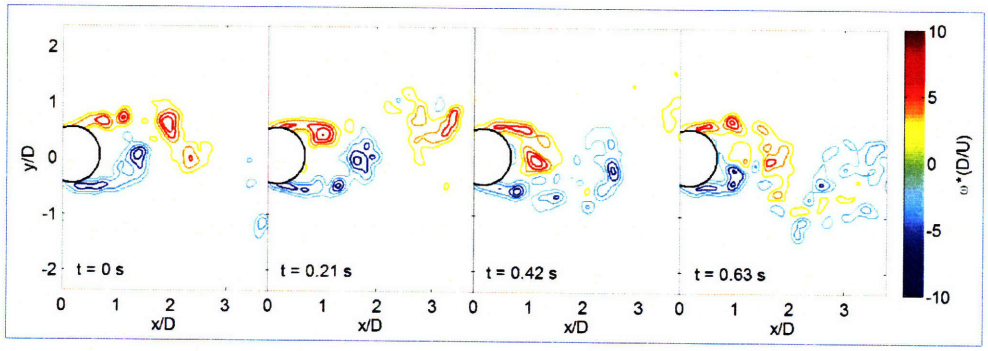

(a)

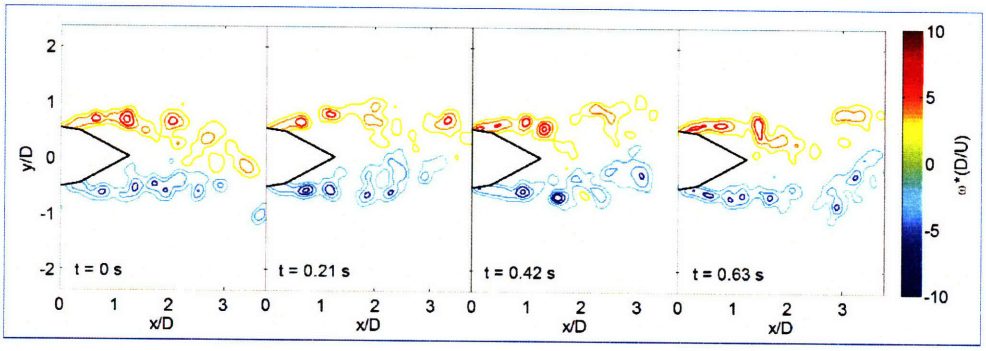

(b)

Figure 3-6: Time spaced vorticity fields for the (a) BC and (b) BCT configurations.

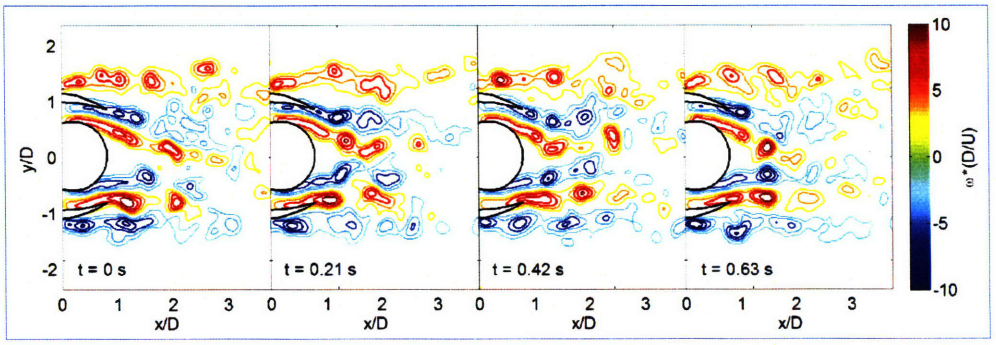

(a)

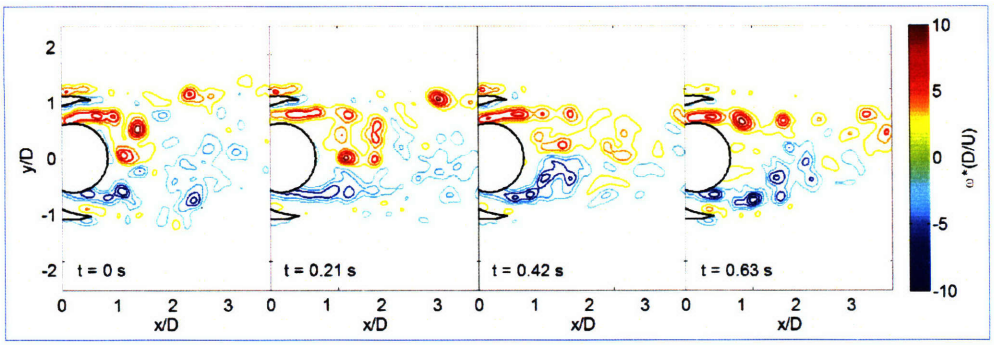

(b)

Figure 3-7: Time spaced vorticity fields for the (a) $BCPTn_1$ and (b) $BCPTn_2$ configurations.

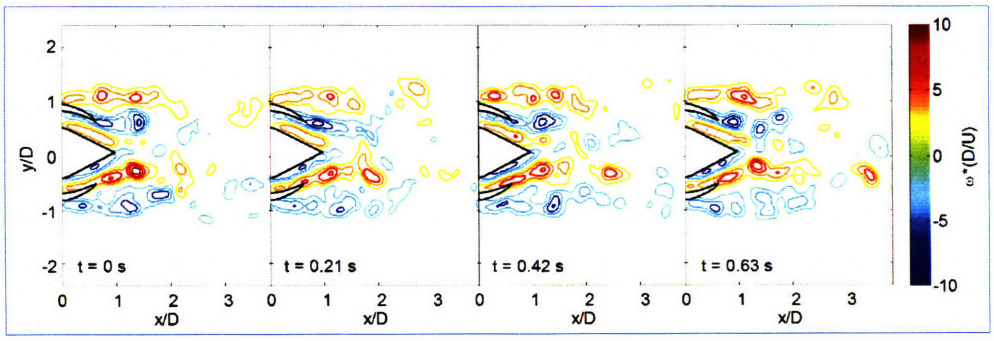

Figure 3-8: Time spaced vorticity fields for the BCP configuration.

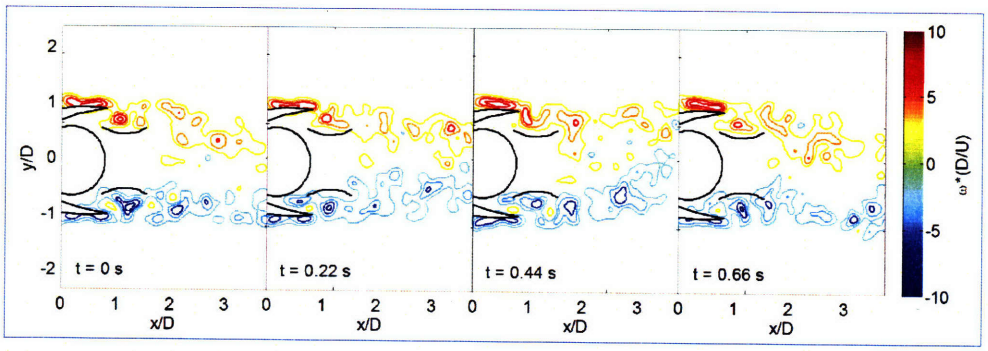

(a)

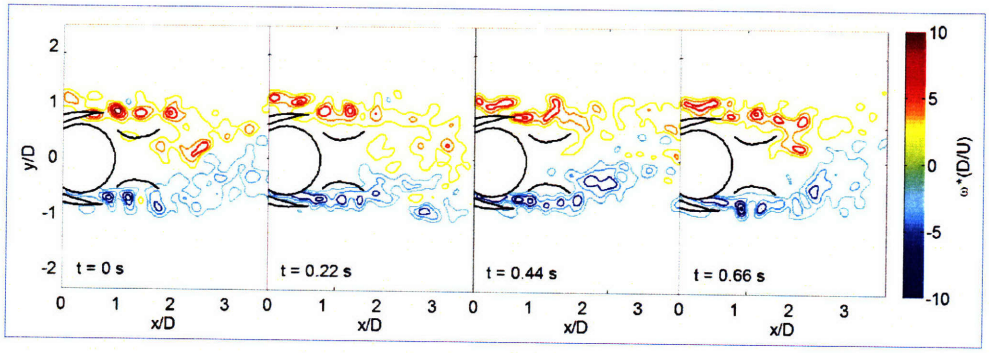

(b)

Figure 3-9: Time spaced vorticity fields for the (a) BCQ_1 and (b) BCQ_2 configurations.

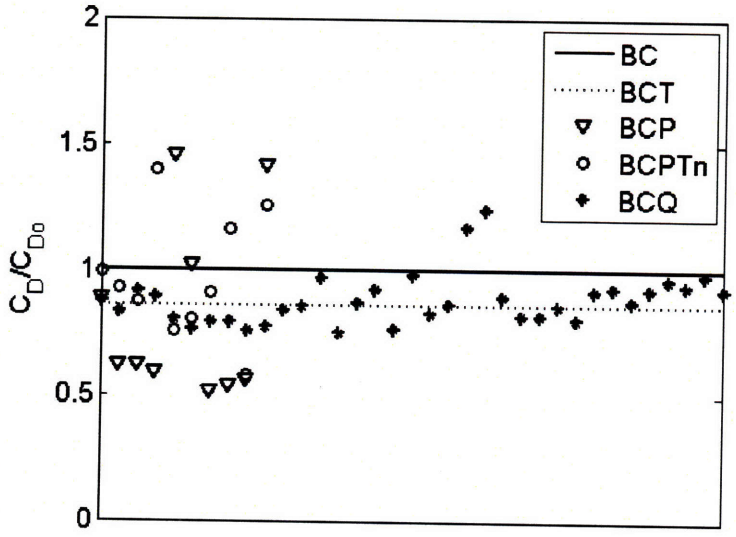

Figure 3-10: Drag ratios relative to BC results for tested hydrofoil configurations.

Chapter 4

Delta Wings

4.1 Overview

The method presented in this chapter is intended to break-up the spanwise vortex structure by introducing vortex generating delta wings along the length of a cylinder. This disturbance of the correlation length is believed to reduce the influence of vortex shedding on the structure. Flow over a delta wing results in the generation of a "vortex tube" with an axis in the direction of the free stream. Such a flow structure could possibly "cut" through the vortex structure shed along the length of the cylinder. Such a result would serve to mitigate some of the fluid induced forces acting on the cylinder.

Mounting delta wings horizontally above the cylinder surface also introduces greater damping into the system. These flat surfaces will resist transverse motion that forces fluid against the wing's surface. Furthermore, the added mass of the structure is altered due to the fluid accelerated by these surfaces. This may serve to reduce the amplitude of vibrations and reduce the range of reduced velocities in which significant VIV occurs.

4.2 Delta Wing Design

The principle design of this configuration is the utilization of delta wings attached a set distance from the cylinder surface. A practical method with which to attach the delta wings to the cylinder surface was developed. A simple design was produced to allow for easy attachment and removal, as well as the capability to change the angle of attack of the wings. The design for the delta wing attachment mechanism is shown in Figure 4-1. A two-part hinge was fabricated that allows for pivoting of the wing surface in 10° increments. A screw attached the two parts of the hinge while a second screw locks the hinge into a set position. The connecting base of the hinge was adhered to the cylinder surface using an epoxy-resin putty. This allowed for easy removal and repositioning of the hinge location as desired. The delta wing itself was attached to the assembly through attachment points on the pivoting portion of the hinge. Both the hinge and delta wings were made of 0.06 inch thick sheet metal.

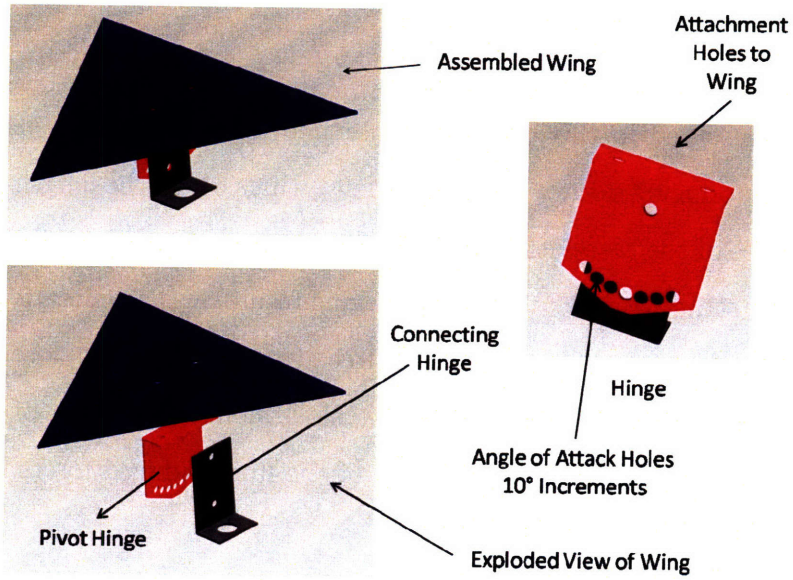

Figure 4-1: Drawings of the delta wings assembly. The assembly consists of the wing, pivot hinge and connecting hinge. The wing is connected by means of the pivoting hinge which allows for change in its angle of attack.

A number of different delta wings geometries were considered in this study. The dimensions of these wings are shown in Figure 4-2. Overall, three different types of wings were tested. Each wing was defined by its leading edge angle with the

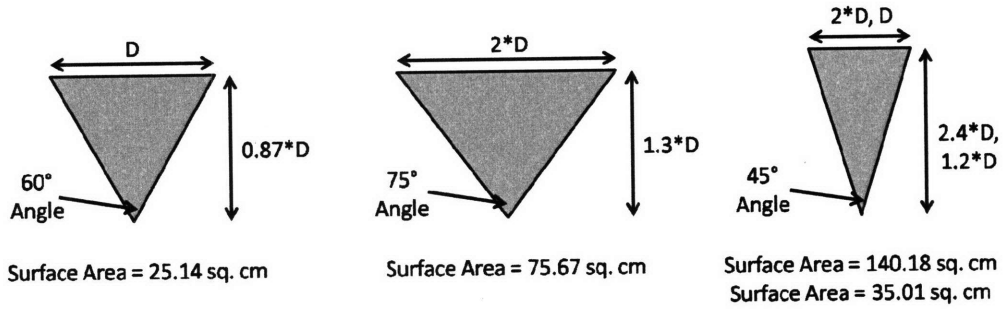

Figure 4-2: Dimensions of the delta wings tested. All of the delta wings were made from sheetmetal with a thickness of 0.02 inches. It is noted that two 45° angle wings of different sizes were investigated.

types investigated having a 60° (Equilateral), 75° and a 45° angle. Furthermore, two different size 45° ($S45°$ and $L45°$) wings were tested.

The delta wings were placed symmetrically about a center plane slicing through the cylinder. These sets of wings were placed along the length of the cylinder with a spacing of four cylinder diameters (4×D) and mounted at a height of one third a diameter (D/3) above the cylinder surface. Angles of attack within the range of −30° to 30° were considered in these experiments. Overall, twelve delta wings were simultaneously attached to the cylinder. These modified cylinders were tested in the tow tank at reduced velocities ranging from 3.5 to 10. Forces acting on the modified cylinder and its motion were recorded for each test conducted.

4.3 Position Data

For each test, the transverse position of the cylinder was recorded in order to determine the magnitude of its oscillations. A sample of this data from tests conducted using a bare cylinder is shown in Figure 4-4. Comparisons of the behavior exhibited by the cylinders modified with delta wings were made with the results from the bare cylinder. The position data from tests of the 75° at an angle of attack of 0° is also provided in Figure 4-4. It is clear that these relatively large wings had good performance in terms of damping out the oscillatory behavior of the cylinder. The smaller wings tested, the equilateral and smaller 45° angle wings, showed improvements over

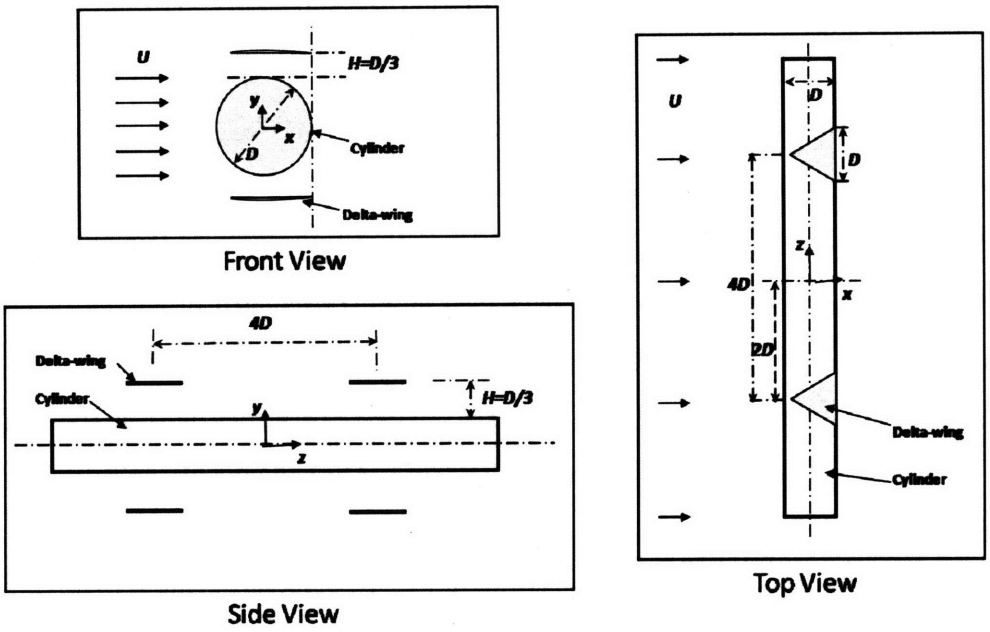

Figure 4-3: The attachment points of the delta wings to the cylinder are diagrammed in this figure. Each wing was attached with a spacing of 4 × D and a height of D/3. A total of 12 wings were attached to the test cylinder which had a length of 78.75 in., or 26.25 × D.

the bare cylinder case but were not quite as significant as those seen for the 75° and larger 45° angle wings. Although this increased damping is desirable, the larger size of these wings does pose mounting and structural concerns when transitioned to the scale of a riser. A full collection of time traces for all tests completed can be found in the Appendix of this document.

The performance of the delta wing enhancements based on oscillatory behavior is best seen by looking at the root mean square of the signal once the behavior has settled from its initial transitory behavior. This provides an indicator of the magnitude of oscillations about the mean position of the cylinder as it is towed down the length of the tow tank. The equation used for this calculation was,

$$\left(\frac{A}{D}\right)_{rms} = \sqrt{\frac{1}{n}\sum_{i=1}^{n} y_i^2} \tag{4.1}$$

where y_i is the recorded transverse position of the cylinder in terms of a normalized amplitude ratio (A/D). It is from this analysis that the performance of the wings is best seen in terms of their damping properties. Overall, the delta wings always produced positive results with varying degrees of success depending upon the shape of the wing and its angle of attack. The plots in Figure 4-6 to 4-9 provide a graphical representation of the rms(A/D) results from all configurations. The largest delta wings exhibited the greatest reduction in VIV with minimal improvements produced by the equilateral wings. The variation attributable to angle of attack is very noticeable with the best performance seen in the $-10°$ to $10°$ range. Thus, any recommendations for use would be for operation within this range. This provides a compelling reason for having a simplistic self-aligning mechanism which would allow the wings to automatically orient themselves to a 0° position with respect to the incoming flow.

The variation of performance can also be considered based solely on size and shape in a very limited manner due to the small number of wing designs tested. Two different sizes of the 45° wings were tested allowing for an initial idea of how the surface area of the wing will affect performance. Also, the smaller 45° wings had

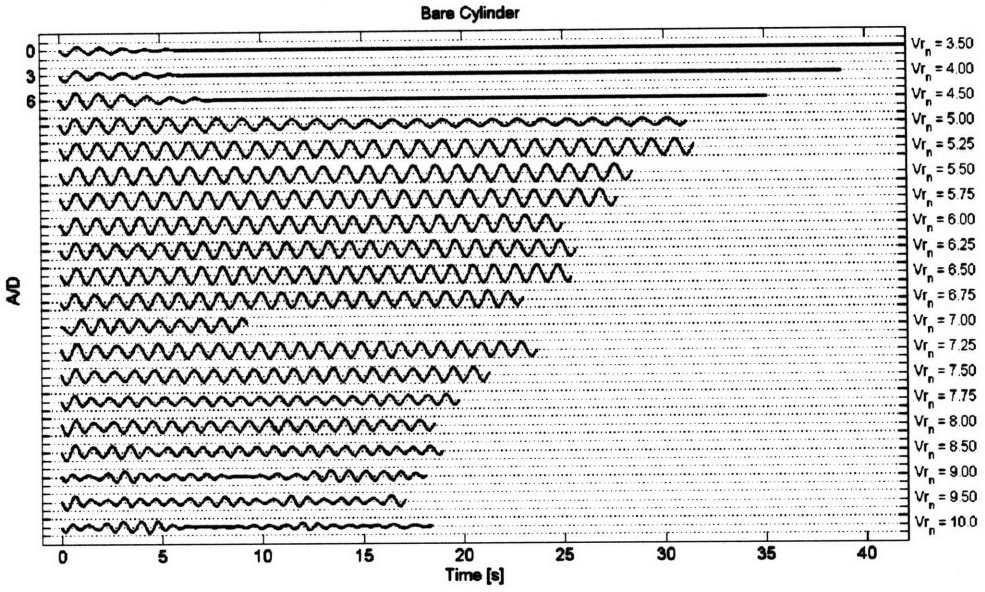

(a)

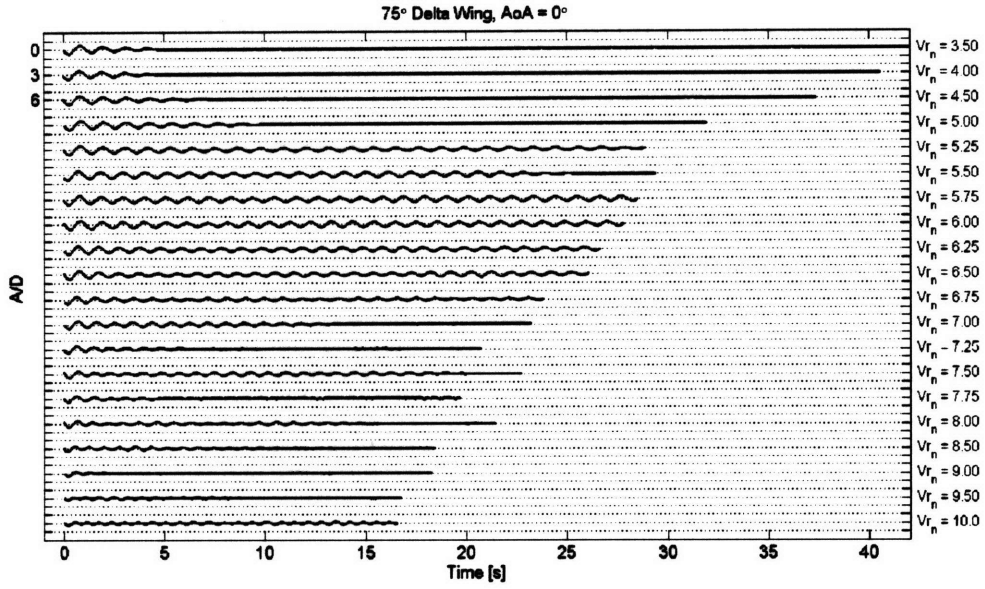

(b)

Figure 4-4: Time traces of the oscillatory behavior exhibited by (a) a bare cylinder and (b) cylinder modified with delta wings of leading edge angle of 75° and angle of attack of 0°.

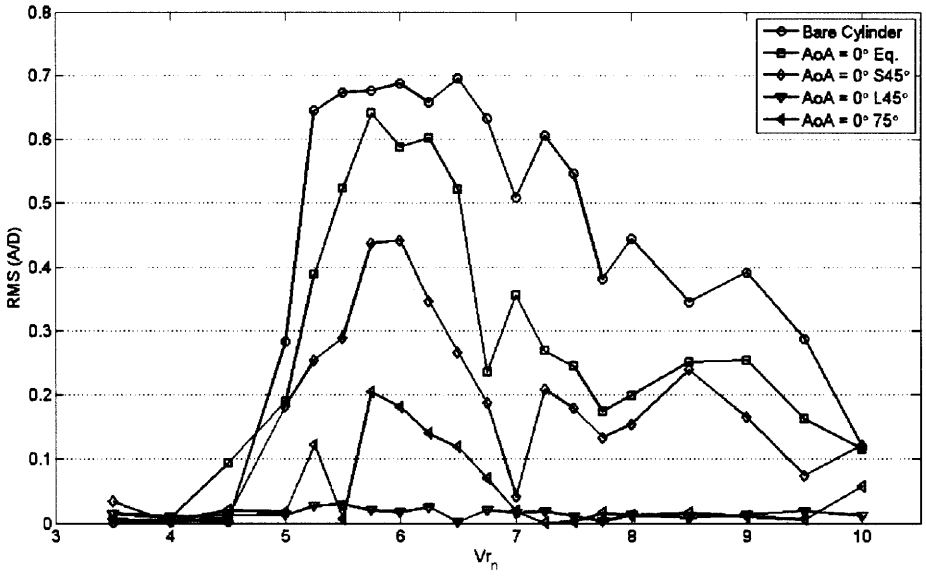

Figure 4-5: Comparison between delta wing geometries of rms(A/D) results.

a surface area close that of the equilateral wings allowing for shape effects to be considered. It is obvious from the data presented in Figure 4-5 that a larger wing will lead to lower amplitude oscillations that will diminish over time. The effect of the shape of the wing is a little harder to determine from the set of tests conducted. The smaller 45° wings had a surface area close to, but not exactly the same as the equilateral wings. Thus, the improved performance seen in the smaller 45° wings may be a result of this slightly increased size. However, it is possible that some of the improvement was derived from the change in the leading edge angle.

4.4 Drag

The other main focus of this study was the effect that the delta wings have on the drag force exerted on the cylinder. The normalized drag,

$$C_d = \frac{Drag}{0.5 \times \rho \times U^2 \times L \times D} \tag{4.2}$$

time trace is shown for the bare cylinder in Figure 4-10. From this data, a time-

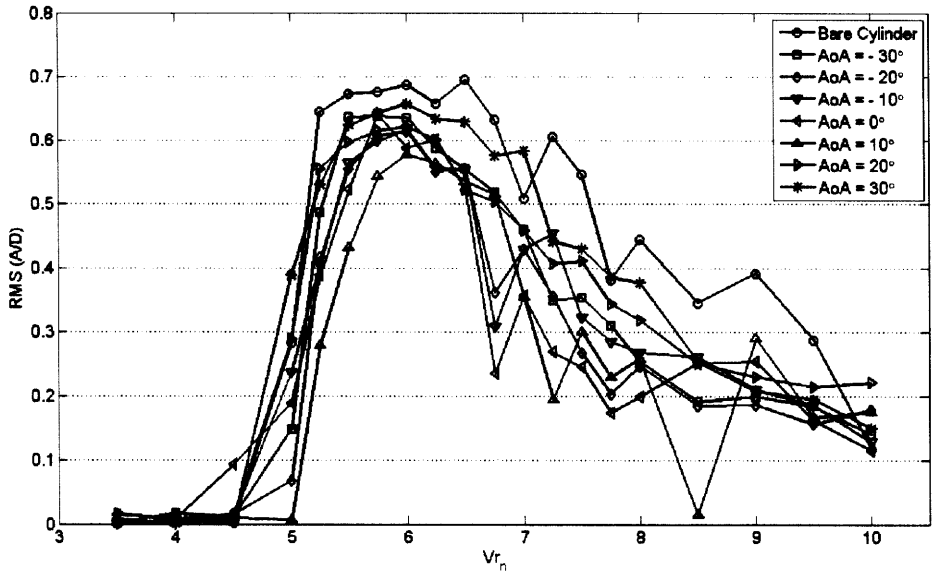

Figure 4-6: rms(A/D) data for a cylinder modified with equilateral delta wings.

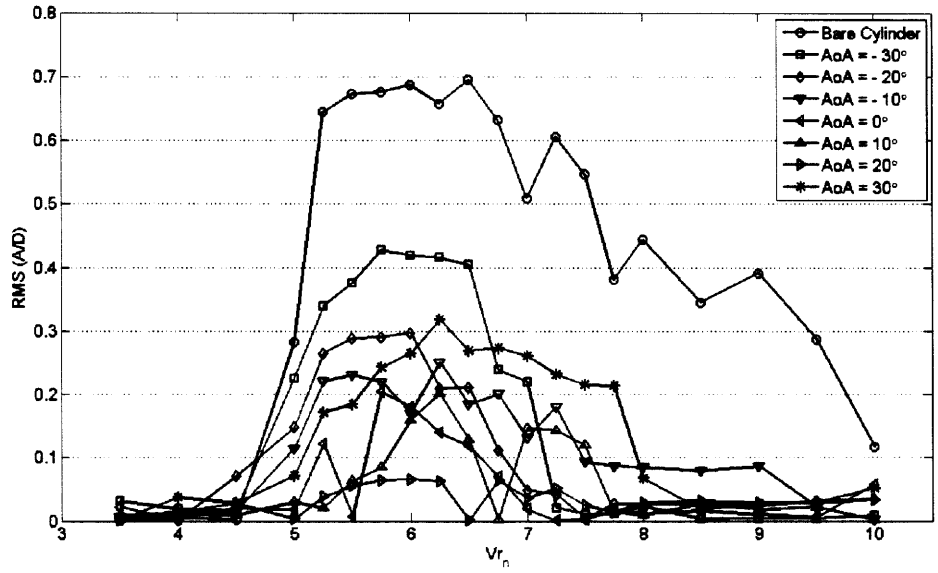

Figure 4-7: rms(A/D) data for a cylinder modified with 75° delta wings.

averaged drag coefficient, C_d, is obtained excluding the transient period of time. This provides a relevant means of comparing performance between different configurations.

Decreases in time-averaged drag were seen for all cases tested regardless of delta wing shape and size. However, the degree of change was influenced by these factors

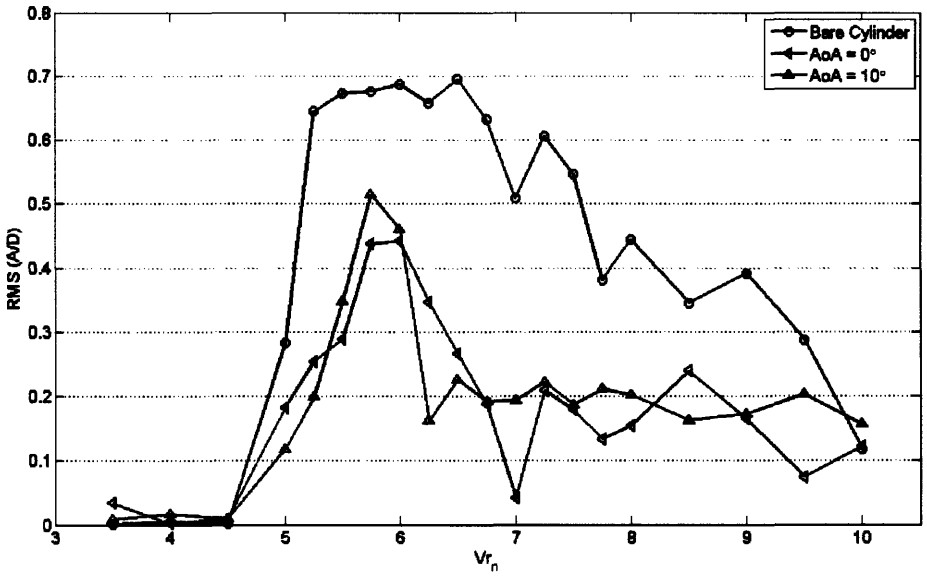

Figure 4-8: rms(A/D) data for a cylinder modified with $S45°$ delta wings.

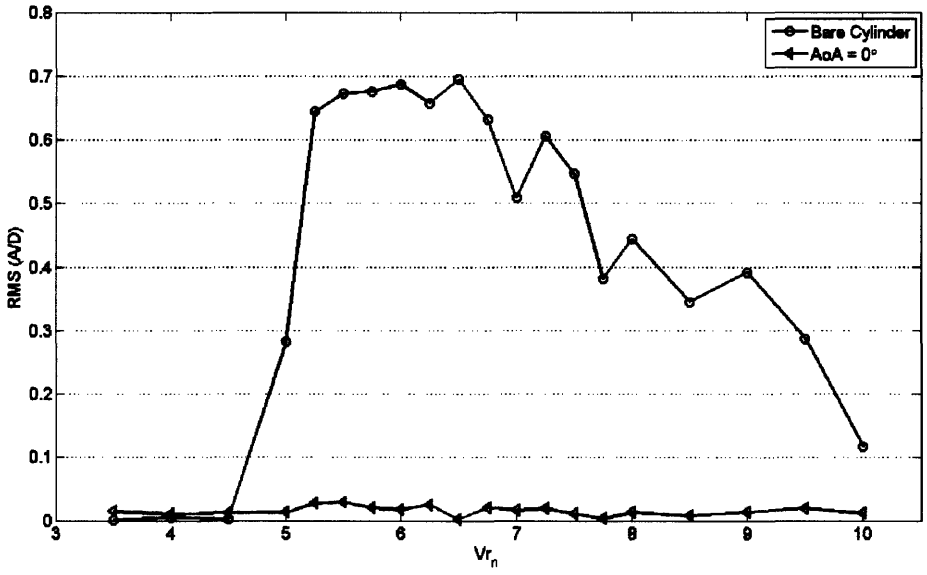

Figure 4-9: rms(A/D) data for a cylinder modified with $L45°$ delta wings.

as seen in Figure 4-11. Once again, the larger surface area wings outperformed the smaller wings considered in this study. The reduction in drag for these cases is likely attributable to the lower amplitude oscillations noted in Section 4.3. As a result, the best performer was the largest of them all, the large 45° wings. The wings that offered

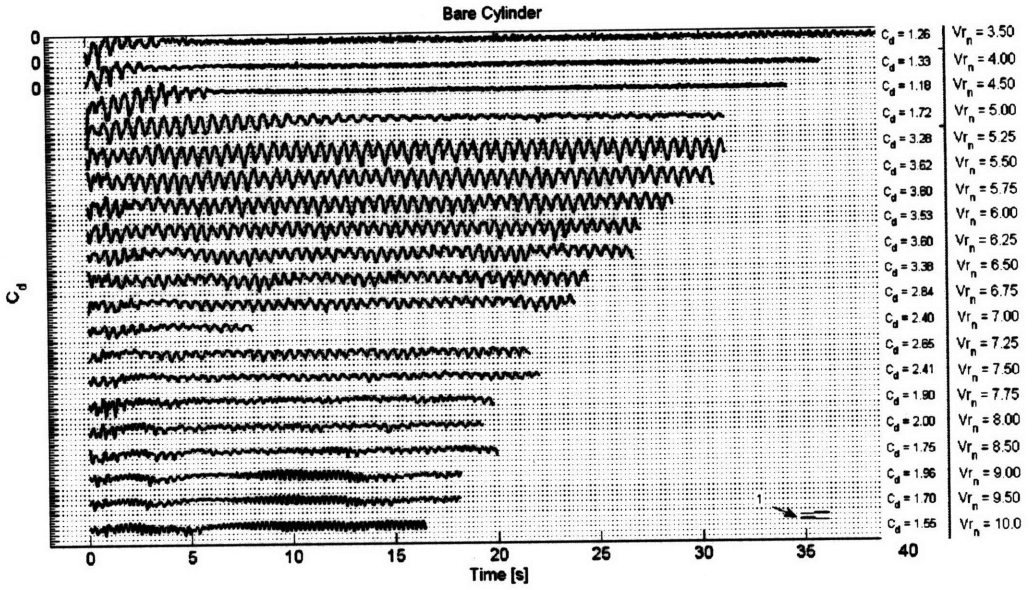

(a)

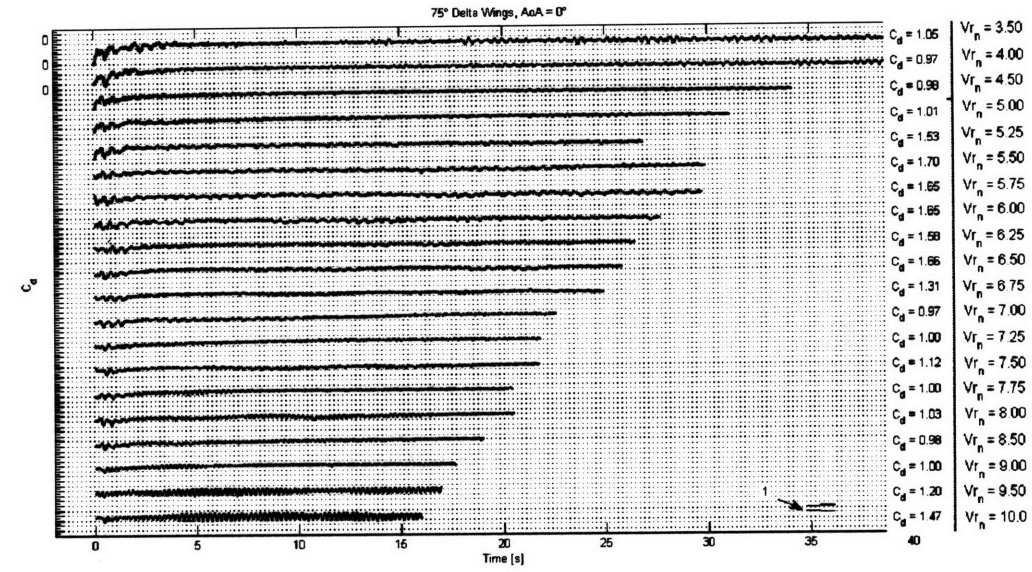

(b)

Figure 4-10: Time traces of the drag coefficient for a bare cylinder and (b) cylinder modified with delta wings of leading edge angle of 75° and angle of attack of 0°.

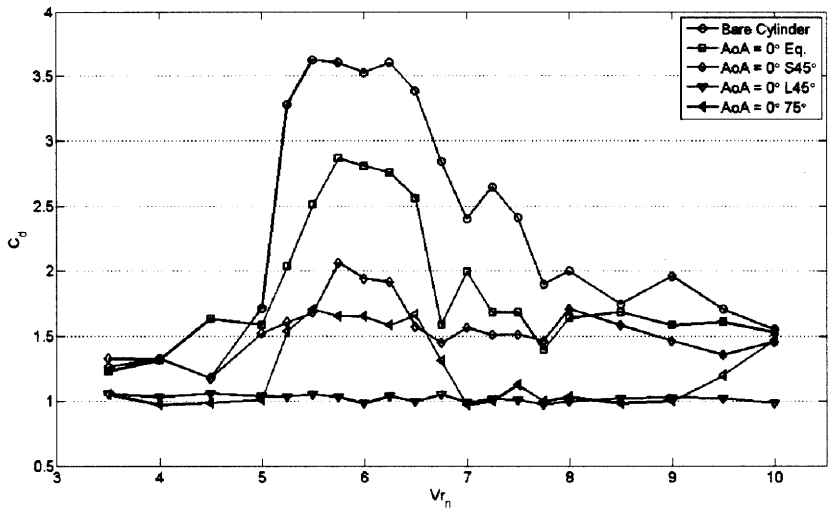

Figure 4-11: Comparison between delta wing geometries of drag coefficient results.

the least drag reduction were the equilateral wings. The smaller 45° wings fell between their larger counterpart and the equilateral wings in drag reduction performance. It is promising that both metrics of performance under consideration in this study behaved in the same manner for each set of wings. Both the drag and vibration damping benefits of the wings moved in a positive direction with the degree of this improvement mostly based on the size of the wings. These two phenomena are linked in a manner that makes attaining the dual goals of this study a possibility.

The plots presented in Figure 4-12 to 4-15 provide a graphical representation of the drag coefficient results from all configurations. Once again, the largest delta wings exhibited the best performance with minimal improvements produced by the equilateral wings.

4.5 Summary of Delta Wing Results

Overall, promising results were obtained from the delta wing modifications. Figure 4-16 shows an average percent difference between the two metrics discussed in this chapter compared to a bare cylinder over the reduced velocities tested. Reductions of up to 98% in rms(A/D) were seen with a corresponding reduction of 57% in the

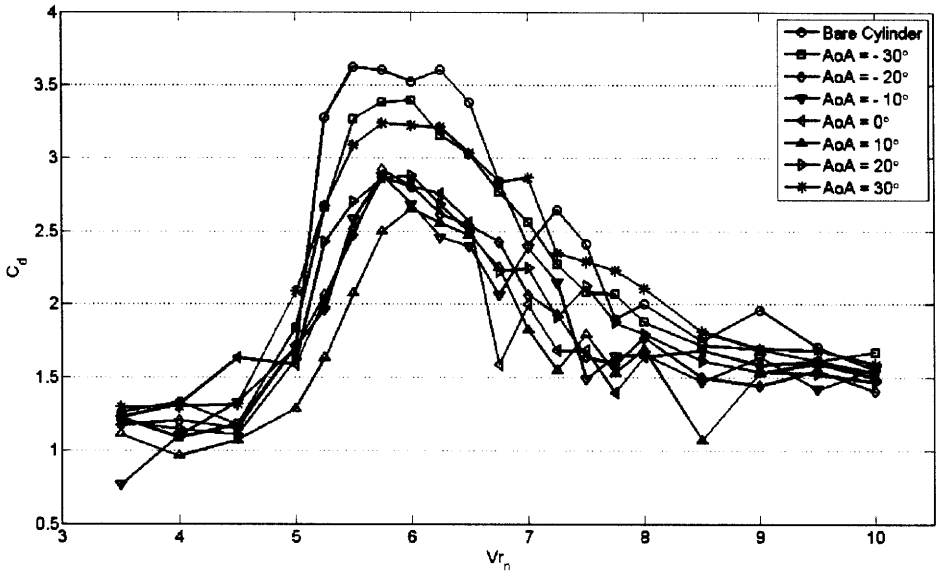

Figure 4-12: Drag coefficient data for a cylinder modified with equilateral delta wings.

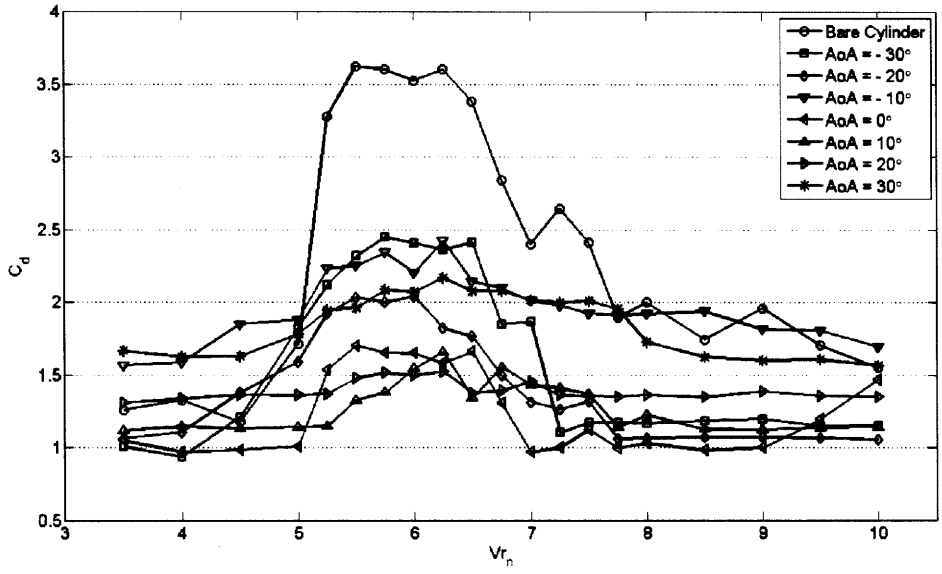

Figure 4-13: Drag coefficient data for a cylinder modified with 75° delta wings.

drag coefficient. These improvements were seen with the largest of the wings tested. Even the smallest wings provided improvements of up to 30% in RMS(A/D) and a corresponding 20% reduction in drag.

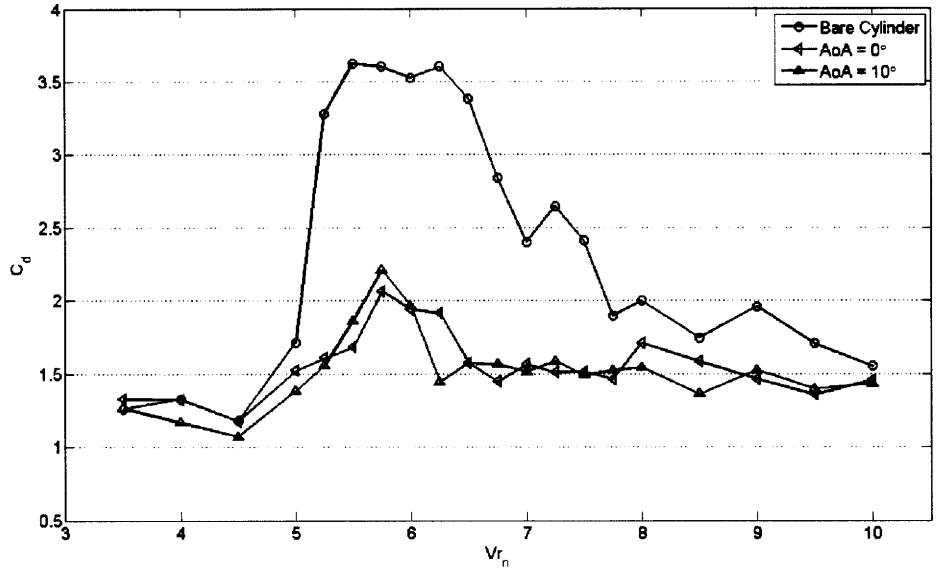

Figure 4-14: Drag coefficient data for a cylinder modified with $S45°$ delta wings.

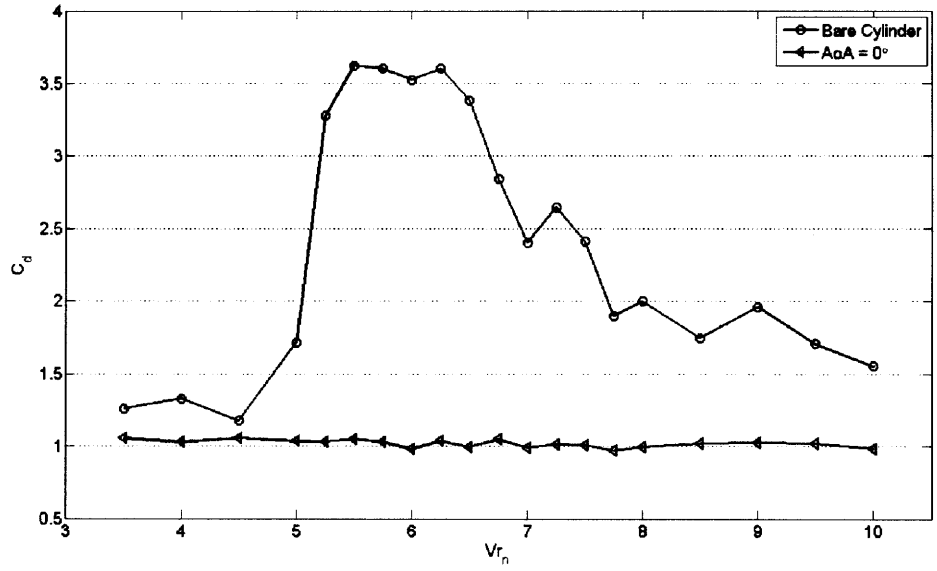

Figure 4-15: Drag coefficient data for a cylinder modified with $L45°$ delta wings.

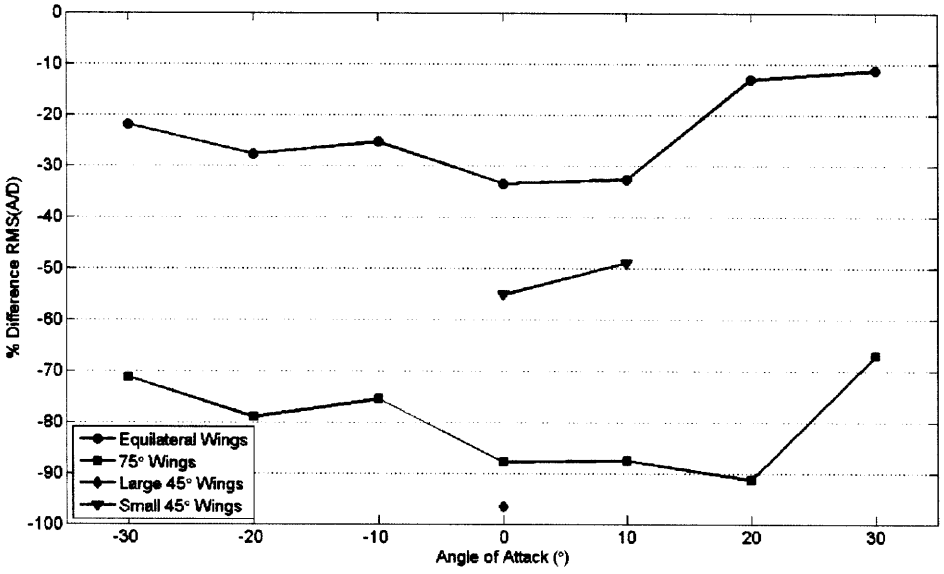

(a)

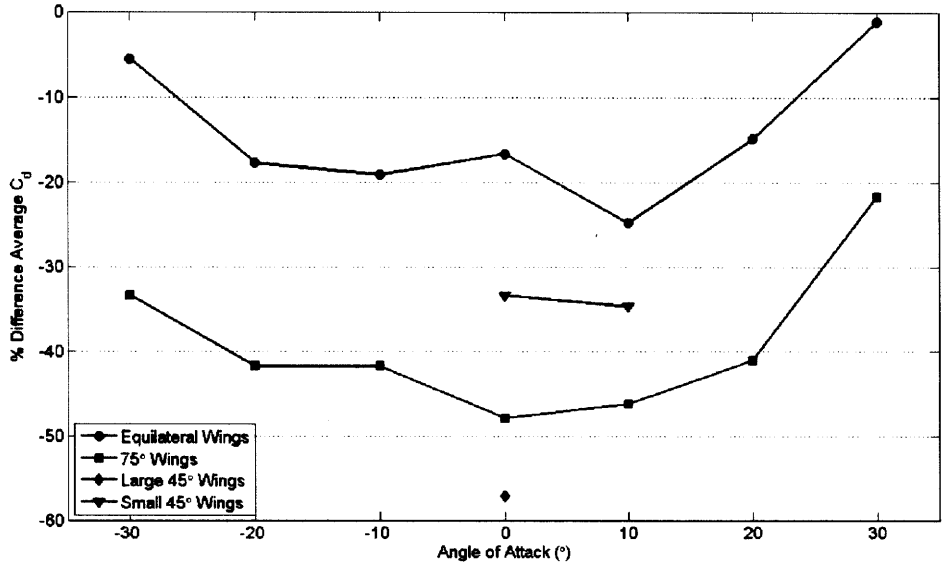

(b)

Figure 4-16:

Chapter 5

Vortex Generating Tabs

5.1 Overview

The motivation behind the Vortex Generating Tab configuration to be described in this chapter was similar to that for the Delta Wing Configuration. In this method, a number of small vortex generating tabs were attached to the cylinder along a helical path. These tabs were meant to introduce vortices into the wake in order to break up the spanwise vortex being shed from the cylinder. This shortens the correlation length of this structure and reduces the intensity of the forces acting on the cylinder and driving VIV.

Two differences arise from using tabs as compared to the horizontally mounted delta wings for VIV suppression. The first of these is the nature of the vortices to be introduced into the wake. The vortex shedding from a delta wing is such that the axis of vorticity is parallel with the direction of the free stream flow. Adding a vertical tab to the cylinder leads to shedding of vortices with a rotational axis aligned with the transverse direction. The second difference is that the tabs can be mounted in a helical fashion without concern of projecting large surface areas perpendicular to the free stream flow which would significantly increase drag. This helical arrangement allows for the approach to be less directionally sensitive by introducing vortices into the flow regardless of the direction of incoming flow.

5.2 Vortex Generating Tabs

The intended design of this configuration was to utilize small vortex generating surfaces arranged in a triple-start helix as depicted in Figure 5-1. The helical attachment design was conceived to minimize the directionality of this approach. However, in actual tests, only the tabs located on cylinder poles (locations 90° from the cylinder's stagnation points) were attached. This method of investigation attempted to use the tab/flow interaction to its fullest potential while minimizing the number of tabs being attached for each round of tests.

Multiple tab geometries and dimensions, as depicted in Figure 5-2 were investigated. The first set of tabs used were square with sharpened leading and trailing edges. Two different size tabs with side lengths of $\frac{1}{6}D$ and $\frac{1}{3}D$ were considered. Another geometry tested was of a right triangle with base and height dimensions of $\frac{1}{3}D$. The square tabs were made from lengths of aluminum bent at a 90° angle with a thickness of 0.1 inches. The edges of the square tabs were sharpened to a point to present a streamlined face to the flow. The triangular tabs were made from aluminum sheet metal with a thickness of 0.06 inches. All tabs were attached to the cylinder surface using an epoxy-resin putty.

5.3 Configurations Tested

The parameters, other than tab geometry, that could be altered for this suppression method were angle of attack and pitch of the helix (spacing between tabs). Furthermore, there were variations in the attachment method that included alternating the angle of attack (positive and negative) of sequential tabs. This method is labeled as alternating, while non-alternating refers to cases in which all tabs were aligned to have the designated angle of attack. Further variations were possible when testing the triangular tabs and are depicted in Figure 5-4 (note that the depicted configurations represent an alternating angle of attack design). These variations included aligning the tabs such that either the slanted or vertical edge of the triangle served as the

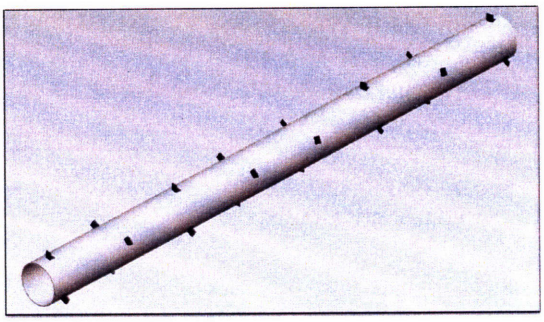

(a)

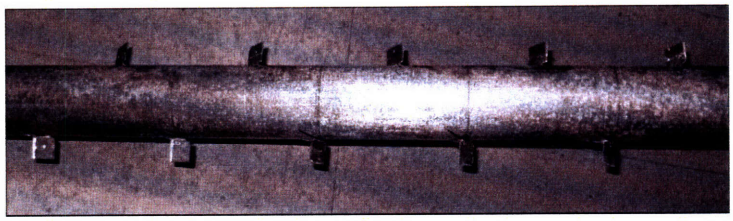

(b)

Figure 5-1: (a) Computer rendering of tab vortex generating configuration and (b) image of modified cylinder with square tabs.

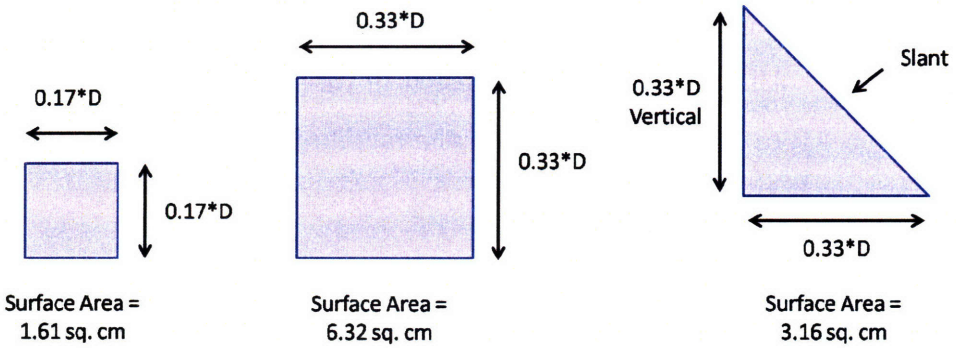

(a) (b) (c)

Figure 5-2: Diagrams depicting the shapes and dimensions of the tabs used: (a) small square tabs, (b) large square tabs and (c) triangular tabs.

Non-Alternating AoA

Square Tabs (0.17D x 0.17D)
- Pitch: 12D, AoA: 10°
- Pitch: 6D, AoA: 10°
- Pitch: 6D, AoA: 45°

Square Tabs (0.33D x 0.33D)
- Pitch: 6D, AoA: 45°

Right Triangle Tabs (0.33*D x 0.33*D)
- Pitch: 12D, AoA: 45°, Vertical LE (VLE)
- Pitch: 12D, AoA: 45°, Slanted LE (SLE)

Alternating AoA (+/-)

Square Tabs (0.33D x 0.33D)
- Pitch: 6D, AoA: +/- 5°
- Pitch: 12D, AoA: +/- 5°
- Pitch: 12D, AoA: +/- 10°
- Pitch: 12D, AoA: +/- 45°

Right Triangle Tabs (0.33D x 0.33D)
- Pitch: 6D, AoA: +/- 45°, Vertical LE (VLE)
- Pitch: 6D, AoA: +/- 45°, Slanted LE (SLE)
- Pitch: 6D, AoA: +/- 45°, Alternating LE (ALE)

Figure 5-3: List of tested vortex generating tabs configurations.

leading edge. Alternating the leading edges between slanted and vertical edges was also attempted. All configuration were tested in the tow tank at reduced velocities ranging from 3.5 to 10. Forces acting on the modified cylinder and its motion were recorded for each test conducted.

5.4 Experimental Results

The results from tests conducted on a cylinder modified with the vortex generating tabs described in this chapter did not exhibit significant reduction in VIV. Data (see description of RMS(A/D) in Chapter 4) presenting the dynamic behavior of the cylinder is shown in the proceeding plots. Non-altering configurations, regardless of

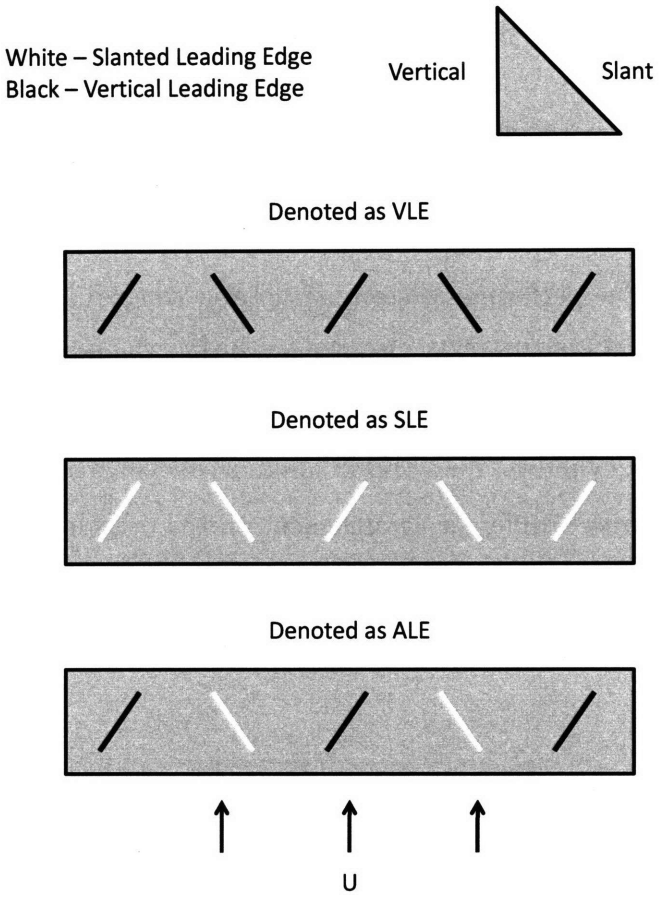

Figure 5-4: Graphical representation of various tab attachment variations for the triangular tabs.

size and geometry, did not result in a reduction of vibrations. Slight improvements were seen with the alternating configurations. Even then, peak values of rms(A/D) were comparable to those seen for the bare cylinder. Any reduction in vibrations that did occur were mostly confined to values of reduced velocity greater than seven. Despite little effect on vibrations for most cases, drag often showed a noticeable, but not significant decrease. This is an expected result considering that large scale oscillations continued to occur even with the modifications.

5.5 Summary of Vortex Generating Tabs Results

The vortex generating tabs explored in this work did not provide the desired and expected results. The performance seen using delta wings did not carry over to this attempted method of reducing VIV. It is believed that the tabs used were simply too small to produce large enough vortices to break up the coherence of the vortex tube being shed from the cylinder. With this in mind, a concept was conceived using larger vortex generators with a different arrangement on the cylinder. This modification is referred to as the "Rabbit Ear" method and is described in Chapter 6.

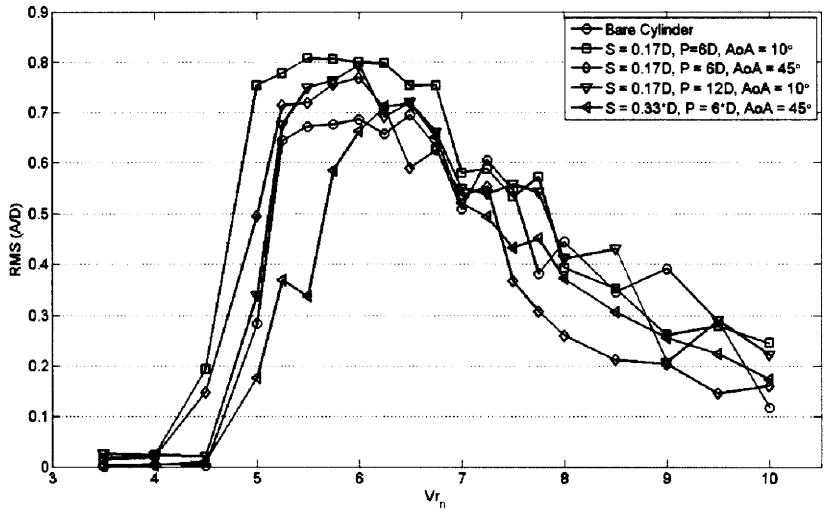

(a)

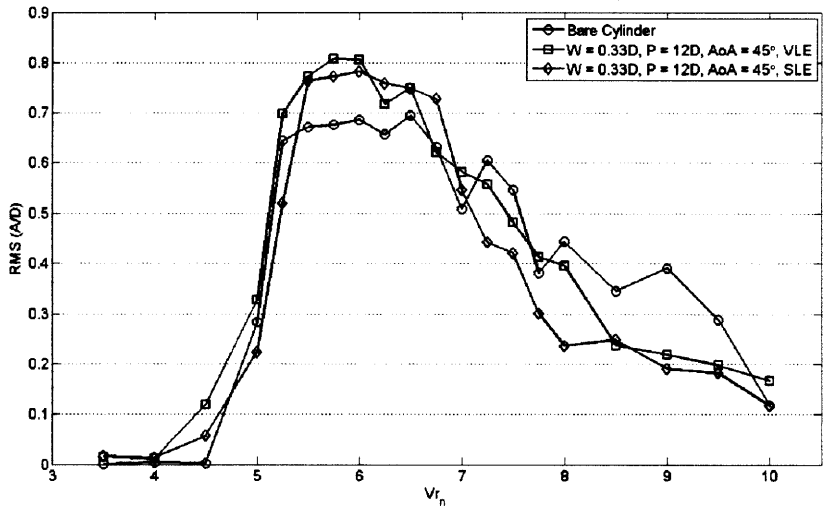

(b)

Figure 5-5: RMS(A/D) for non-alternating angle of attack a.) square and b.) triangular vortex generating tab configuration.

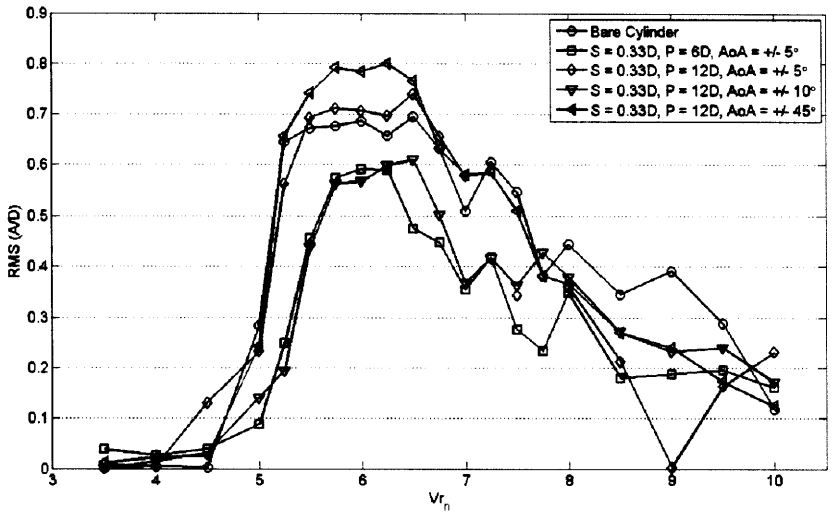

(a)

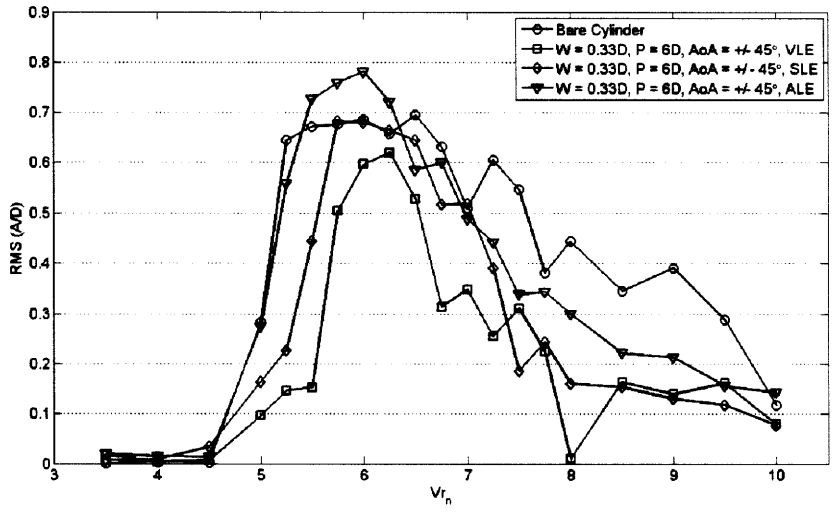

(b)

Figure 5-6: RMS(A/D) for alternating angle of attack a.) square and b.) triangular vortex generating tab configuration.

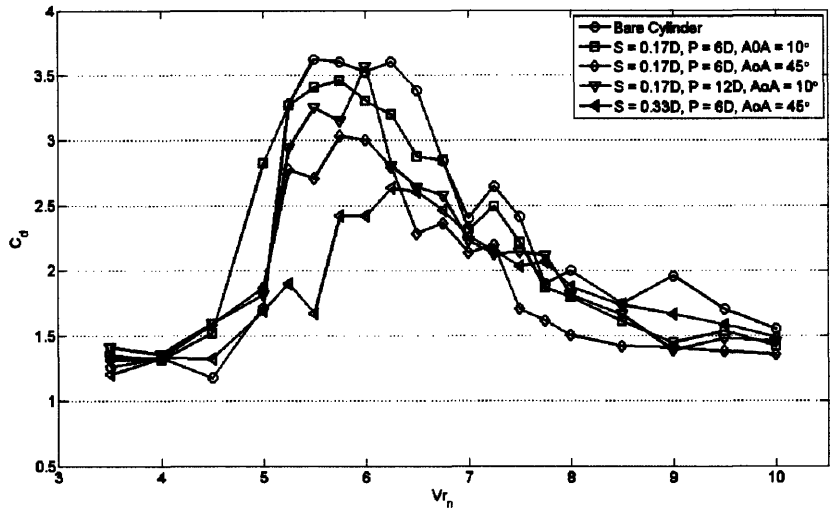

(a)

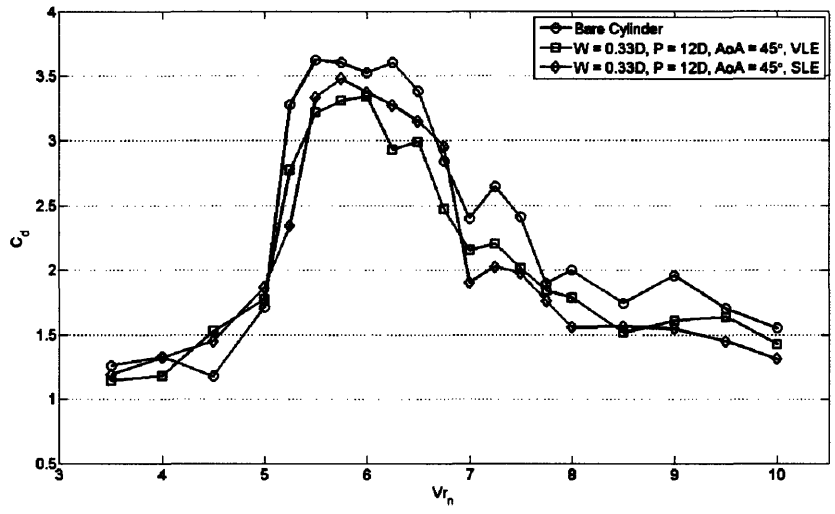

(b)

Figure 5-7: Drag coefficients for non-alternating angle of attack a.) square and b.) triangular vortex generating tab configuration.

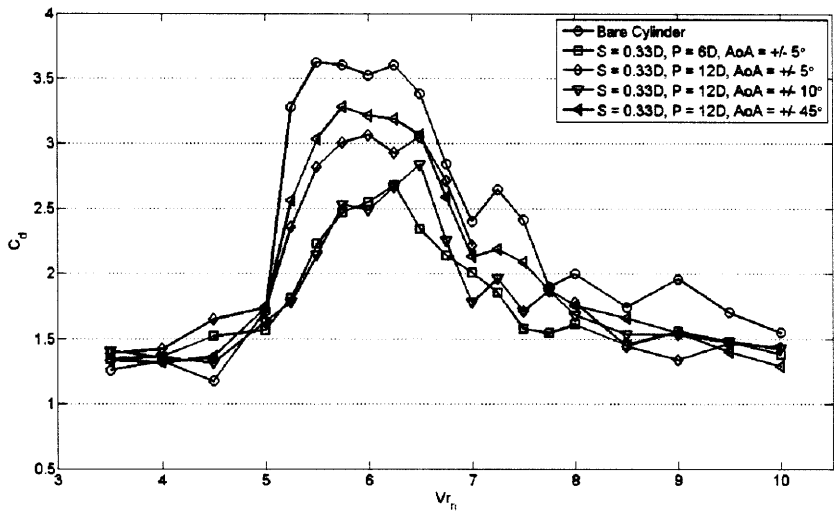

(a)

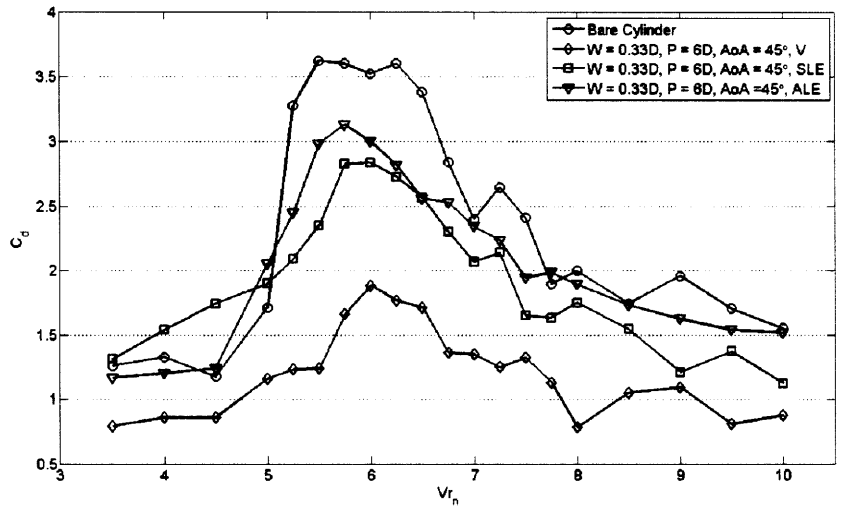

(b)

Figure 5-8: Drag coefficients for alternating angle of attack a.) square and b.) triangular vortex generating tab configuration.

Chapter 6

Rabbit Ears

6.1 Concept

The relative success of the delta wings provided evidence that the introduction of vortices into the typical wake of a cylinder can act to reduce or even eliminate vortex induced vibrations. Breaking up the spanwise behavior of shedding from the cylinder appears to provide these sought after results. However, the size of the wings required for complete vibration suppression are quite large. There is also the possibility that the improvements are only brought about by the increased damping of the delta wings. As a result, the concept of halving the delta wings and forming a vortex generating pair with the two halves was considered. The "Rabbit Ears" configuration allows for some insight to be gained regarding the cause of improvement. The added damping of the tabs is less than that of the horizontally mounted wings, but the vortex formation should be comparable. Equivalent results would suggest that the spanwise breakup of vortex shedding provides the most significant mechanism for VIV reduction.

Furthermore, the attachment of the delta wings potentially presents some challenges in that they would most likely be attached at site due to transport difficulties of the combined structure. The "Rabbit Ear" approach has the potential of having the tabs form a type of flap that could be folded up against the cylinder surface and deployed at the site by unfolding them upward to the desired angle. Also, the delta wings provide a method of VIV suppression that is sensitive to flow direction. The

"Rabbit Ear" tabs could be arranged around the circumference of the cylinder to provide benefits from multiple directions with a compromise of decreased performance when the flow does not entirely align with a series of tab pairs.

6.2 "Rabbit Ears" Configuration

A combination of the "Delta Wing" and "Vortex Generating Tab" configuration was attempted and referred to as "Rabbit Ears". This arrangement utilized tabs with a triangular geometry meant to represent half of the small, horizontally mounted 45° delta wings tested. A number of different parameters were used to define this configuration as depicted in Figure 6-1. These parameters are

- h: The length of the trailing edge of the tab
- c: The chordlength of the tab
- s: Inter-pair spacing distance
- p: Distance between pairs
- ϕ: Angle of attack of the tab with reference to the free stream
- θ: Inclination angle of the tab with reference to the cylinder surface
- S: Refers to pairs of tabs being placed at the same spanwise positions on opposing sides of the cylinder

The tabs for this configuration were constructed from sheetmetal with a thickness of 0.06 inches. The idealized tabs depicted in the parameter diagram (Figure 6-1) were slightly modified as shown in Figure 6-2. The extensions added to the triangular section were made in order to reduce gaps between the vortex generating tab and the cylinder surface. This was done with the intention of increasing the amount of flow passing over the tab surface.

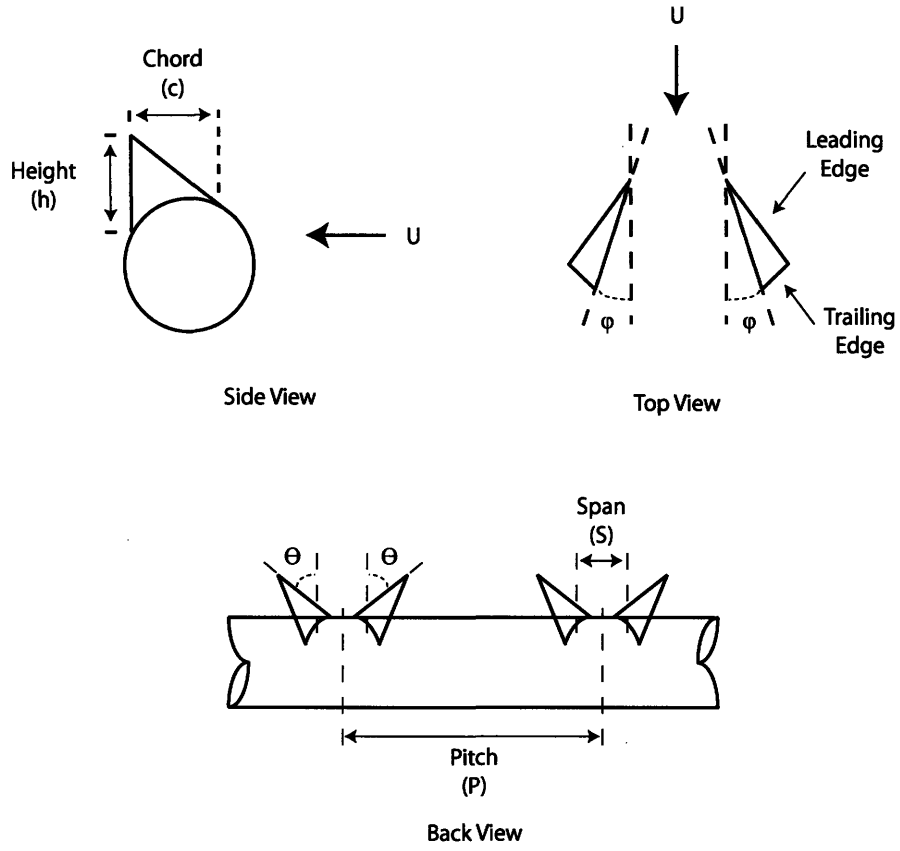

Figure 6-1: Graphical representation of the parameters defined for the "Rabbit Ear" configuration.

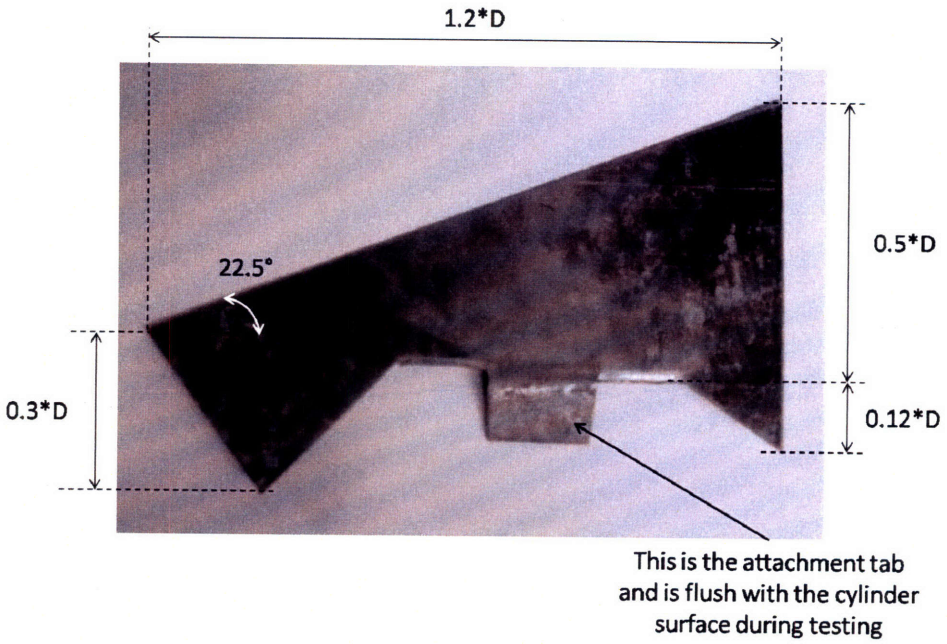

Figure 6-2: Image of a tab used in the "Rabbit Ear" configuration.

6.3 Configurations Tested

A total of thirty-one different configurations of the parameters outlined were investigated. Alterations in all parameters were made except for the geometry of the tabs. The height and chord were held constant at $0.5D$ and $1.2D$, respectively. A number of tests were conducted with an arrangement that did not involve staggered pairs, while the rest were staggered. All configurations are tabulated in Figure 6-3.

6.4 Experimental Results

Graphically presenting the rms(A/D) data (see Chapter 4 for details) collected from experiments allows for easy comparison between configurations of the effect on vibrations. An inclination angle of 45° only provided noteworthy improvement when staggered as seen in Figure 6-4. The configurations in which tab pairs were located symmetrically about the centerline of the cylinder demonstrated very little effect on vibrations. Only minimal improvements were seen once the pairs were staggered regardless of changes in other parameters.

Configuration	Height	Chord	Span	Pitch	AoA (ϕ)	Incl. Angle (θ)	Staggered	Pairs
1	0.5*D	1.2*D	0.5*D	4*D	10	45	N	12
2	0.5*D	1.2*D	0.5*D	4*D	0	45	N	12
3	0.5*D	1.2*D	1*D	4*D	0	45	N	12
4	0.5*D	1.2*D	2*D	4*D	0	45	N	12
5	0.5*D	1.2*D	2*D	4*D	30	45	N	12
6	0.5*D	1.2*D	1*D	5*D	0	45	Y	7
7	0.5*D	1.2*D	1*D	4*D	0	45	Y	11
8	0.5*D	1.2*D	0.5*D	4*D	0	45	Y	11
9	0.5*D	1.2*D	0.3*D	4*D	0	45	Y	11
10	0.5*D	1.2*D	0.5*D	4*D	20	45	Y	11
11	0.5*D	1.2*D	1*D	4*D	20	45	Y	11
12	0.5*D	1.2*D	1*D	3*D	20	45	Y	13
13	0.5*D	1.2*D	0.5*D	3*D	20	45	Y	13
14	0.5*D	1.2*D	1*D	4*D	0	30	N	12
15	0.5*D	1.2*D	1*D	4*D	0	30	Y	11
16	0.5*D	1.2*D	1*D	4*D	10	30	Y	11
17	0.5*D	1.2*D	1*D	4*D	-10	30	Y	11
18	0.5*D	1.2*D	1*D	4*D	0	150	Y	11
19	0.5*D	1.2*D	1*D	4*D	10	150	Y	11
20	0.5*D	1.2*D	1*D	4*D	-10	150	Y	11
21	0.5*D	1.2*D	1*D	4*D	0	15	Y	11
22	0.5*D	1.2*D	1*D	4*D	10	15	Y	11
23	0.5*D	1.2*D	1*D	4*D	-10	15	Y	11
24	0.5*D	1.2*D	1*D	4*D	0	165	Y	11
25	0.5*D	1.2*D	1*D	4*D	10	165	Y	11
26	0.5*D	1.2*D	1*D	4*D	-10	165	Y	11
27	0.5*D	1.2*D	0.75*D	4*D	0	30	Y	11
28	0.5*D	1.2*D	1.25*D	4*D	0	30	Y	11
29	0.5*D	1.2*D	1*D	5*D	0	30	Y	7
30	0.5*D	1.2*D	1*D	3*D	0	30	Y	13
R1	0.5*D	1.2*D	R	R	0	30	N/A	N/A

Figure 6-3: "Rabbit Ear" configurations tested.

Reducing the inclination angle to 30° resulted in notable improvement, especially toward the higher end of reduced velocities tested. It is noted that vortex production from the tabs can be altered by changes in angle of attack and inclination angle. It may be that the higher inclination of 45° places these "half delta wings" into a regime of stall. Such a result would inhibit the generation of strong vortices that are desired in order to break up the vortex structure shed form the cylinder. Lowering the inclination may return these tabs to an angle with the incoming flow that supports vortex production, thus resulting in more significant suppression of VIV. Further modification to lower inclination angles and inversion of the foils to have them inclined into one another ($\theta > 90°$)mostly maintained these effects.

Improved drag performance is in agreement with the reductions seen in VIV. Non-staggered configurations with an inclination of 45° exhibited the least significant reductions in drag. Adopting lower inclination angles led to a slight improvement. Reductions in drag over all reduced velocities tested for inclination angles other than 45° averaged about 30%. This is compared to a reduction of about 20% for configurations with the higher inclination from the cylinder surface.

6.5 Determination of Benefits

All configurations led to overal reductions in vortex induced vibrations as well as flow induced drag on the structure. The benefits of the modifications are quantified by considering the area underneath rms(A/D) and drag coefficient curves. This provides a method of comparison between each configuration across the range of reduced velocities considered. The rms value of the normalized amplitude was raised to the fourth power to provide a relation to fatigue in a steel structure. The connection between stress and fatigue is modeled by

$$N \times S^b = A \tag{6.1}$$

The variables in the equation are A and b, which are experimentally derived constants where $b = 4$, N, the number of cycles until fatigue occurs and, S, the

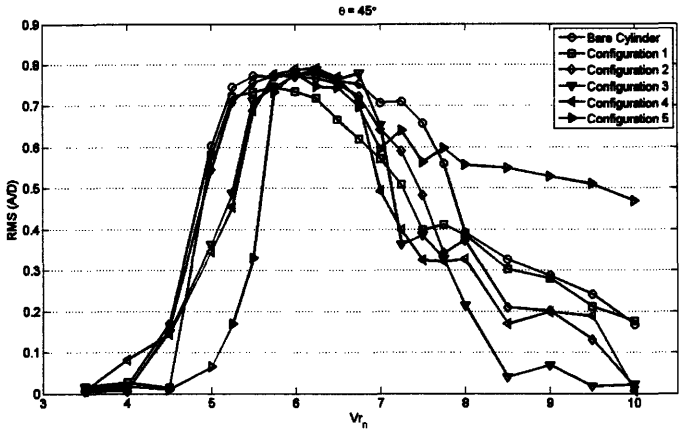

(a)

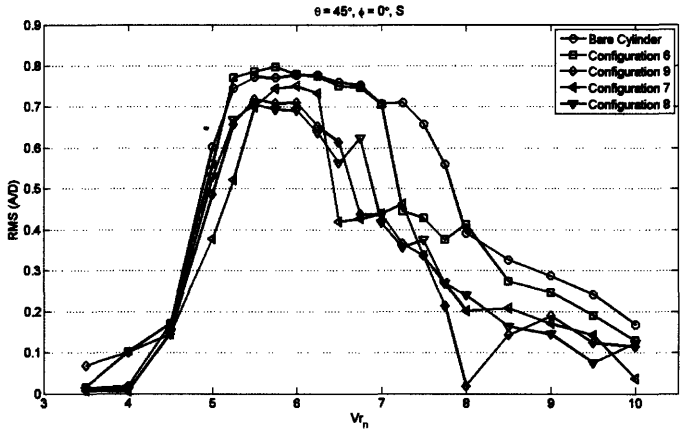

(b)

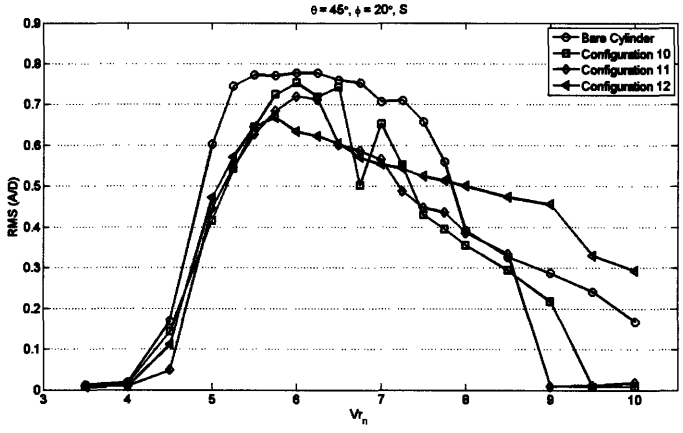

(c)

Figure 6-4: rms(A/D) data for "Rabbit Ear" configurations with an inclination angle of 45°.

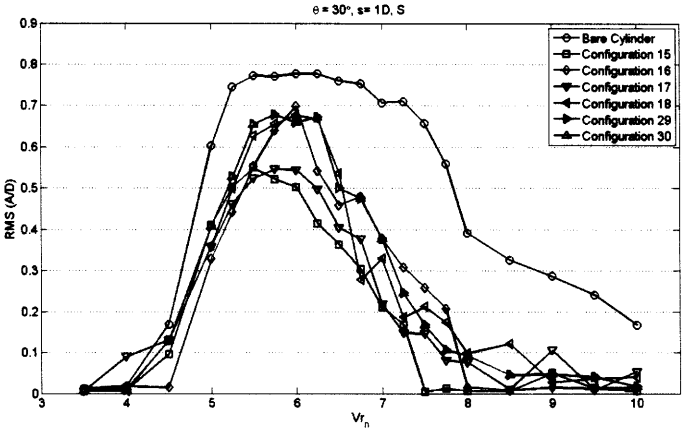

(a)

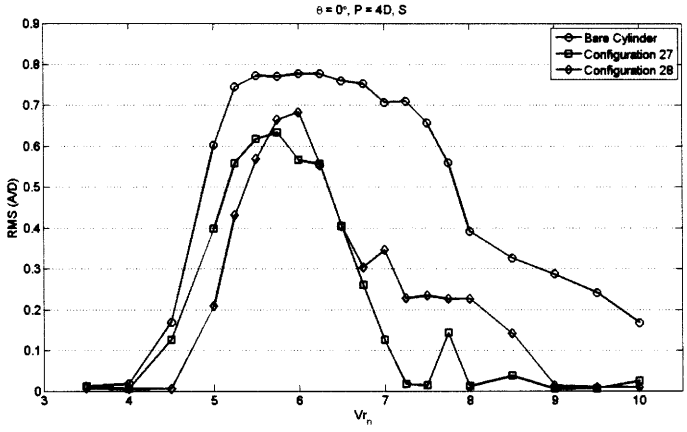

(b)

Figure 6-5: rms(A/D) data for "Rabbit Ear" configurations with an inclination angle of 30°.

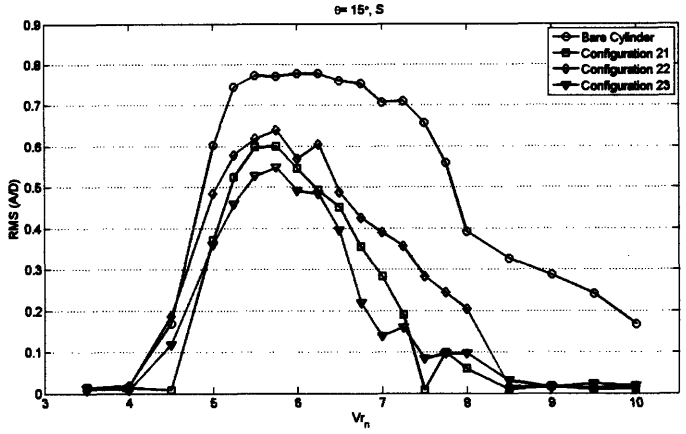

(a)

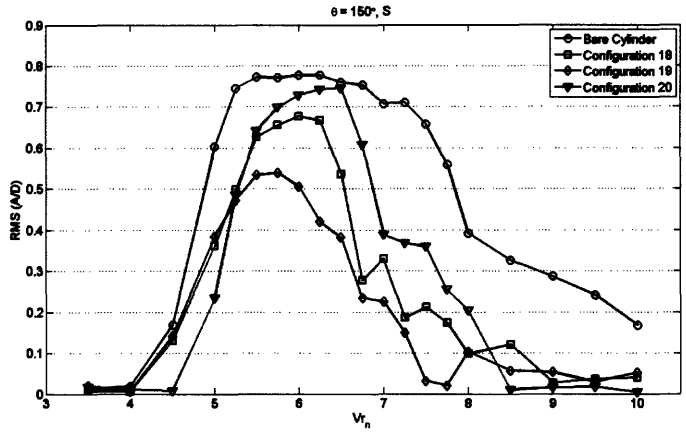

(b)

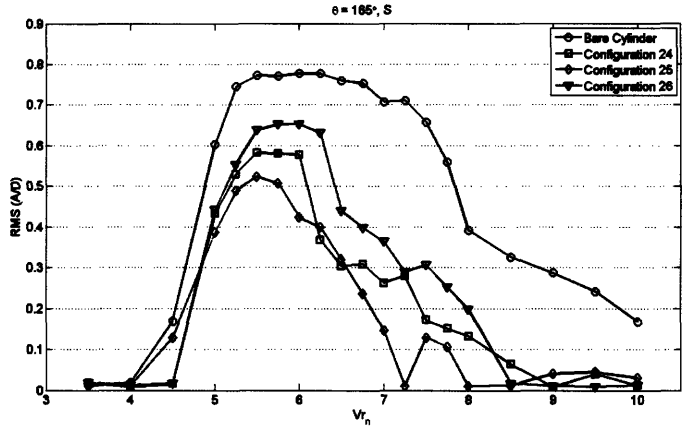

(c)

Figure 6-6: rms(A/D) data for "Rabbit Ear" configurations with an inclination angle of (a) 15°, (b)B 150° and 165°.

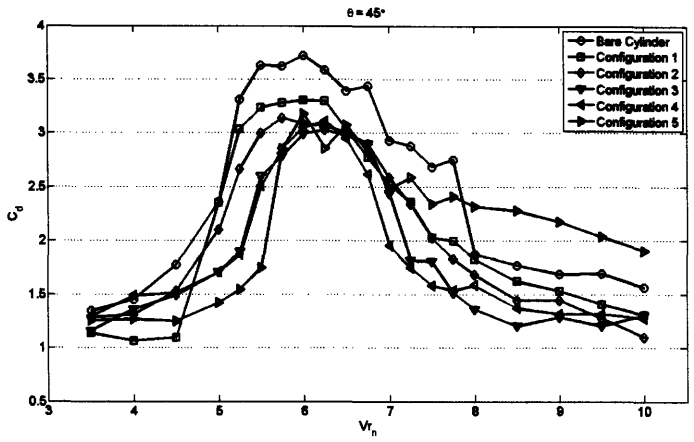

(a)

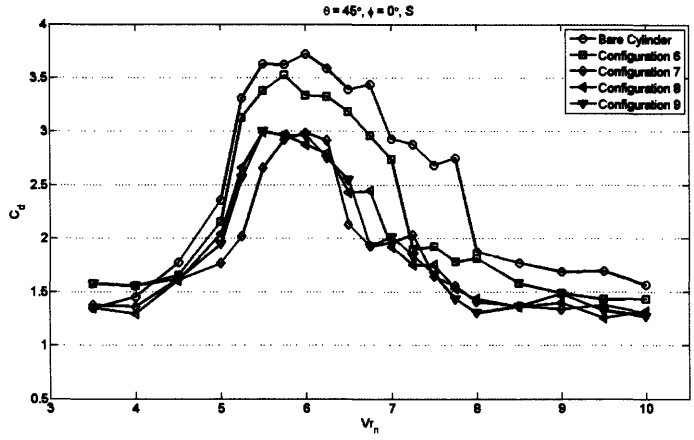

(b)

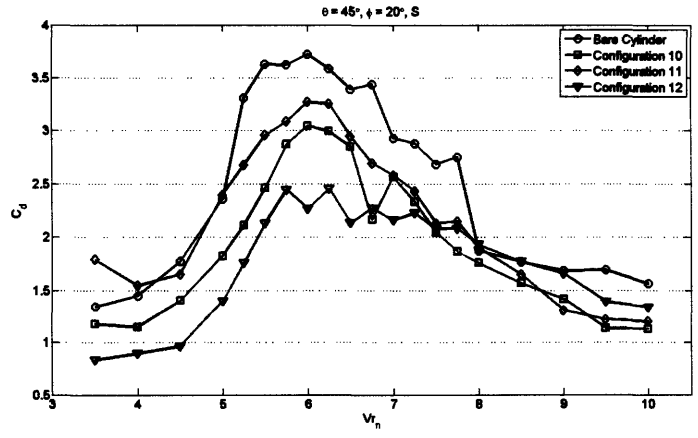

(c)

Figure 6-7: Drag coefficients for "Rabbit Ear" configurations with an inclination angle of 45°.

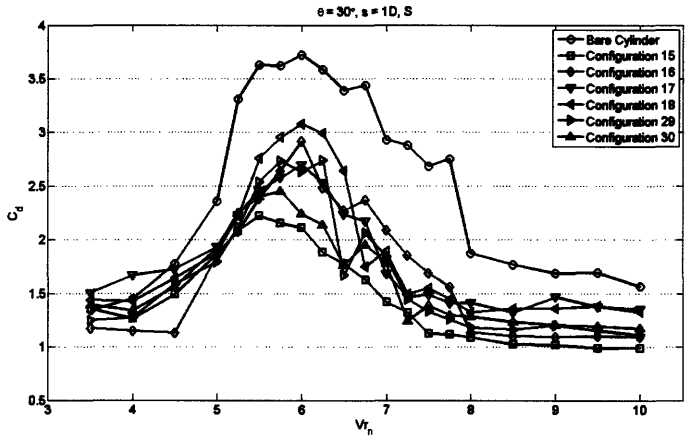

(a)

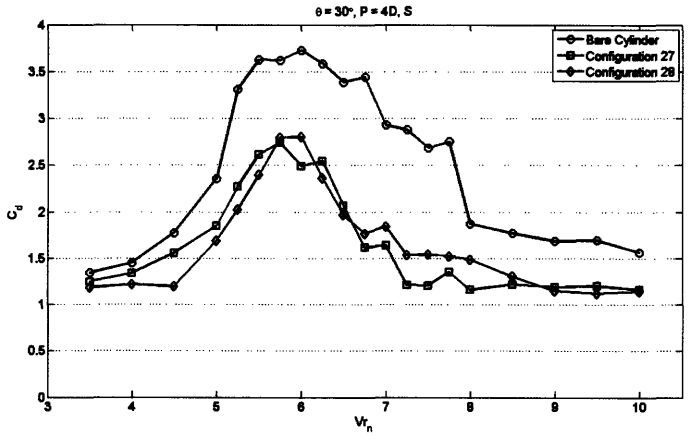

(b)

Figure 6-8: Drag coefficients for "Rabbit Ear" configurations with an inclination angle of 30°.

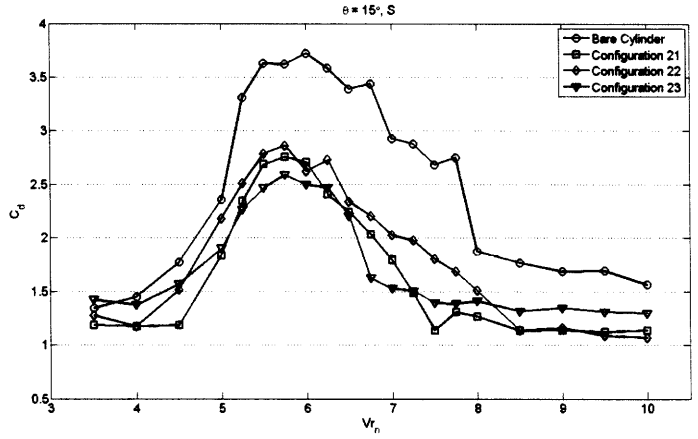

(a)

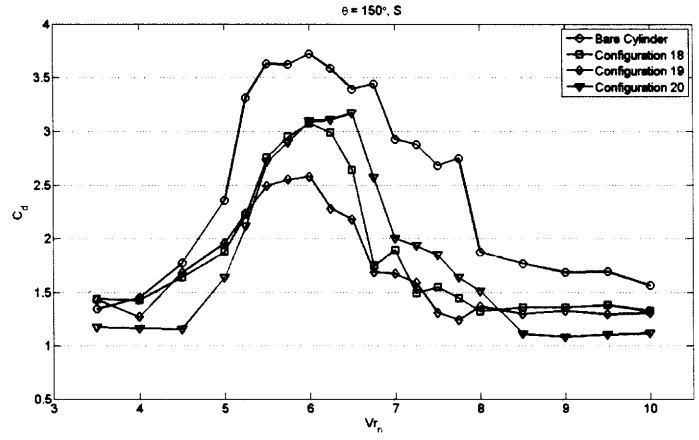

(b)

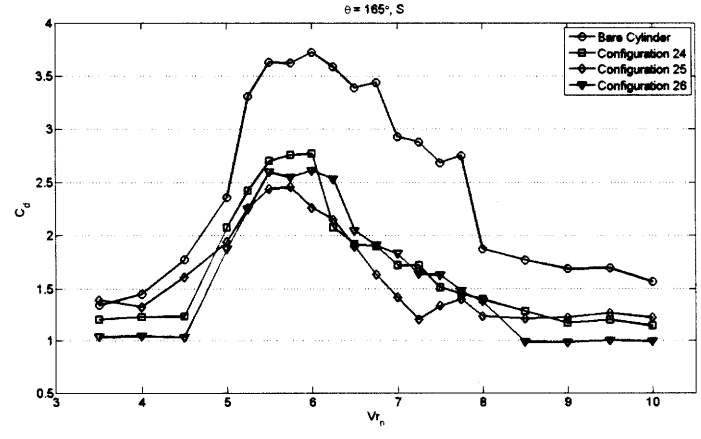

(c)

Figure 6-9: Drag coefficients for "Rabbit Ear" configurations with an inclination angle of (a) 15°, (b)B 150° and 165°.

magnitude of stress acting on the structure [5]. The stresses are a function of the forces exerted on the structure by the fluid which in turn are related to the vibrations of the structure. Thus, as a means of quantifying the effect in VIV reduction on the structure's longevity, the rms(A/D) values derived from experimentation were raised to the fourth power. The area under the rms(A/D) vs. Vr_n curve further provides a means of comparing configuration effects across the range of reduced velocities explored. A configuration may attain a lower maximum oscillation amplitude but may sustain this behavior across a wide range of reduced velocities, thus reducing the benefit of the reduction. By considering the area underneath the entire curve, a comparison can be made based on the overall performance of the system in multiple flow conditions.

The same view is carried over to consideration of the reduction in drag exerted on the modified cylinder. The overall minimum drag coefficient value derived from experiments for the "Rabbit Ear" configurations was used to normalize all other data points. The area under this normalized drag coefficient curve across the range of reduced velocities considered was calculated. The benefits of these reductions are presented in Figure 6-10. The data points indicate that all configuration succeeded at reducing overall vibrations and drag as compared to the bare cylinder. Points located closer to the bottom left corner of the plot represent those configurations with the best combined performance. Configurations with an inclination angle of 45° demonstrated the least effect on VIV. Adjusting the inclination to lower values improved performance. Angles of 15°, 30° and their supplementary angles of 165°, 150° improved performance with a clustering of results.

Maximum reductions were seen with Configuration 15 where the integral of the $rms(A/D)^4$ and of the normalized drag coefficient curves were reduced by 88% and 62% respectively. Slight modifications of the parameters that define Configuration 15 were made in order to view the effects of each parameter independently on performance. The results shown in Figure 6-11 suggest that modification of almost any parameter led to significant changes in the performance of the "Rabbit Ears". One exception is seen in decreasing the angle of attack to a value of 15°. Only slight

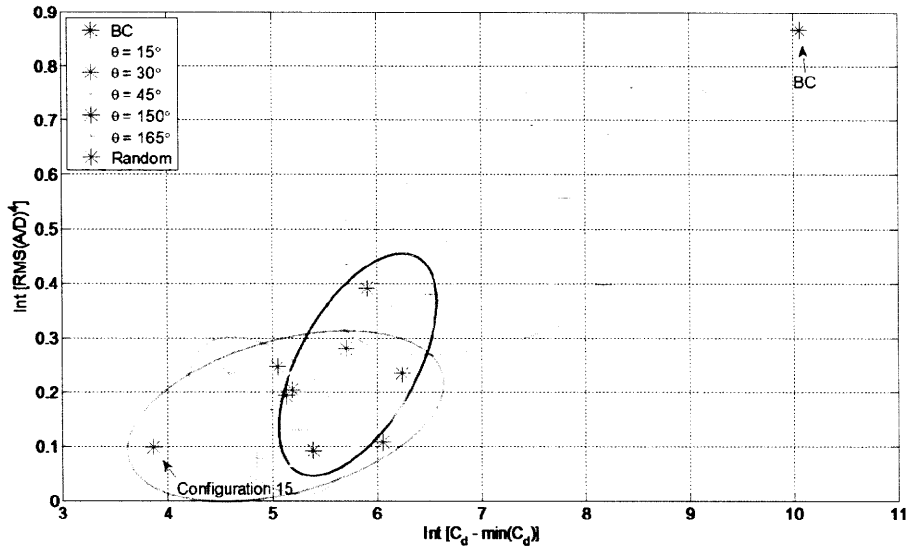

Figure 6-10: Measure of impact on vibrations and drag.

changes were noticed for this alteration indicating that decreasing the angle of attack of the tabs is not as crucial as other parameters assuming that the value is kept below 30°.

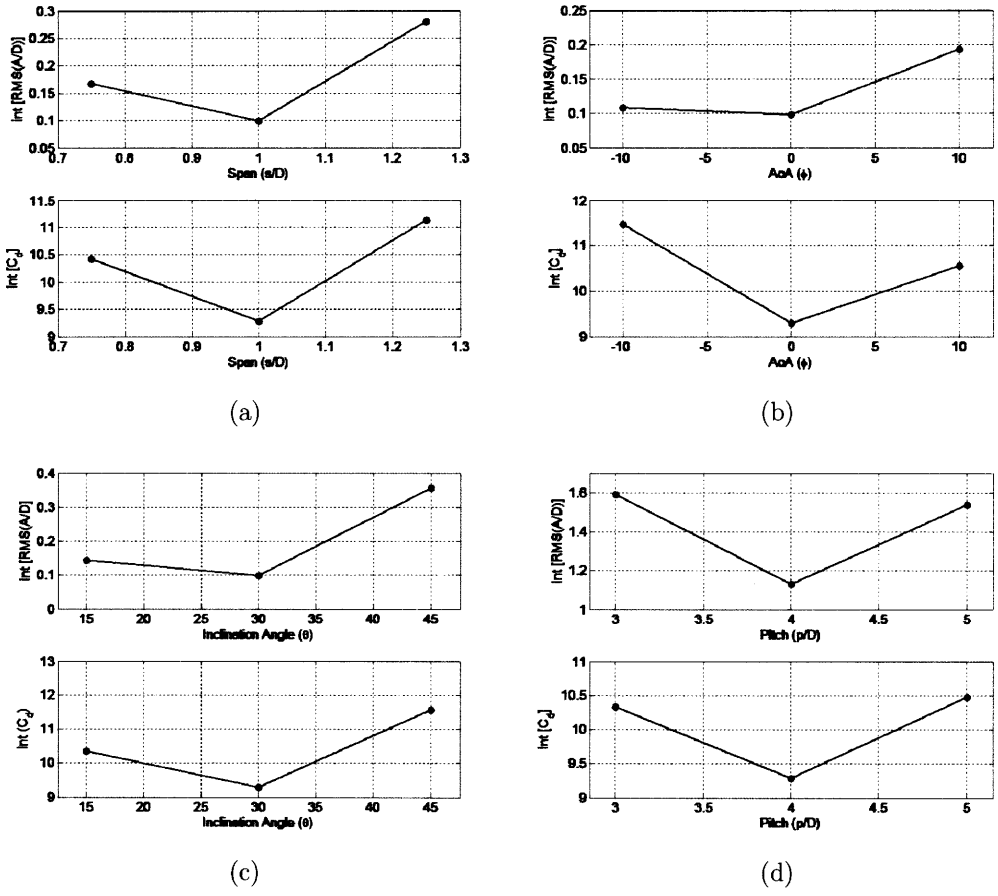

Figure 6-11: Effect on "Rabbit Ear" performance due to change in (a) span, (b) angle of attack, (c) inclination angle and (d) pitch.

Chapter 7

Conclusion

7.1 Assessment of Results

The goal of producing an effective and implementable passive method of vortex induced vibration suppression that meets various criteria is one that is not easily achieved. The ideal method sought after by industry would attain a drag coefficient below 0.6, be cost-effective, easy to implement and be omni-directional without the use of bearings that do not fare well in underwater environments. A number of different approaches were taken in trying to solve this problem. In the end, a few effective means of mitigating VIV and reducing drag were discovered. However, these methods are not necessarily easy to implement in most practical applications.

The suppression method involving hydrofoil vanes performed well in reducing drag and unsteady lift forces on the structure. An extension is made in suggesting that reducing the unsteady lift forces will result in lower amplitude vibrations of the body. Based on flow visualization, vorticity shed from the hydrofoil surfaces interacted with the flow downstream of the cylinder to either delay vortex shedding or eliminate strong alternate shedding altogether. It is hypothesized that this interaction is responsible for the reduction in unsteady lift forces. The best performing configurations served to guide flow around the cylinder and inject additional momentum into the wake. This results in narrowing of the wake and a lower momentum deficit. These are two features that should theoretically reduce drag on the structure. The concerns

with the hydrofoil approach are its unidirectional performance and likely high costs of implementation.

Numerous methods based on the principle of breaking of vortex shedding along the span of a cylinder were explored. The first of these approaches utilized delta wings to generate vortices. The wings were either mounted parallel or at angle to the free stream in order to produce vortices with an axis of rotation inline with the flow. The results confirmed a lower amplitude and even a complete suppression of vibrations in some cases with a corresponding reduction in drag. Smaller delta wings produced a respectable decrease in VIV, but larger wings almost completely suppressed the phenomenon. Drag coefficients for the case in which VIV was eliminated hovered around a value of 1.2, or the expected value for a non-oscillating bare cylinder. This suggests that reductions seen in other delta wing configurations may have been solely the result of reducing the amplitude of oscillations. As a result, a drag coefficient near a value of 1.2 is the lowest to be expected. Again, like the hydrofoils, this systems brings about concerns regarding cost and directionatlity.

The effort to reduce the sensitivity of the suppression mechanism to flow direction was not successful. Reducing the size of vortex generators in order to arrange them in a helical fashion similar to strakes did not provide adequate suppression of VIV. The small size of the tabs used may have resulted in vortices being shed with insufficient strength to interfere with shedding from the cylinder. Increasing the size of the tabs may improve performance, but doing so would result in an assembly approaching the full strake design. Extensive testing of this approach was not conducted for this reason and a new approach was investigated.

The final approach undertaken sought to reproduce the performance of the delta wings while reducing the complexity of the system. The "Rabbit Ear" method essentially used delta wings cut in half and adhered to the cylinder at a prescribed inclination angle. This modification to the delta wing configuration eliminates the need to have a support component to attach the wing above the cylinder surface. "Rabbit Ears" did provide similar performance as one of the smaller delta wings tested. The method is not quite as directionally sensitive as the delta wings since the

attached surface that could become perpendicular to the flow has been reduced. This approach has some merit, but does not meet all the criteria that we wish to satisfy.

Some of the methods developed may be suitable for certain applications, but do not meet all the needs for offshore application. Further research is certainly required to find VIV suppression technique with better characteristics than those investigated in this thesis. An improved understanding of the effects of the techniques explored has been gained. This knowledge can be used to guide future work on this topic.

Bibliography

[1] Bearman, P.W. Vortex Shedding from Oscillating Bluff Bodies. Annual Review of Fluid Mechanics, 16: 195–222, 1984.

[2] Bearman, P.W. and J.C. Owen. Passive Control of VIV With Drag Reduction. European Journal of Mechanics and Fluids, 23: 9–15, 2001.

[3] Brankovic, M. and P.W. Bearman. Measurements of Transverse Forces on Circular Cylinders Undergoing Vortex-Induced Vibration. Journal of Fluids and Structures, 22: 829–836, 2006.

[4] Carberry, J. and J. Sheridan. Forces and Wake Modes of an Oscillating Cylinder. Journal of Fluids and Structures, 15: 523–532, 2001.

[5] Dahl, J.M. Vortex-Induced Vibration of a Circular Cylinder with Combined In-line and Cross-Flow Motion. PhD Thesis, Massachusetts Institute of Technology, 2008.

[6] Farrell, D.E. Vortex Induced Vibrations of Cylinder: Experiments in Reducing Drag. SM Thesis, Massachusetts Institute of Technology, 2007.

[7] Grimminger, G. The Effect of Rigid Guide Vanes on the Vibration and Drag of a Towed Circular Cylinder. David Taylor Model Basin, Washington, Rep. 504, 1945.

[8] Huang, X.Y. Suppression of Vortex Shedding from a Circular Cylinder by Internal Acoustic Excitation. Journal of Fluids and Structures, 9: 563–570, 1995.

[9] Huang, X.Y. Passive Control of the aerodynamic Forces Acting on a Circular Cylinder. Experimental Thermal and Fluid Sciences, 16: 112–121, 1998.

[10] Igarashi, T. Flow Characteristics Around a Circular Cylinder With a Slit. Bulletin of the Japan Society of Mechanical Engineers, 21: 656–664, 1978.

[11] Hwang, J. and K. Yang. Drag Reduction on a Circular Cylinder Using Dual Detached Splitter Plates. Journal of Wind Engineering and Industrial Aerodynamics, 95: 551–564, 2007.

[12] King, R. A Review of Vortex Shedding Research and its Application. Journal of Ocean Engineering, 4: 141–171, 1977.

[13] Lee, Sang-Joon and Jung-Yeop Lee. Flow Structure Behind a Rotationally Oscillating Circular Cylinder. Journal of Fluids and Structures, 2: 1097–1112, 2006.

[14] Lee Sang-Joon, Lee Sang-Ik and Park, C. Reducing the Drag on a Circular Cylinder by Upstream Installation of a Small Control Rod. Fluid Dynamics Research, 34: 233–250, 2004.

[15] Lee, E.J. Airfoil Vortex Induced Vibration Suppression Devices. SM Thesis, Massachusetts Institute of Technology, 2007.

[16] Lesage, F. and L.S. Garthshore. A Method of Reducing Drag and Fluctuating Side Force on Bluff Bodies. Journal of Wind Engineering and Industrial Aerodynamics, 25: 229–245, 1987.

[17] Niemann, H.J. and Holscher, N. A Review of Recent Experiments on the Flow Past Circular Cylinders. Journal of Wind Engineering and Industrial Aerodynamics, 33: 197–209, 1990.

[18] Owen, J.C. and Masa Brankovic. Experimental Studies of Passive Control of Vortex-Induced Vibration. Journal of Fluids and Structures, 15: 597–605, 2003.

[19] Roshko, A. On the Drag and Shedding Frequency of Two-Dimensional Bluff Bodies. National Advisory Committe for Aeronautic, Note 3168, 1954.

[20] Sarpkaya, T. A Critical Review of the Intrinsic Nature of Vortex-Induced Vibrations. Journal of Fluids and Structures, 19: 389–447, 2004.

[21] Sarpkaya, T. Transverse Oscillations of a Cylinder in Uniform Flow. Technical Report NPS-69SL77071, Naval Postgraduate School, Mechanical Engineering, Monterey, California, July 1977.

[22] Willert, C.E. and M. Gharib. Digital Particle Image Velocimetry. Experiments in Fluids, 10: 181–193, 1991.

[23] Williams, J.E. and B.C. Zhao. The Active Control of Vortex Shedding. Journal of Fluids and Structures, 3: 115–122, 1989.

[24] Williamson C.H.K. and R. Govardhan. Vortex-Induced Vibrations. Annual Review of Fluid Mechanics, 36: 413–455, 2004.

[25] Williamson, C.H.K. Vortex Dynamics in the Cylinder Wake. Annual Review of Fluid Mechanics, 28: 477–539, 1996.

[26] Williamson, C.H.K. Vortex Dynamics in the Cylinder Wake. Annual Review of Fluid Mechanics, 28: 477–539, 1996.

[27] Yajima, Y. and O. Sano. A Note on the Drag Reduction of a Circular Cylinder Due to Double Rows of Holes. Fluid Dynamics Research, 18: 237–243, 1996.

[28] Zdravkovich, M.M. *Flow Around Circular Cylinders.* Oxford University Press, New York, 1997.

[29] Zdravkovich, M.M. Review and Classification of Various Aerodynamic and Hydrodynamic Means for Suppressing Vortex Shedding. Journal of Wind Engineering and Industrial Aerodynamics, 7: 145–189, 1981.

Appendix A

Vorticity Fields for Hydrofoil Vane Modifications

A total of fifty-six different configurations of the outlined parameters were investigated using a triangular fairing, single and dual hydrofoil pairs. Alterations in all possible parameters were made. The naming protocol for these configurations was chosen with the following prefixes

- *BC* : Bare cylinder with a diameter (D) of 3.81cm.
- *BCT* : *BC* modified with a triangular fairing of extension length D.
- *BCP* : *BCT* with a pair of hydrofoils (chord of 3.18cm).
- *BCPTn*: *BC* with a pair of hydrofoils (chord of 3.18cm).
- *BCQ* : *BC* with two pairs of hydrofoils - larger pair (chord of 3.18cm) and smaller pair (chord of 2.41cm) of hydrofoils.

Three major configuration parameters were defined for the cylinder and hydrofoil system. First, the attachment location of the hydrofoil can be located anywhere along the circumference of the cylinder. This parameter was defined as the swivel angle where a value of zero degrees places the attachment points directly above the poles of the cylinder. Positive swivel angle denotes that the attachment point was rotated

closer to the downstream stagnation point. Second, the height of the hydrofoils was defined as the distance of the hydrofoil attachment point from the cylinder surface. Finally, the third parameter was the angle of attack of the hydrofoils relative to the free stream flow.

The adjustable parameters are height (H), swivel angle (S) and angle of attack (A). The naming convention incorporates these letters followed by a number indicating the set value for that parameter. A denotation of H1, H3 and H4 indicates heights of $\frac{1}{6}$, $\frac{1}{3}$ and $\frac{5}{12}$, respectively. The number proceeding S and A indicate the angle set for that parameter. The *BCQ* configurations are similarly denoted with the addition of a preceeding S or L to parameter indicators to indicate whether the parameter value refers to the small or large hydrofoil pair, respectively.

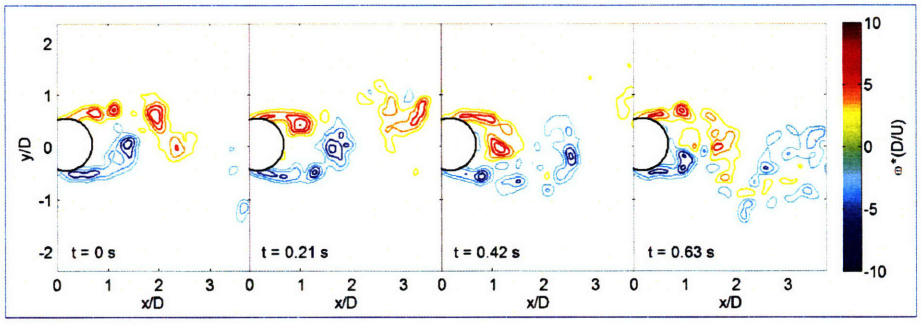

(a)

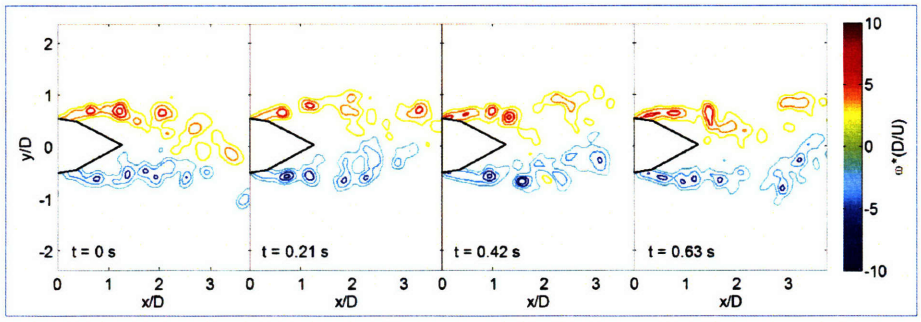

(b)

Figure A-1: Time spaced vorticity fields for the (a) BC and (b) BCT configurations.

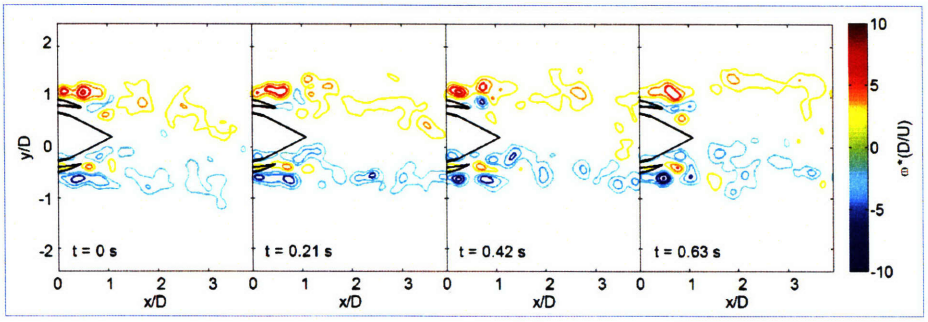

(a)

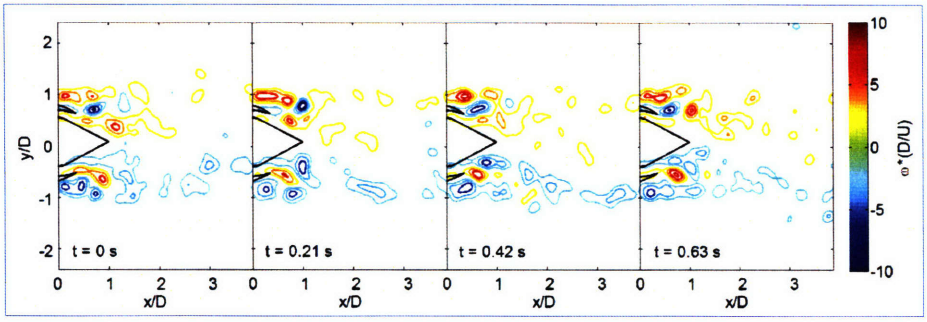

(b)

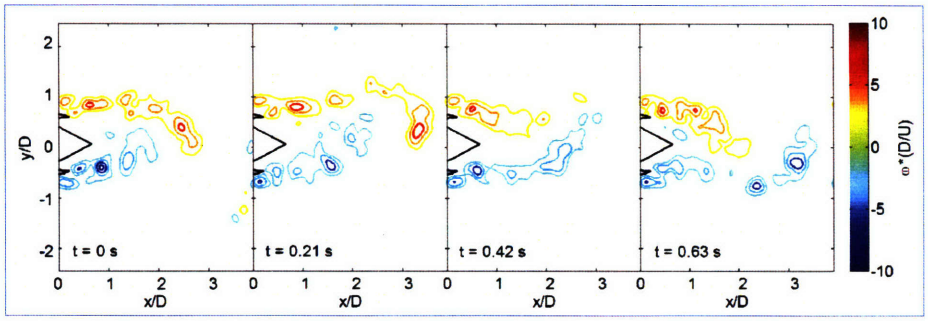

(c)

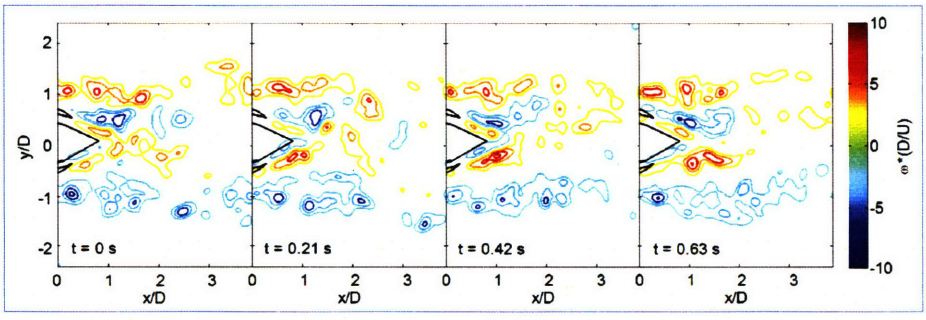

(d)

Figure A-2: Time spaced vorticity fields for the (a) BCP_H1_S0_A0, (b) BCP_H1_S0_A10, (c) BCP_H1_S0_A-10 and (d) BCP_H1_S0_A20 configurations.

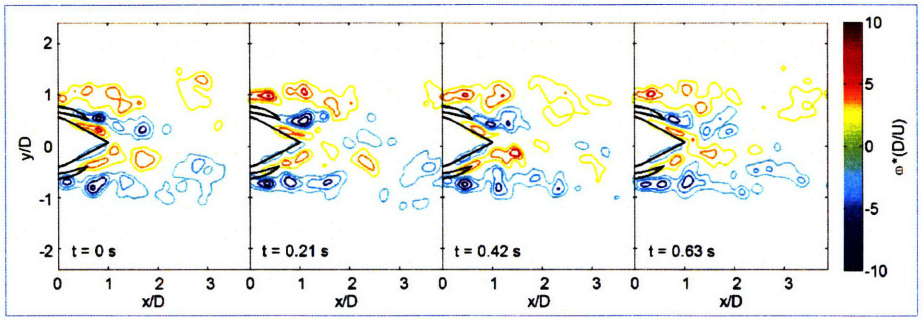

(a)

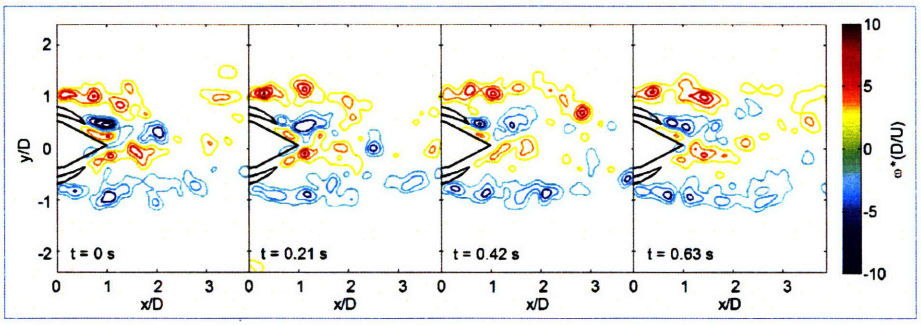

(b)

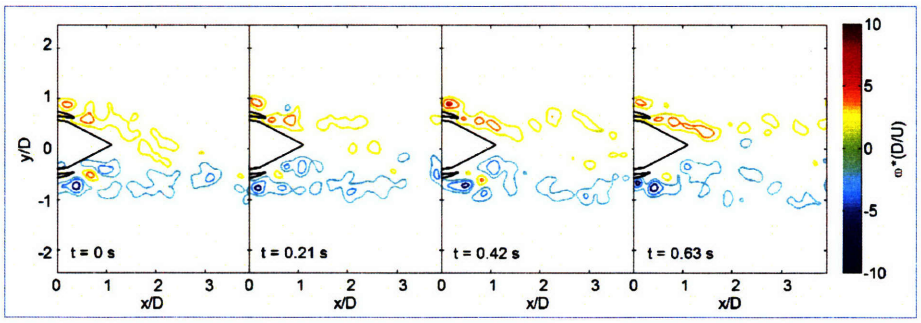

(c)

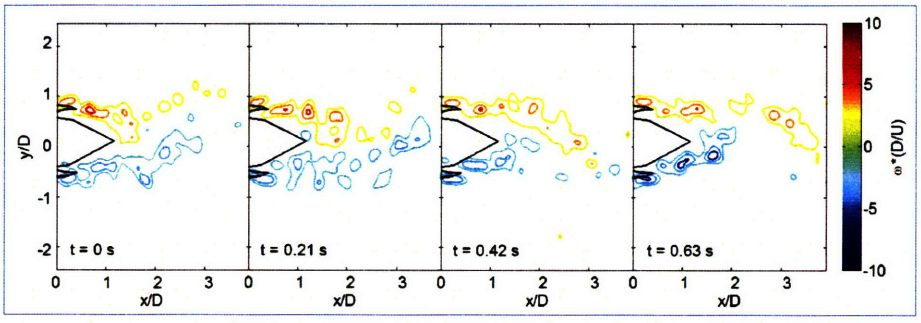

(d)

Figure A-3: Time spaced vorticity fields for the (a) BCP_H1_S20_A10, (b) BCP_H1_S20_A20, (c) BCP_H1_S20n_A0 and (d) BCP_H1_S20n_A-10 configurations.

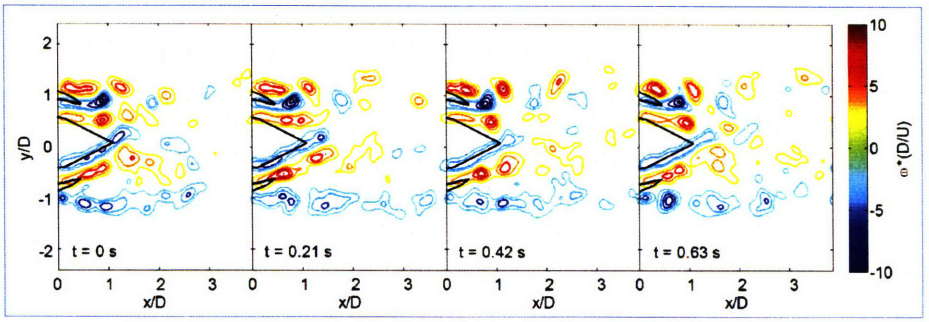

(a)

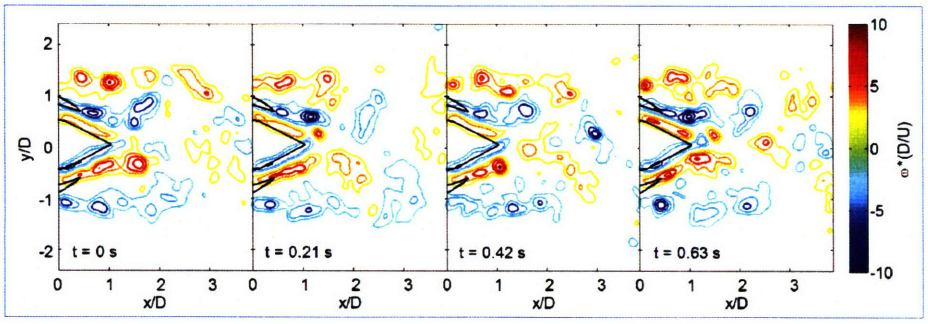

(b)

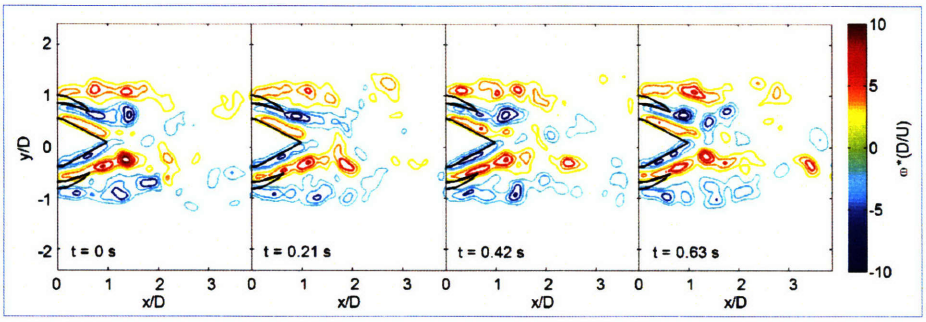

(c)

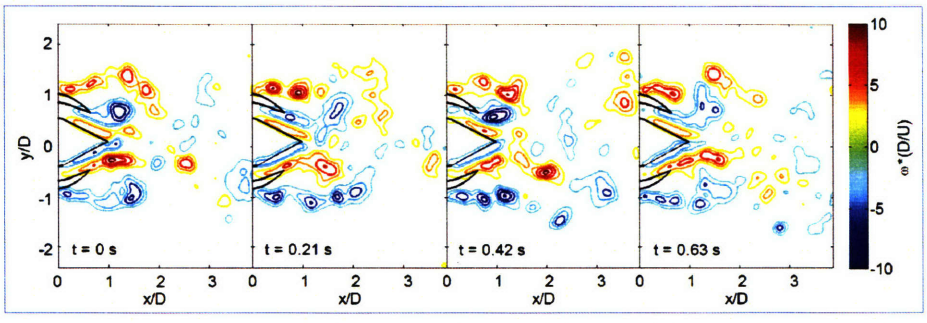

(d)

Figure A-4: Time spaced vorticity fields for the (a) BCP_H3_S0_A10, (b) BCP_H3_S0_A20, (c) BCP_H3_S20_A10 and (d) BCP_H3_S20_A20 configurations.

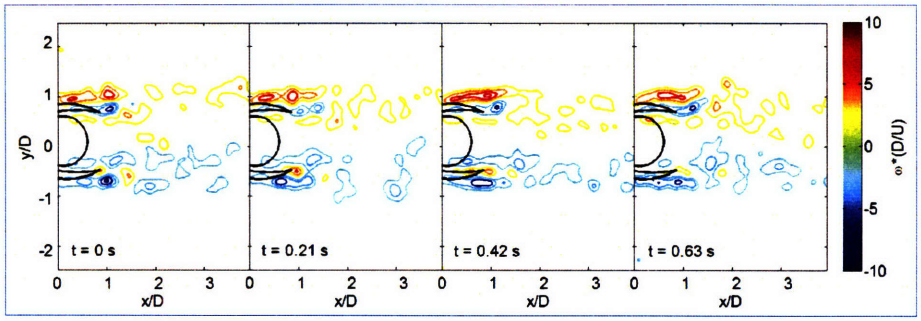

(a)

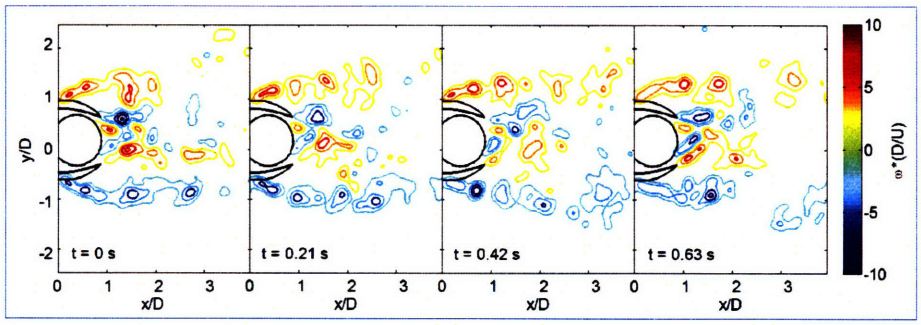

(b)

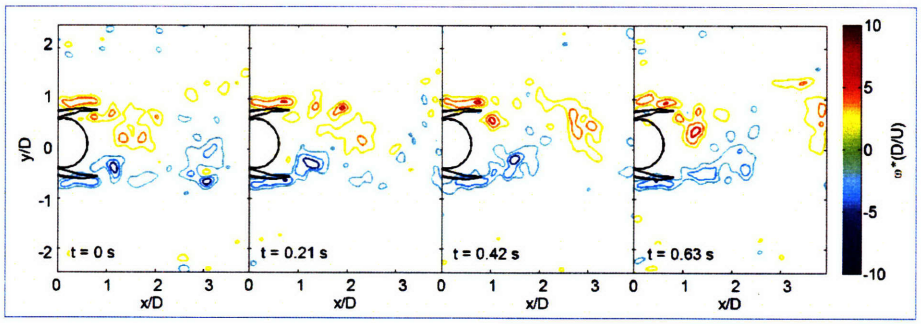

(c)

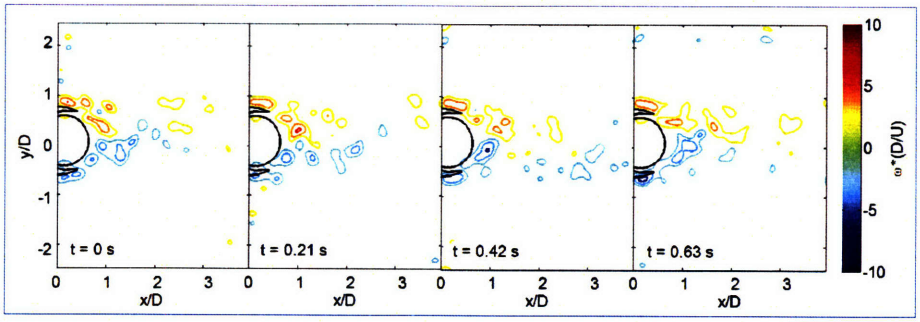

(d)

Figure A-5: Time spaced vorticity fields for the (a) BCPTn_H1_S0_A0, (b) BCPTn_H1_S0_A10, (c) BCPTn_H1_S0_A-10 and (d) BCPTn_H1_S-20_A0 configurations.

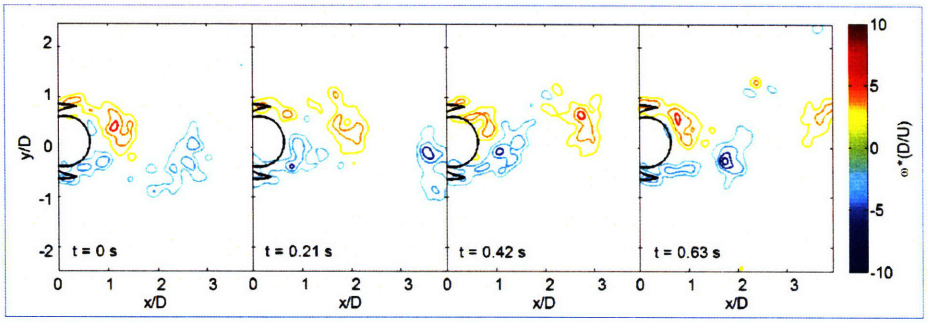

(a)

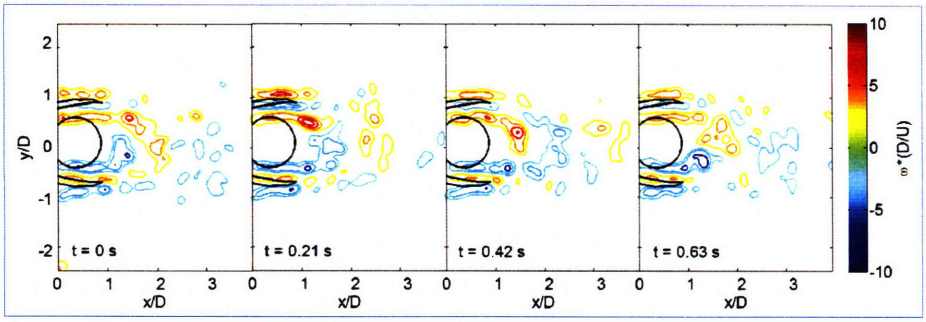

(b)

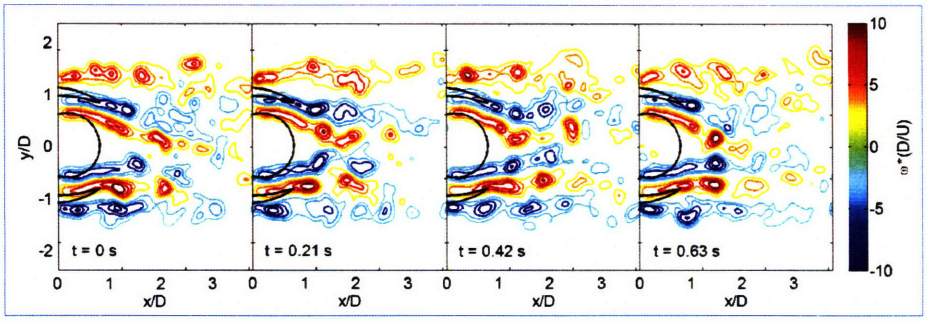

(c)

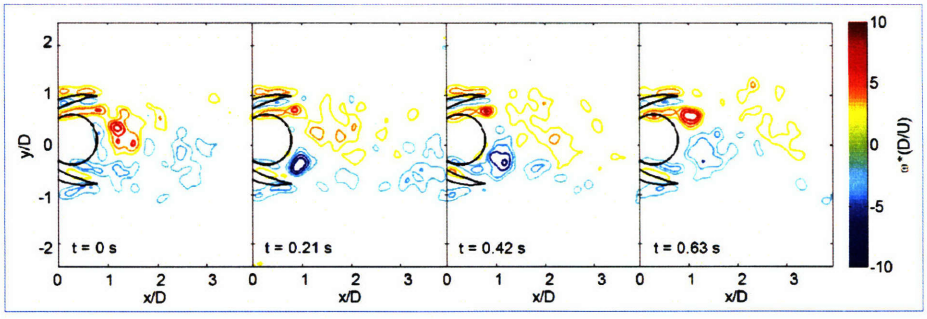

(d)

Figure A-6: Time spaced vorticity fields for the (a) BCPTn_H1_S-20_A-10, (b) BCPTn_H3_S0_A0, (c) BCPTn_H3_S0_A10 and (d) BCPTn_H3_S0_A-10 configurations.

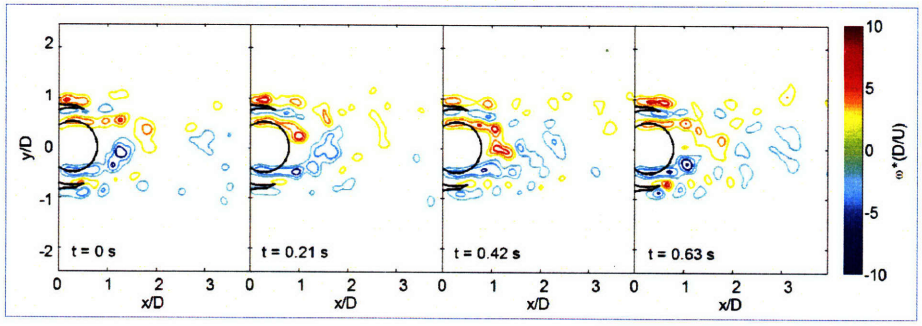

(a)

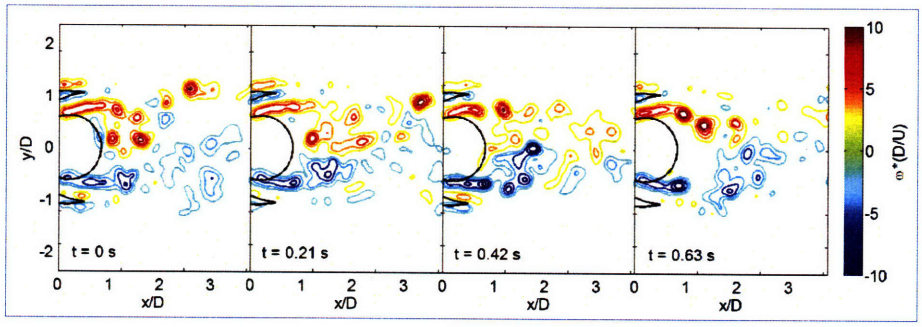

(b)

Figure A-7: Time spaced vorticity fields for the (a) BCPTn_H3_S-20_A0 and (b) BCPTn_H3_S-20_A-10 configurations.

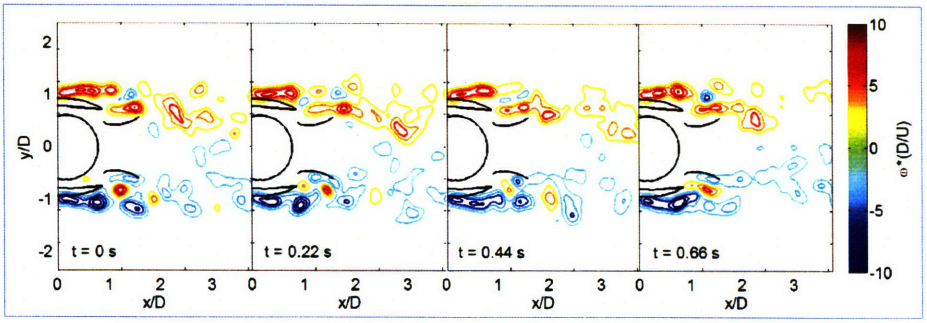

(a)

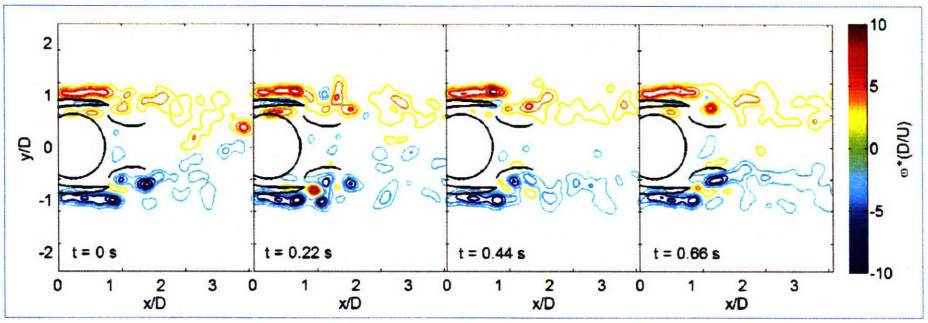

(b)

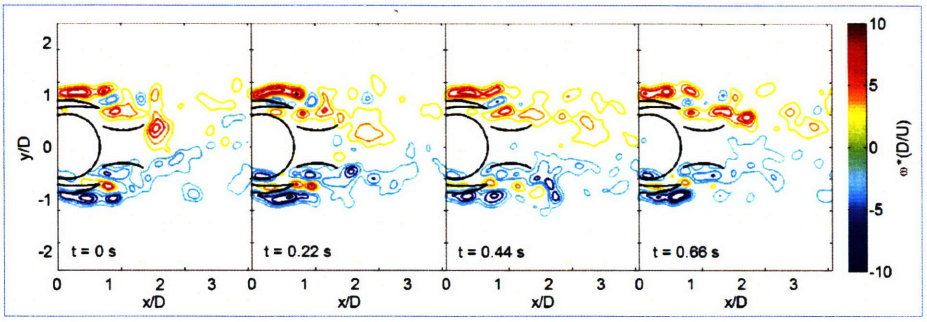

(c)

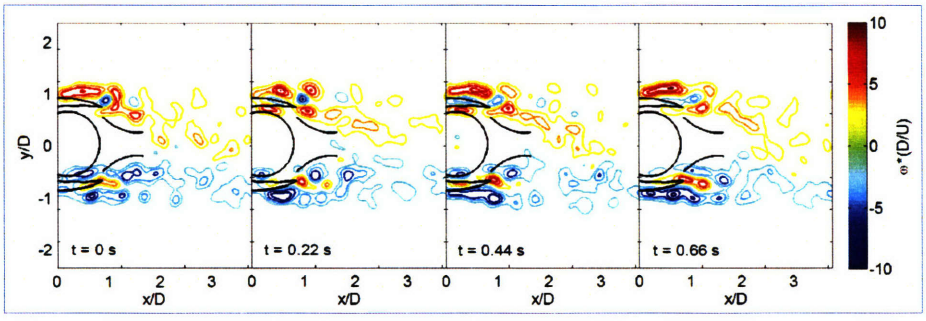

(d)

Figure A-8: Time spaced vorticity fields for the (a) BCQ_LH1_LS0_LA0_SH3_SS60_SA0, (b) BCQ_LH1_LS0_LA0_SH3_SS60_SA-20, (c) BCQ_LH1_LS0_LA0_SH3_SS70_SA0 and (d) BCQ_LH1_LS0_LA0_SH3_SS70_SA-20 configurations.

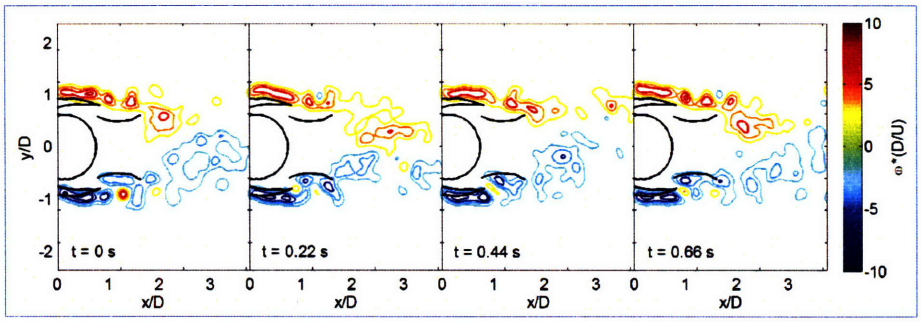

(a)

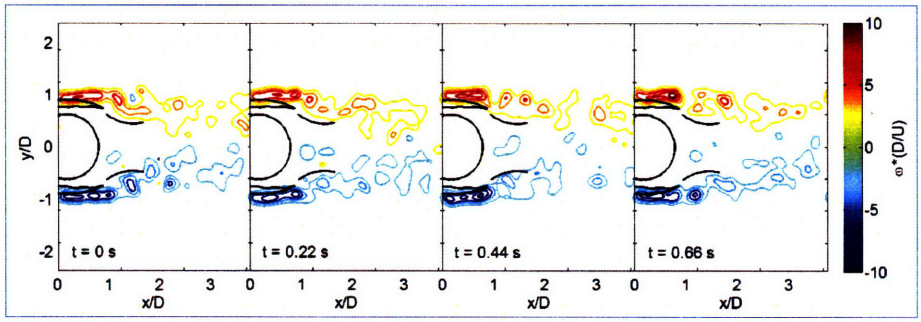

(b)

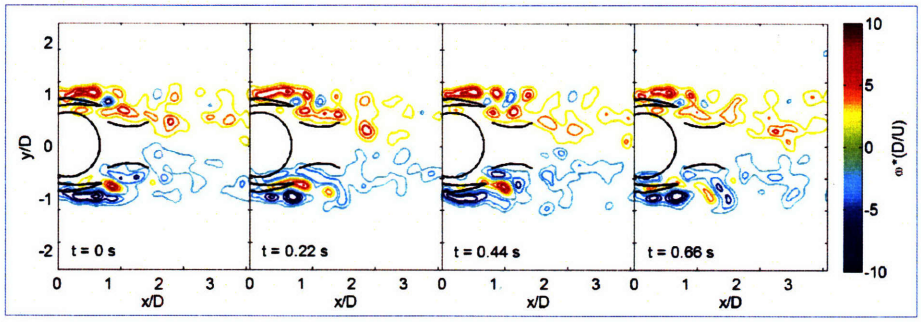

(c)

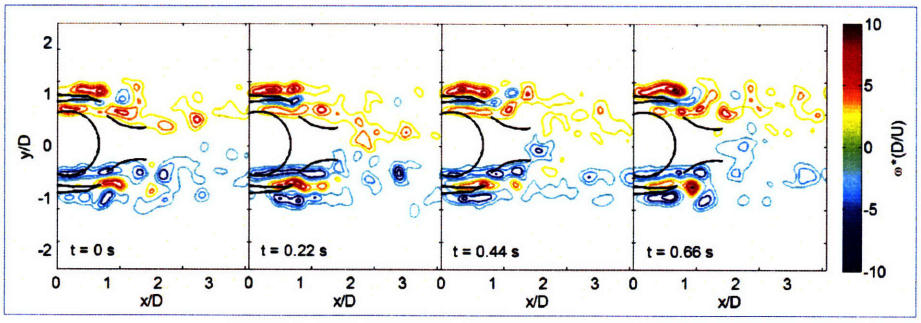

(d)

Figure A-9: Time spaced vorticity fields for the (a) BCQ_LH1_LS0_LA0_SH4_SS60_SA0, (b) BCQ_LH1_LS0_LA0_SH4_SS60_SA-20, (c) BCQ_LH1_LS0_LA0_SH4_SS70_SA0 and (d) BCQ_LH1_LS0_LA0_SH4_SS70_SA-20 configurations.

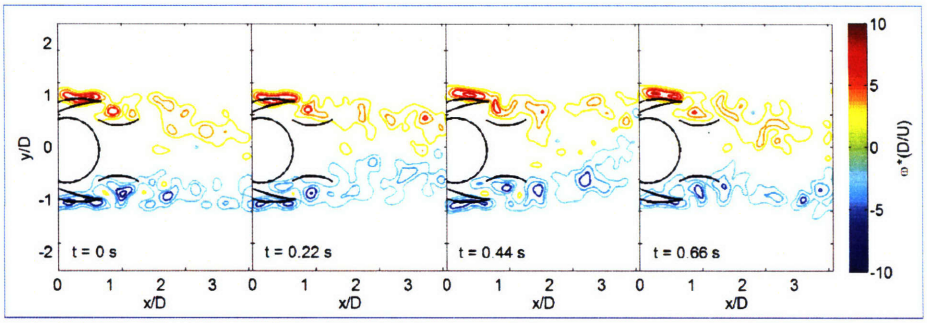

(a)

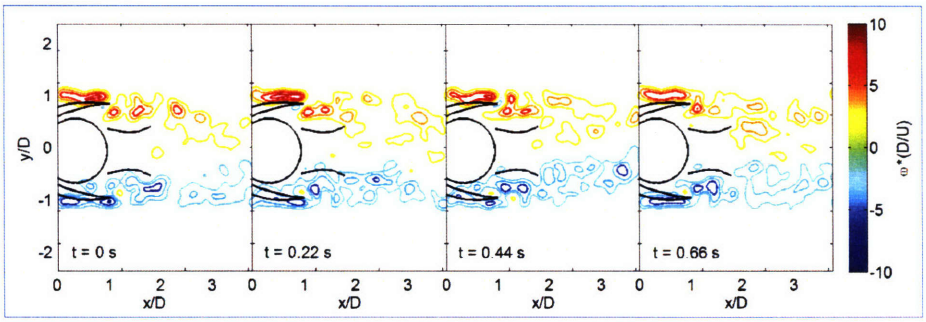

(b)

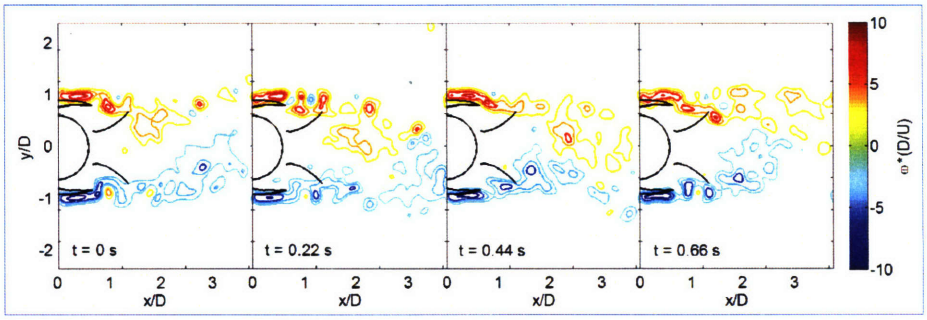

(c)

Figure A-10: Time spaced vorticity fields for the (a) BCQ_LH1_LS0_LA-10_SH3_SS60_SA0, (b) BCQ_LH1_LS0_LA-10_SH3_SS70_SA0 and (c) BCQ_LH1_LS0_LA-10_SH3_SS70_SA-20 configurations.

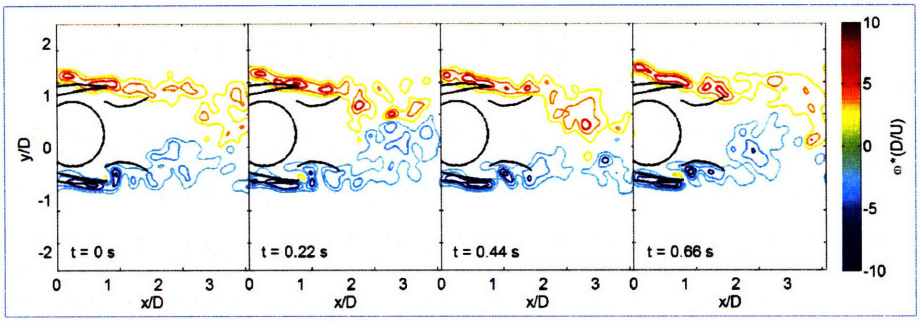

(a)

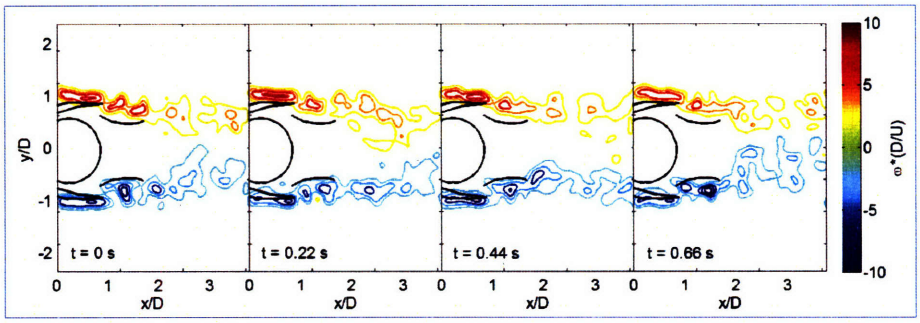

(b)

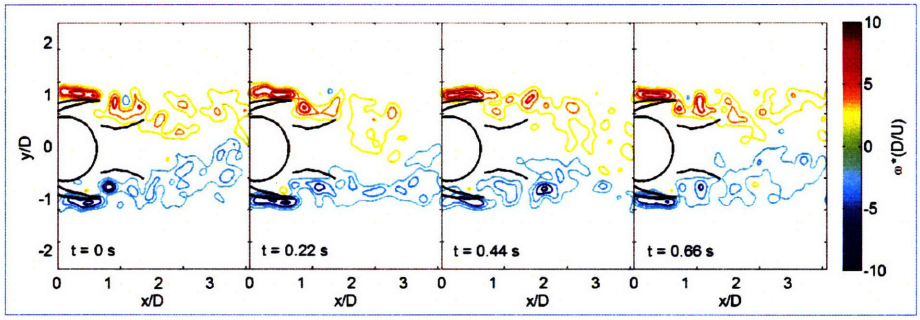

(c)

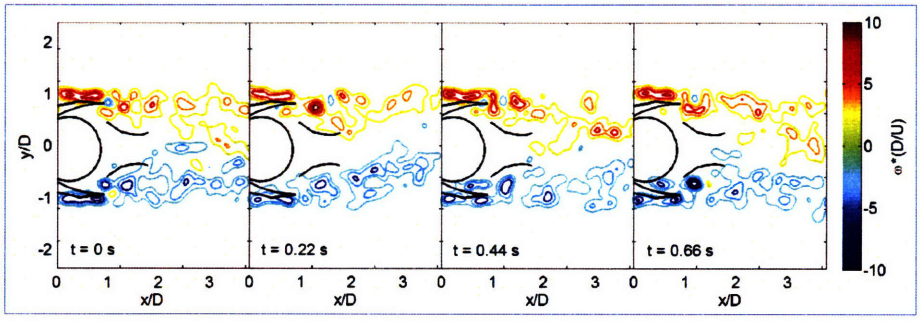

(d)

Figure A-11: Time spaced vorticity fields for the (a) BCQ_LH1_LS0_LA-10_SH4_SS60_SA0, (b) BCQ_LH1_LS0_LA-10_SH4_SS60_SA-20, (c) BCQ_LH1_LS0_LA-10_SH4_SS70_SA0 and (d) BCQ_LH1_LS0_LA-10_SH4_SS70_SA-20 configurations.

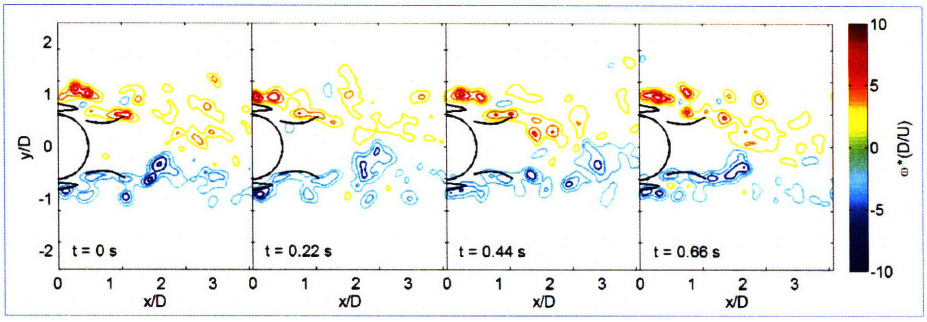

(a)

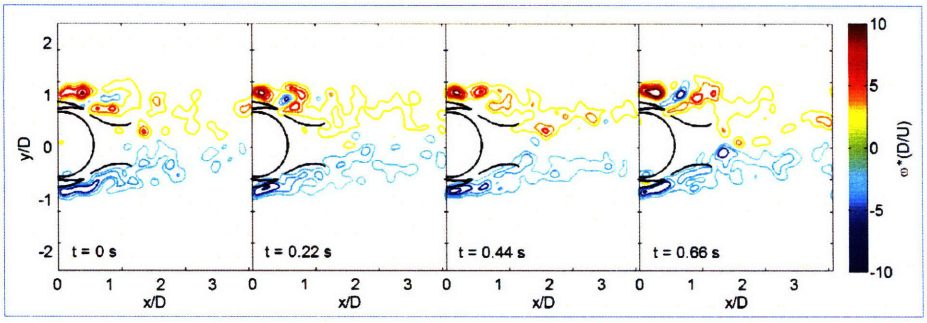

(b)

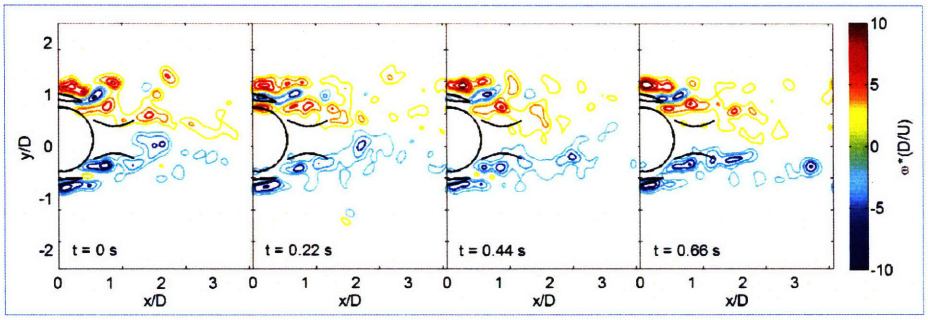

(c)

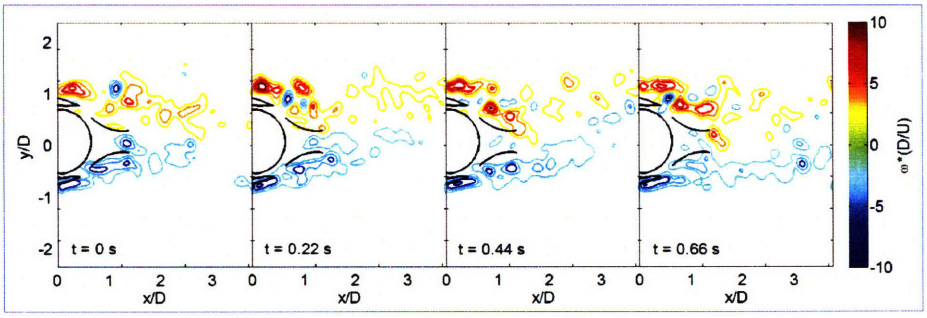

(d)

Figure A-12: Time spaced vorticity fields for the (a) BCQ_LH1_LS-20_LA0_SH3_SS60_SA0, (b) BCQ_LH1_LS-20_LA0_SH3_SS60_SA-20, (c) BCQ_LH1_LS-20_LA0_SH3_SS70_SA0 and (d) BCQ_LH1_LS-20_LA0_SH3_SS70_SA-20 configurations.

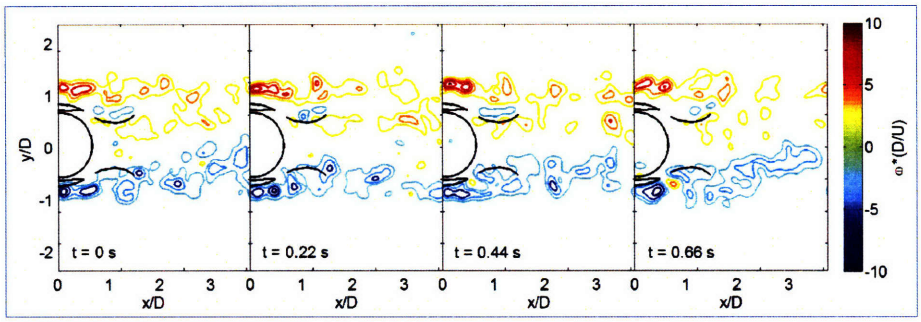

(a)

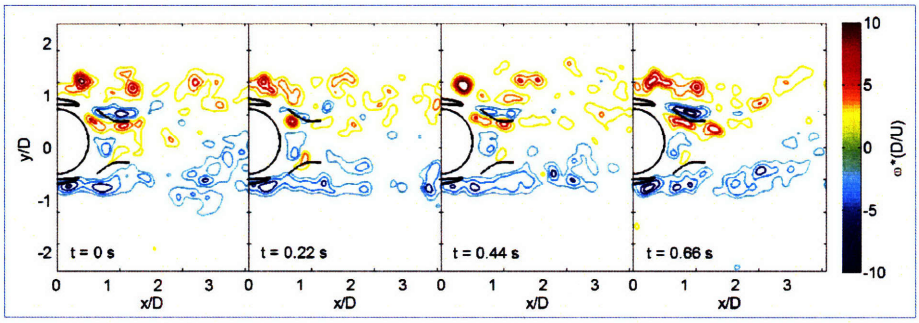

(b)

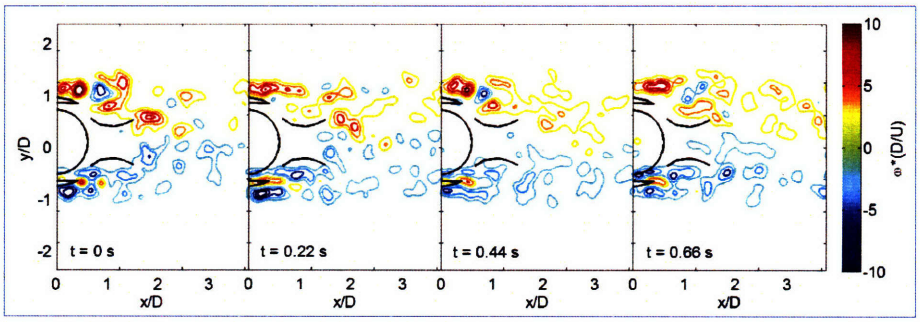

(c)

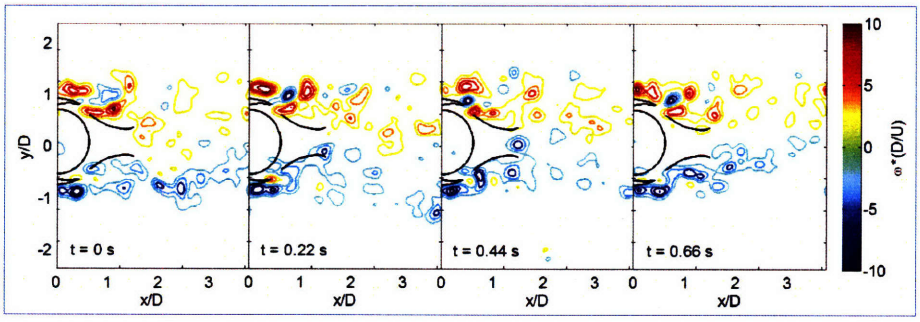

(d)

Figure A-13: Time spaced vorticity fields for the (a) BCQ_LH1_LS-20_LA0_SH4_SS60_SA0, (b) BCQ_LH1_LS-20_LA0_SH4_SS60_SA-20, (c) BCQ_LH1_LS-20_LA0_SH4_SS70_SA0 and (d) BCQ_LH1_LS-20_LA0_SH4_SS70_SA-20 configurations.

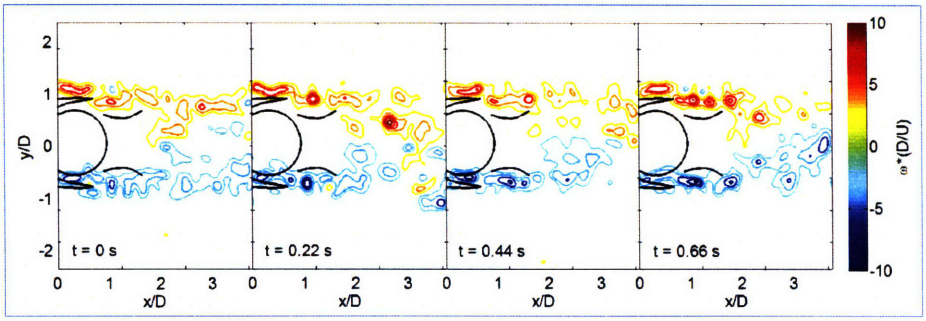

(a)

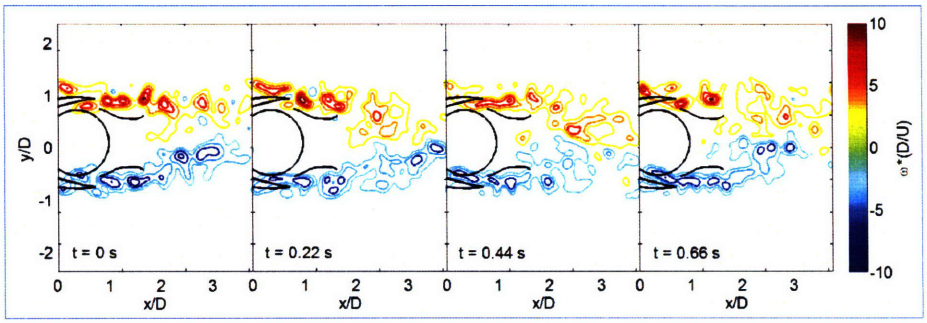

(b)

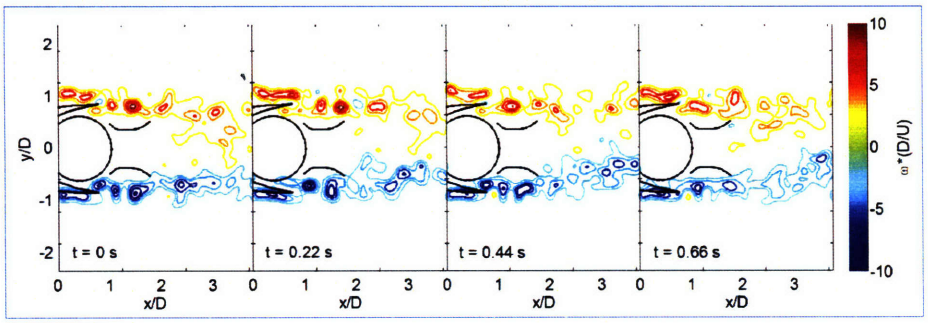

(c)

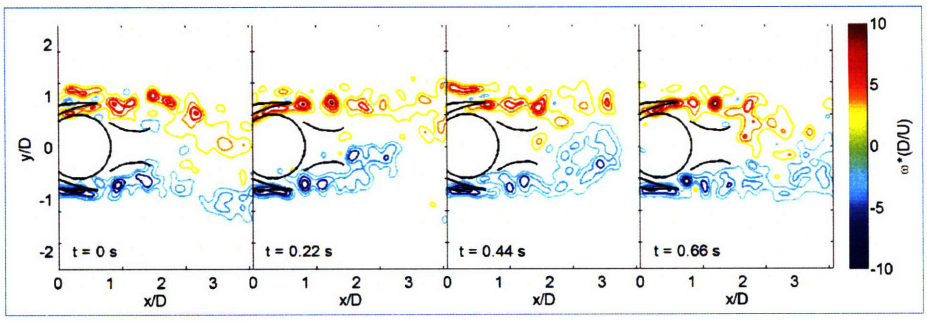

(d)

Figure A-14: Time spaced vorticity fields for the (a) BCQ_LH1_LS-20_LA-10_SH3_SS60_SA0, (b) BCQ_LH1_LS-20_LA-10_SH3_SS60_SA-20, (c) BCQ_LH1_LS-20_LA-10_SH3_SS70_SA0 and (d) BCQ_LH1_LS-20_LA-10_SH3_SS70_SA-20 configurations.

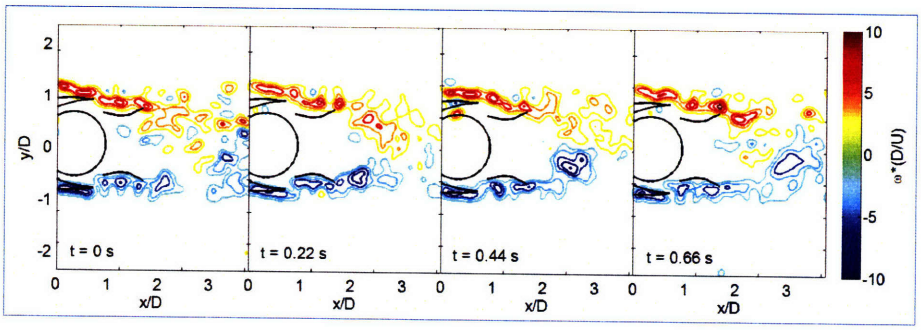

(a)

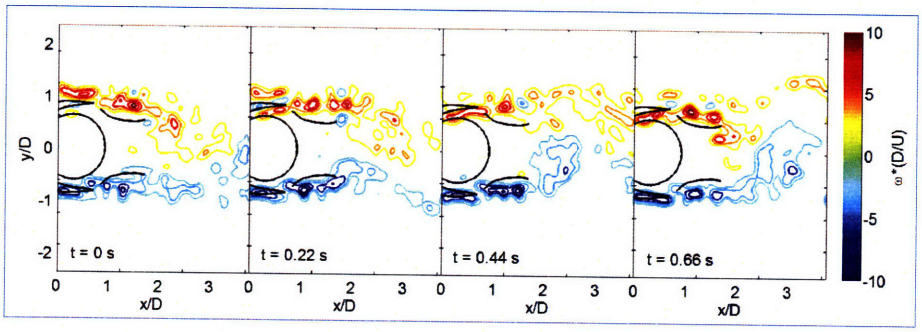

(b)

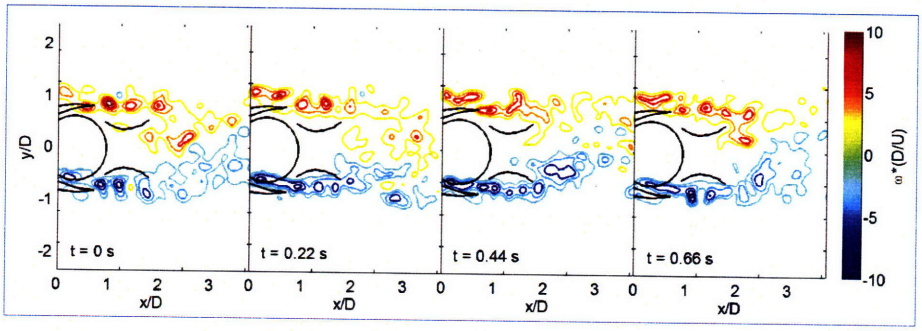

(c)

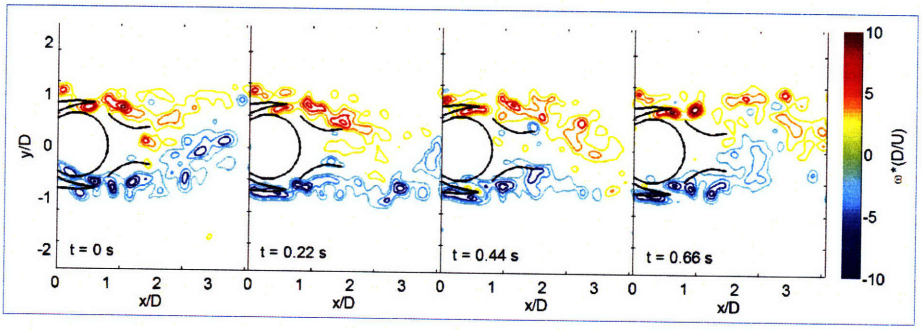

(d)

Figure A-15: Time spaced vorticity fields for the (a) BCQ_LH1_LS-20_LA-10_SH4_SS60_SA0, (b) BCQ_LH1_LS-20_LA-10_SH4_SS60_SA-20, (c) BCQ_LH1_LS-20_LA-10_SH4_SS70_SA0 and (d) BCQ_LH1_LS-20_LA-10_SH4_SS70_SA-20 configurations.

Appendix B

Power Spectral Density of Lift Force Results for Hydrofoil Vane Modifications

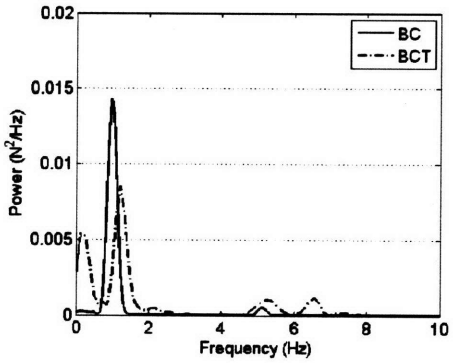

(a)

Figure B-1: Power spectral density of lift forces for *BCT* hydrofoil configurations.

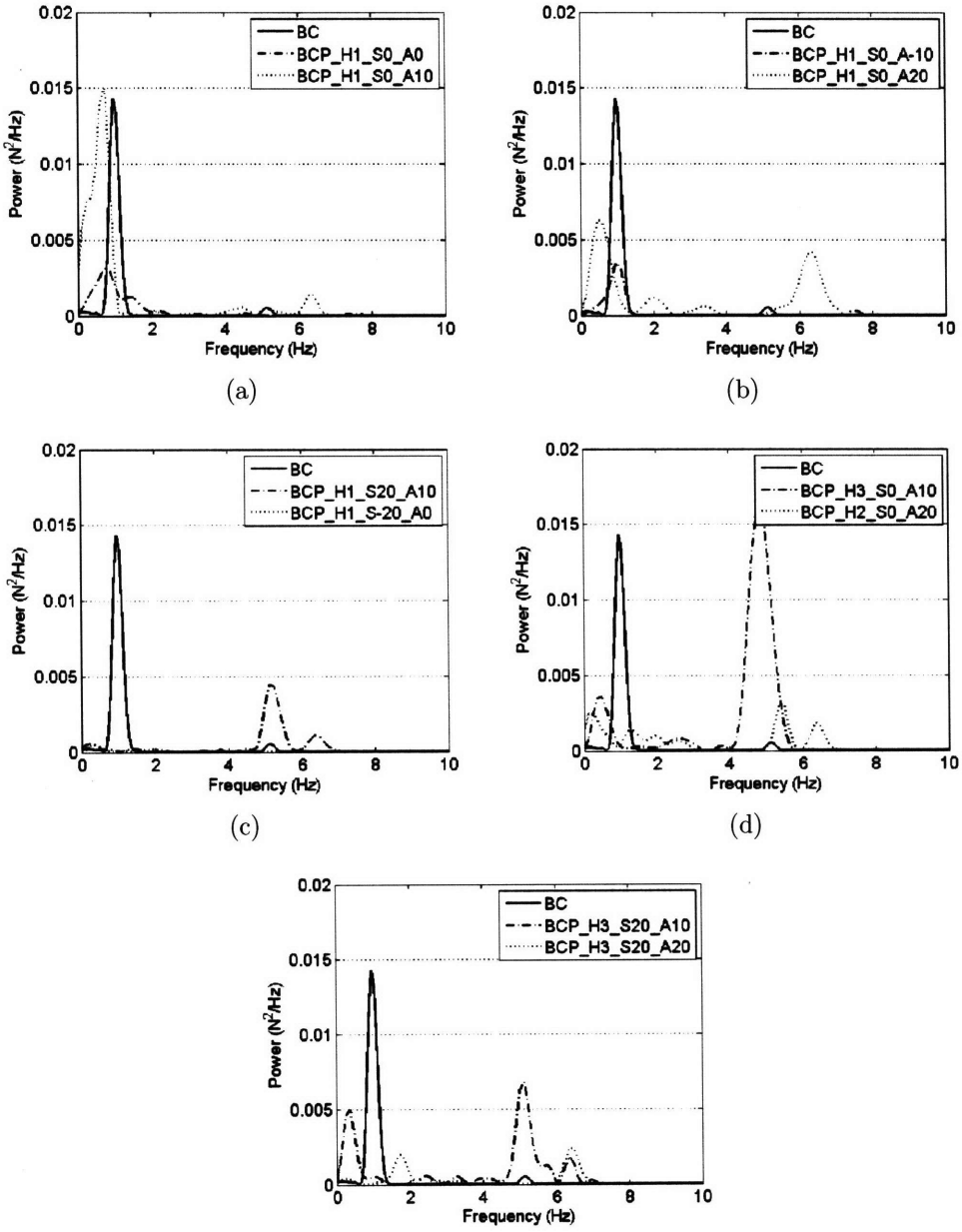

Figure B-2: Power spectral density of lift forces for *BCP* hydrofoil configurations.

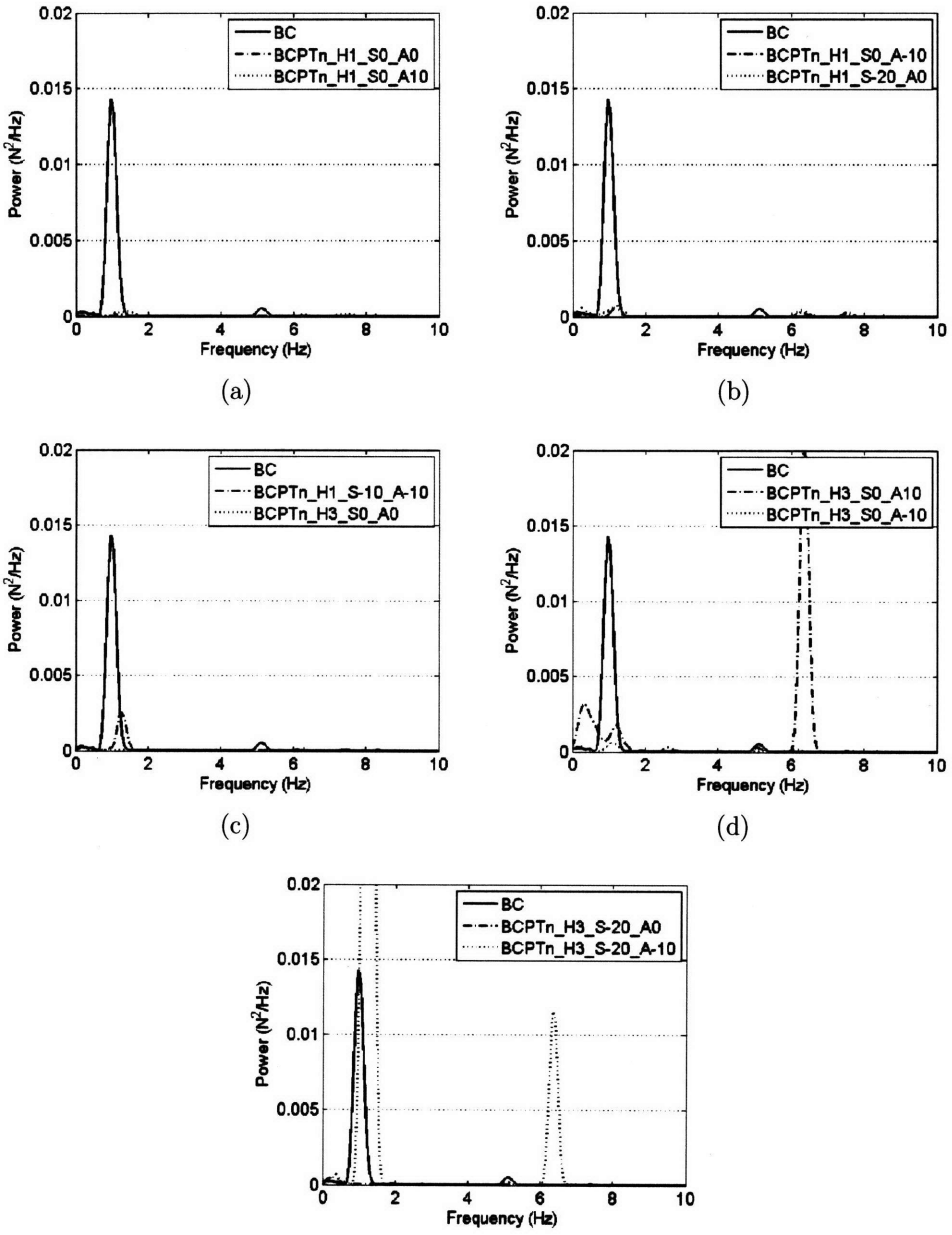

Figure B-3: Power spectral density of lift forces for $BCPTn$ hydrofoil configurations.

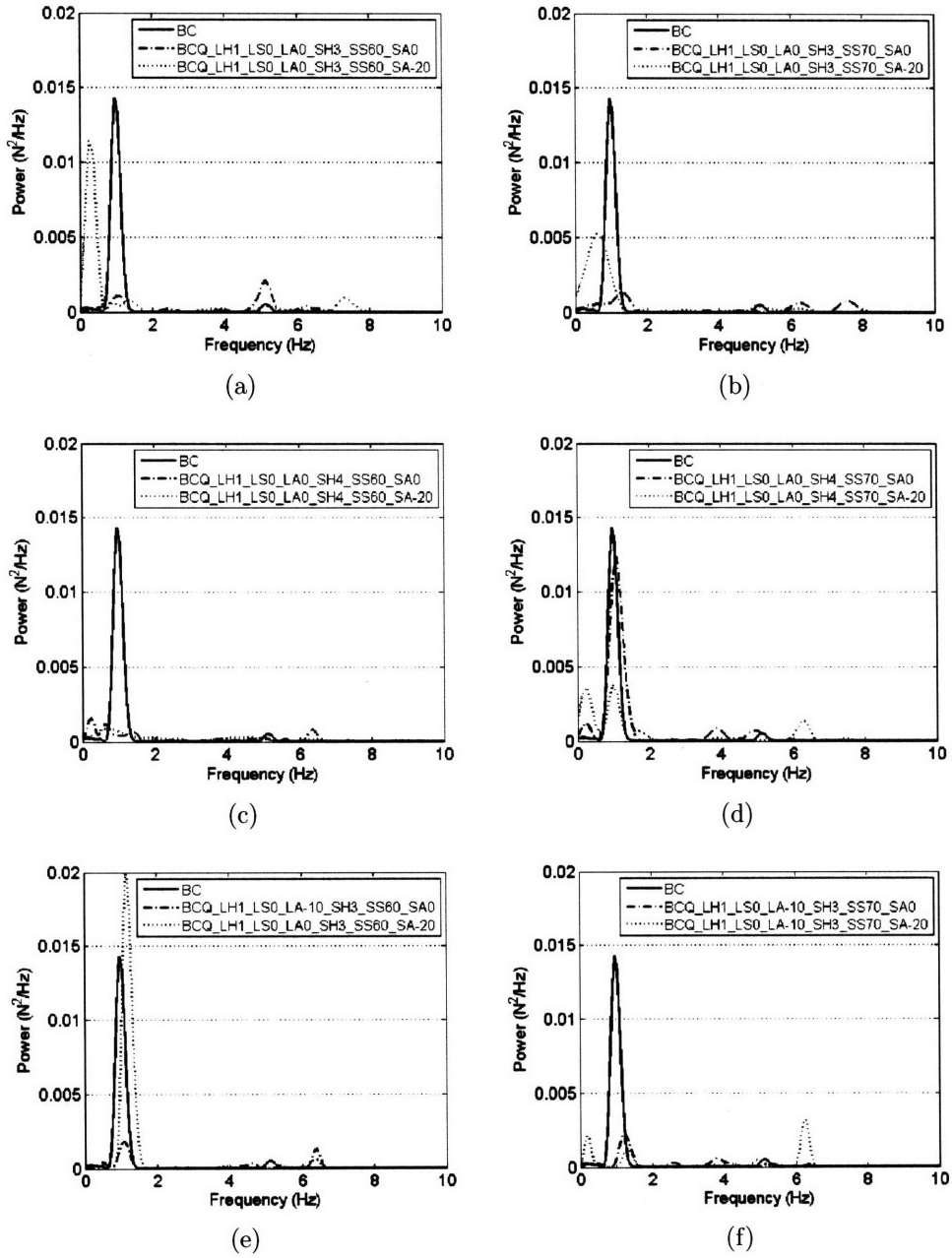

Figure B-4: Power spectral density of lift forces for *BCQ* hydrofoil configurations.

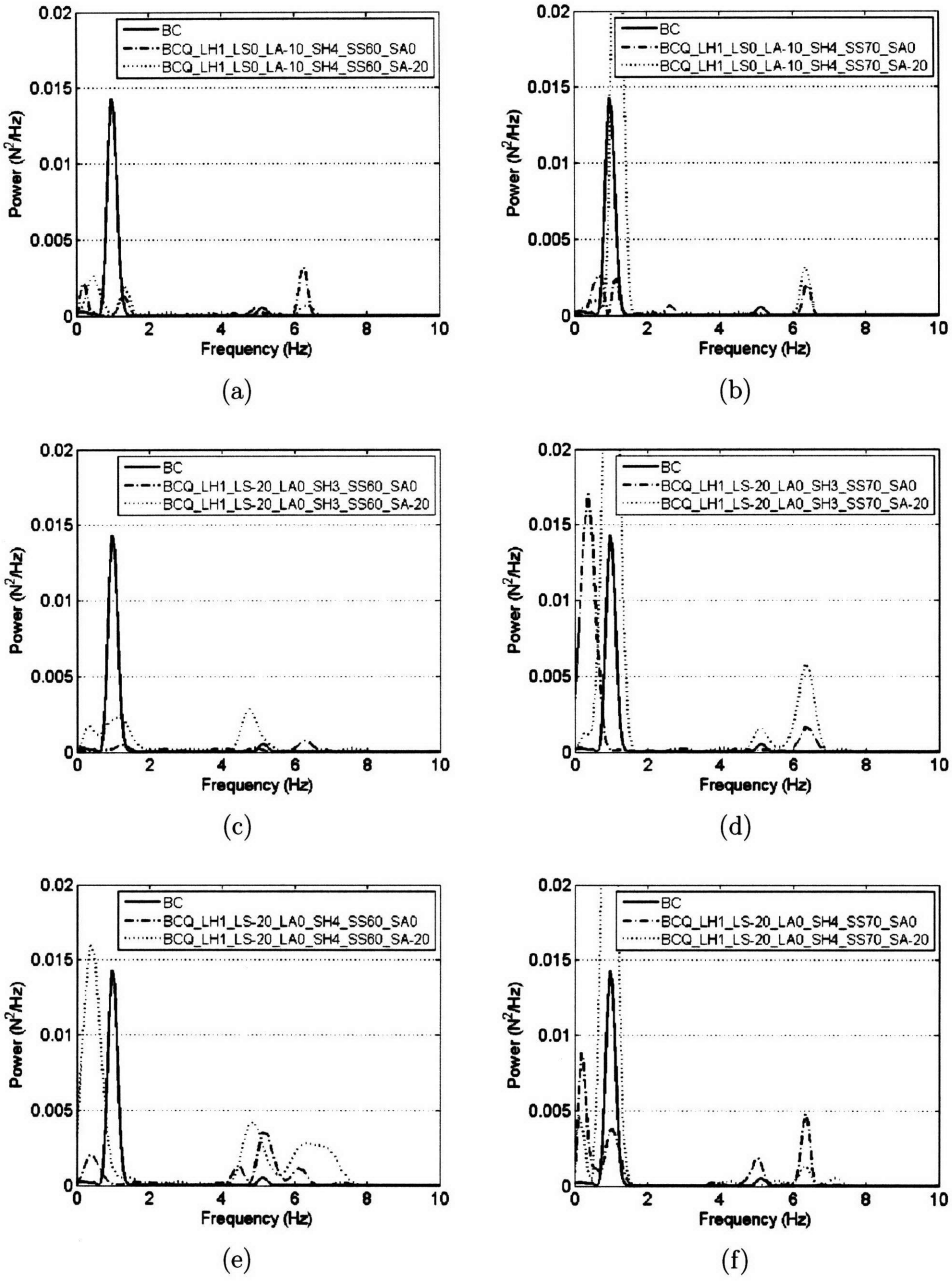

Figure B-5: Power spectral density of lift forces for *BCQ* hydrofoil configurations.

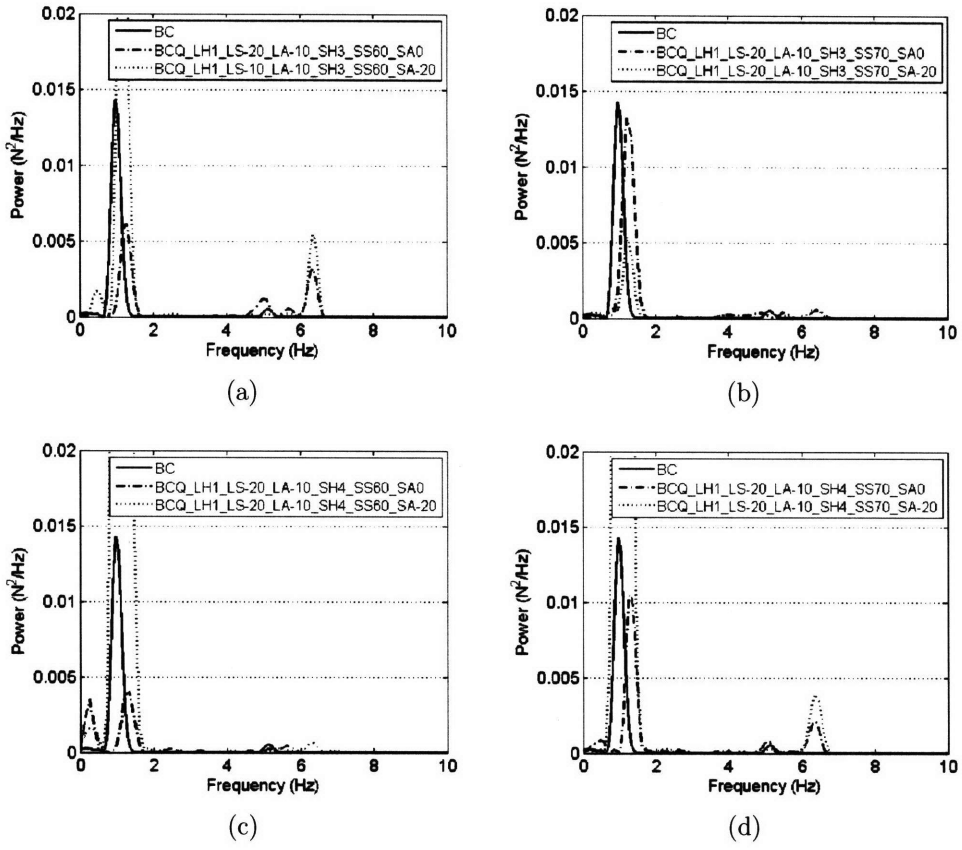

Figure B-6: Power spectral density of lift forces for *BCQ* hydrofoil configurations.

Appendix C

Selected Towing Tank Plucktest Results

The results of these sample plucktests depict the consistency of the system across the time period in which tests were conducted using the oscillating rig in the MIT Towing Tank.

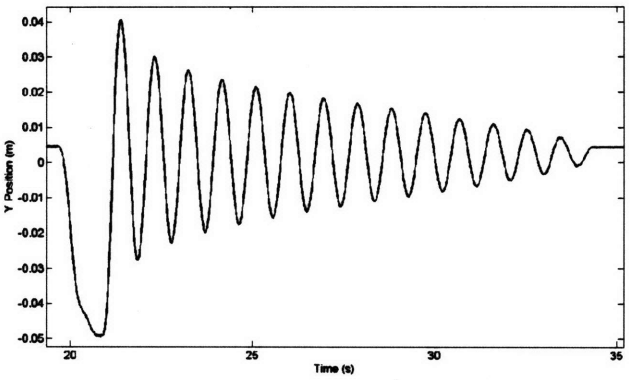

(a)

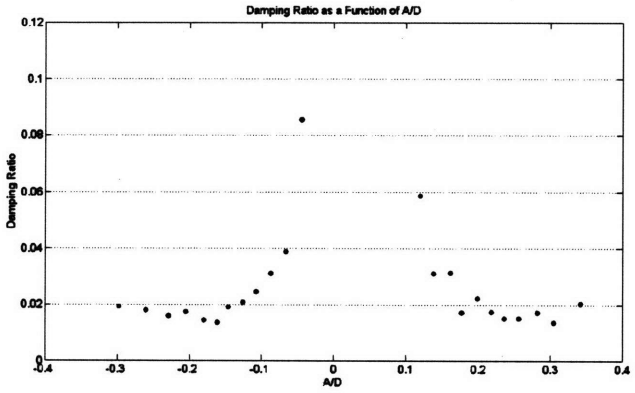

(b)

Figure C-1: Sample of the position signal recording from a pluck test and the calculated damping ratio as a function of A/D.

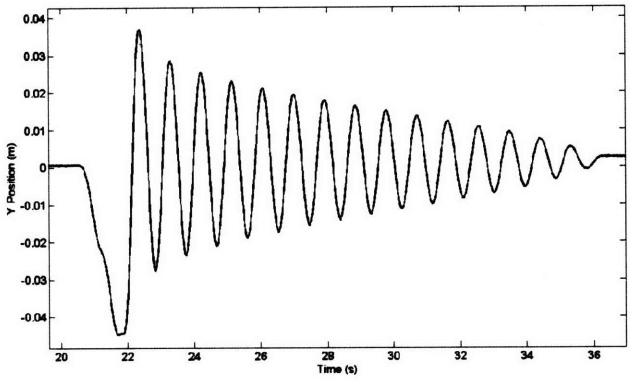

(a)

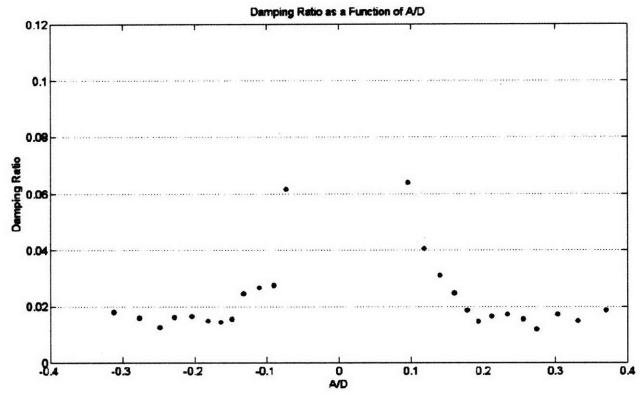

(b)

Figure C-2: Sample of the position signal recording from a pluck test and the calculated damping ratio as a function of A/D.

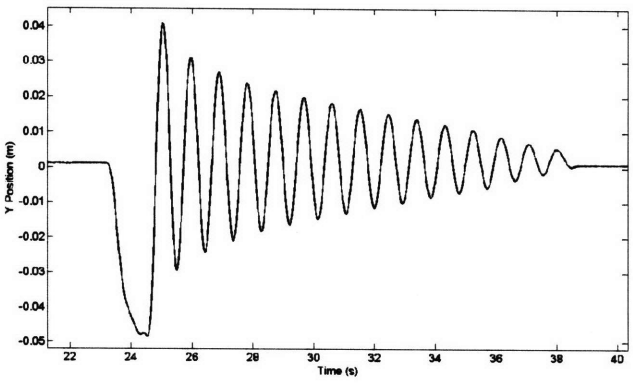

(a)

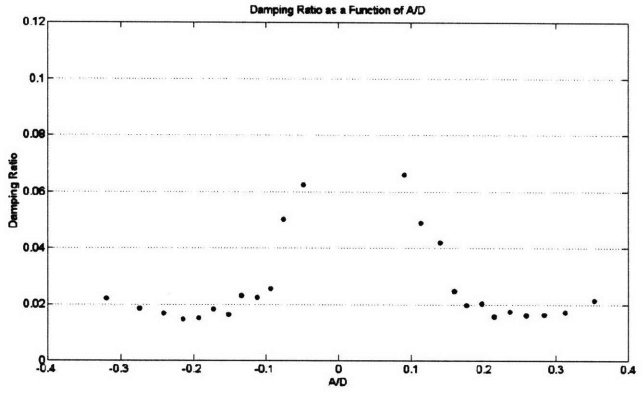

(b)

Figure C-3: Sample of the position signal recording from a pluck test and the calculated damping ratio as a function of A/D.

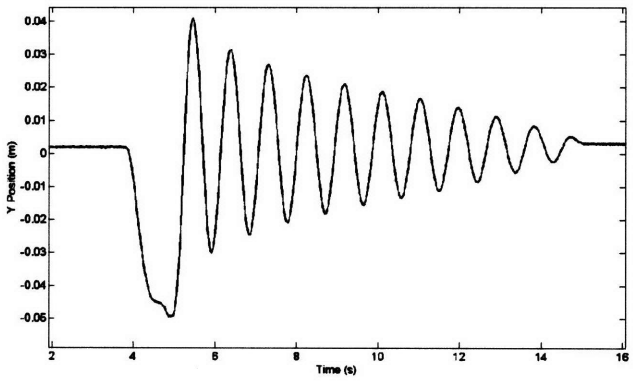

(a)

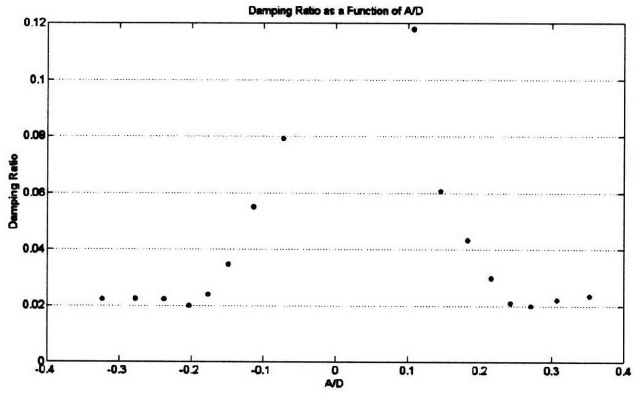

(b)

Figure C-4: Sample of the position signal recording from a pluck test and the calculated damping ratio as a function of A/D.

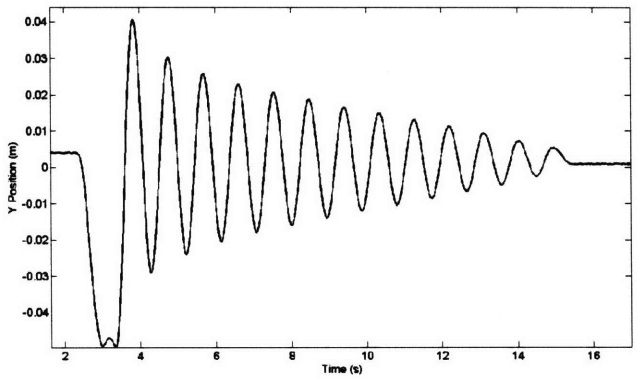

(a)

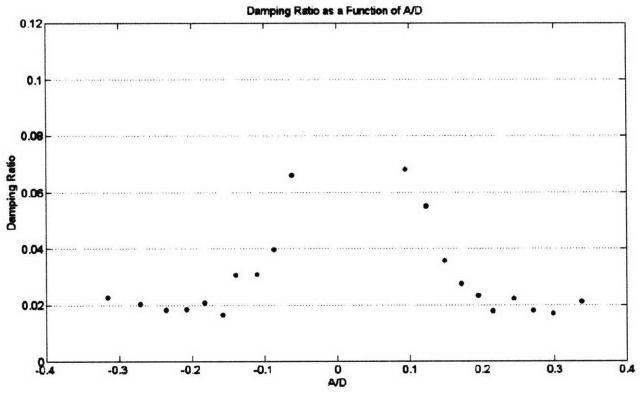

(b)

Figure C-5: Sample of the position signal recording from a pluck test and the calculated damping ratio as a function of A/D.

Appendix D

Time Traces for Delta Wing Modified Cylinder

The transverse position over time for tests of a cylinder modified with the delta wings described in Chapter 4. The result for a bare cylinder is also provided for comparison purposes.

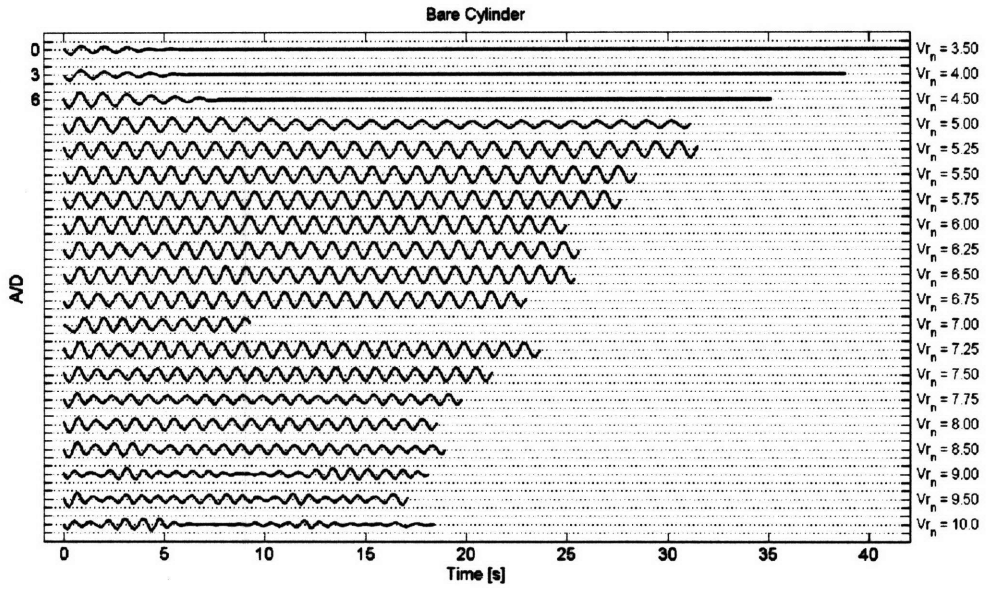

Figure D-1: Time traces of the oscillatory behavior exhibited by a bare cylinder.

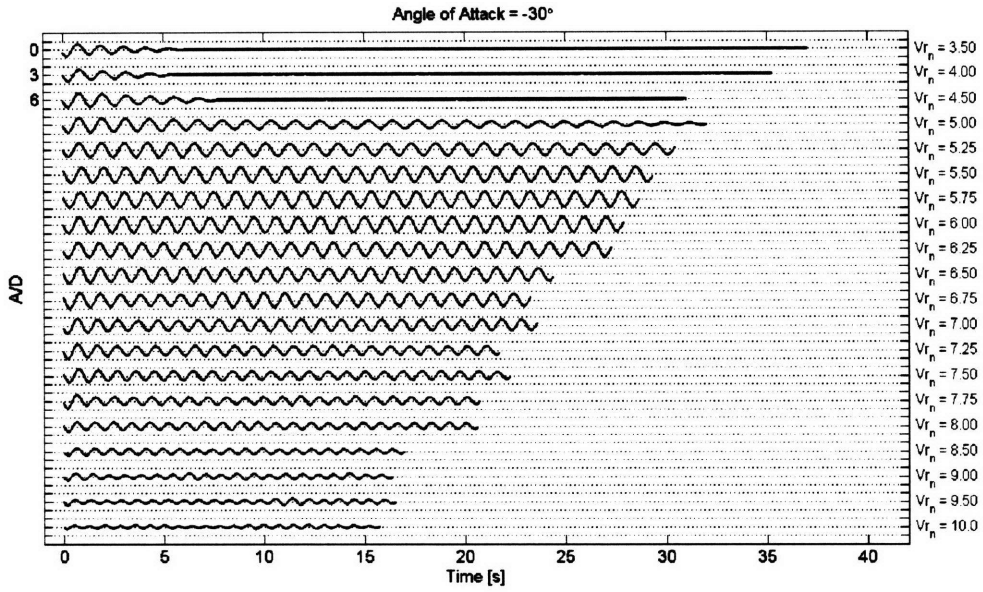

(a)

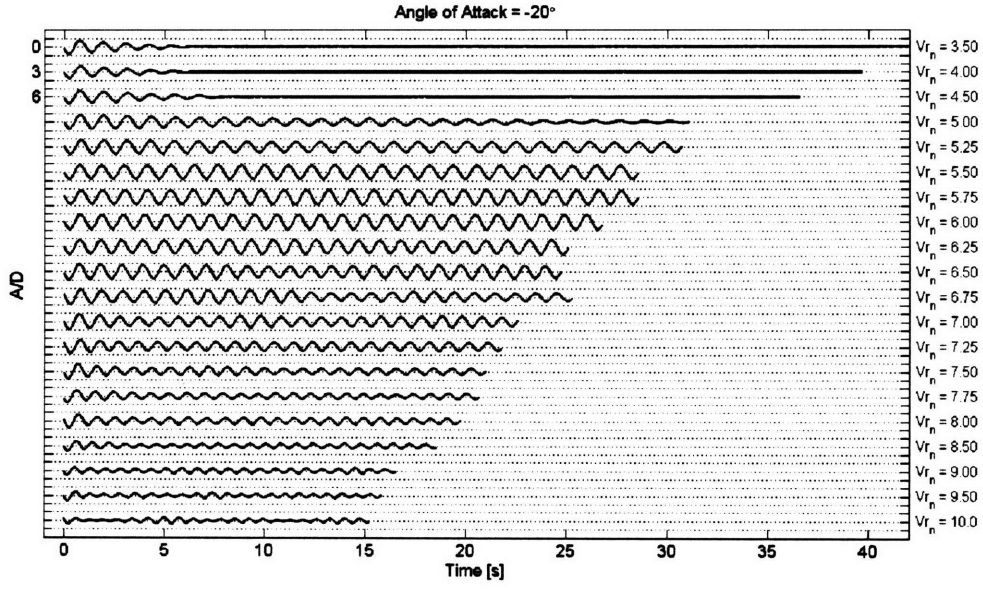

(b)

Figure D-2: Time traces of the oscillatory behavior exhibited by a cylinder modified with equilateral delta wings and angle of attack of (a) $-30°$ and (b) $-20°$.

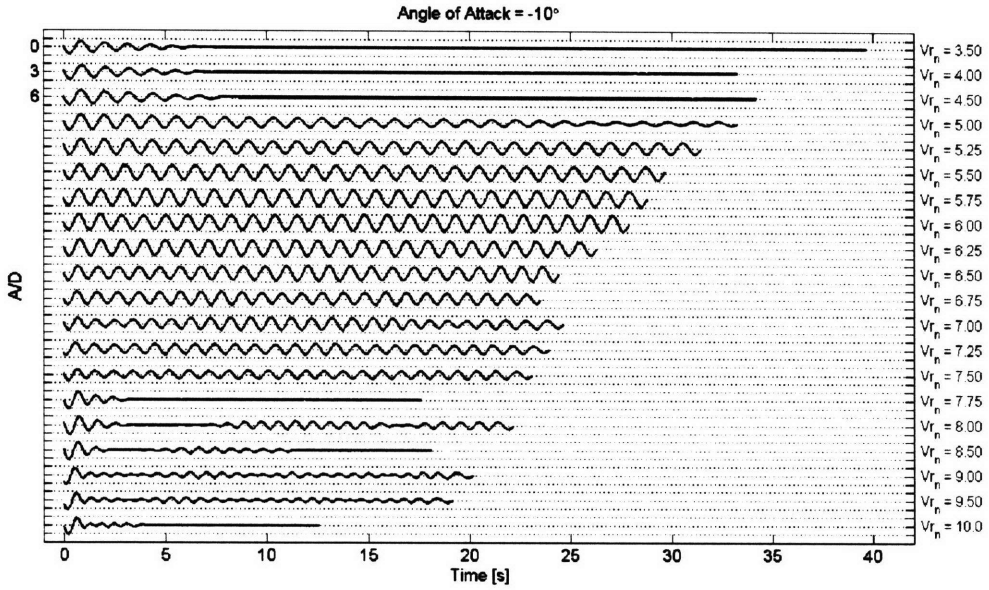

(a)

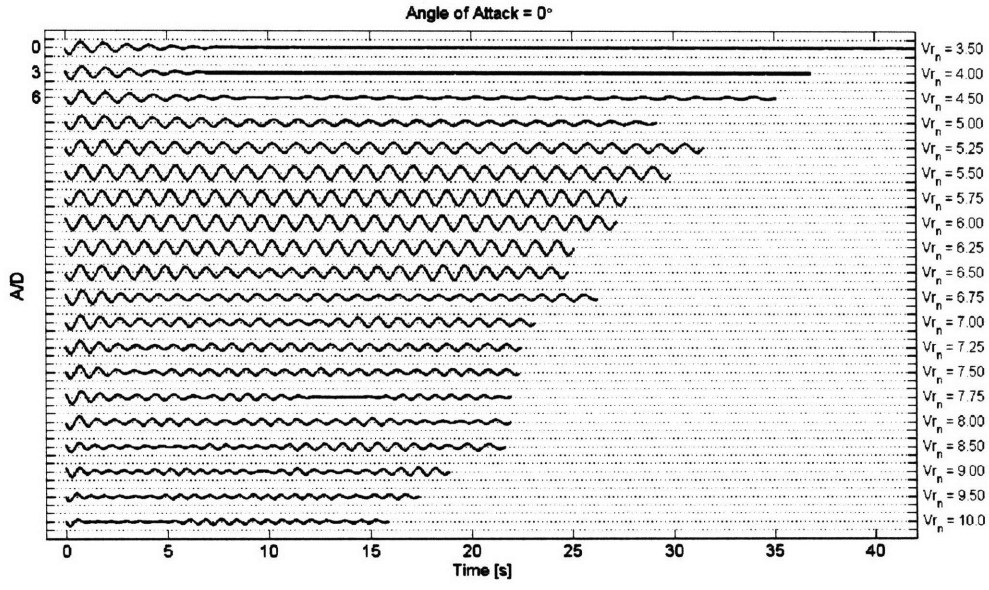

(b)

Figure D-3: Time traces of the oscillatory behavior exhibited by a cylinder modified with equilateral delta wings and angle of attack of (a) $-10°$ and $0°$.

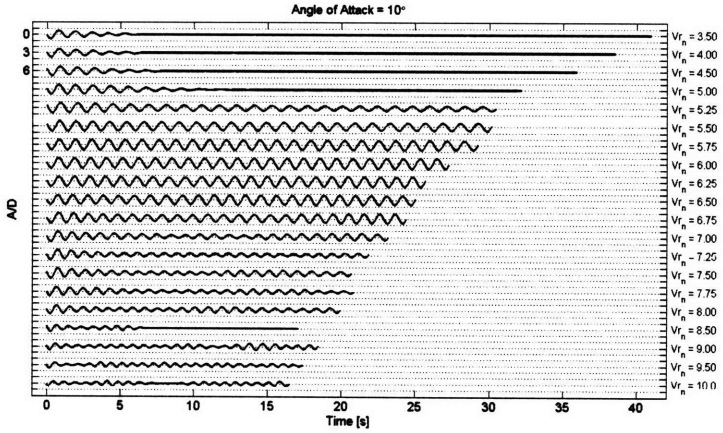

(a)

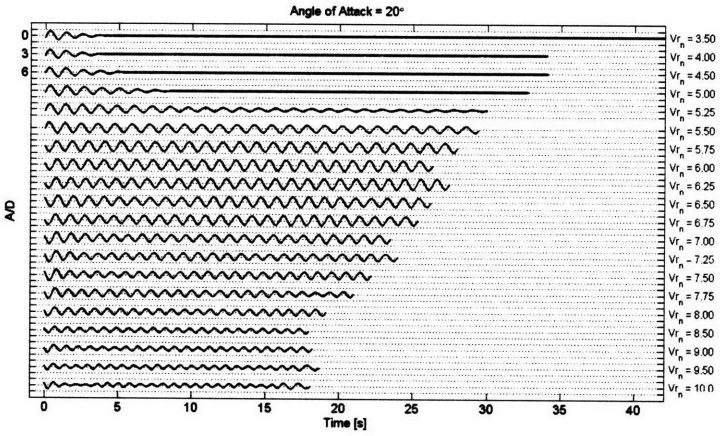

(b)

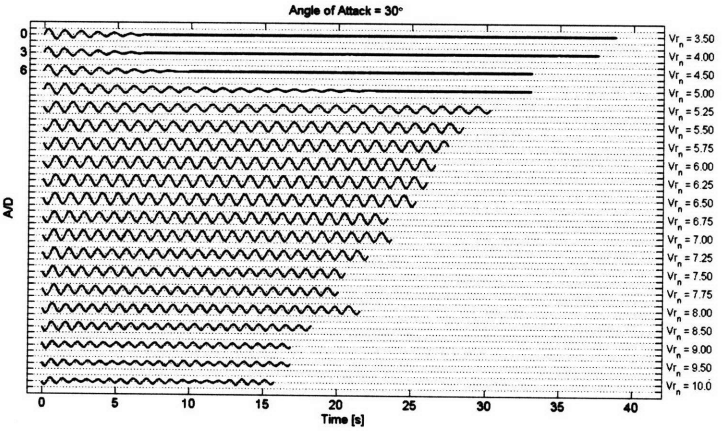

(c)

Figure D-4: Time traces of the oscillatory behavior exhibited by a cylinder modified with equilateral delta wings and angle of attack of (a) 10°, (b) 20° and (c) 30°.

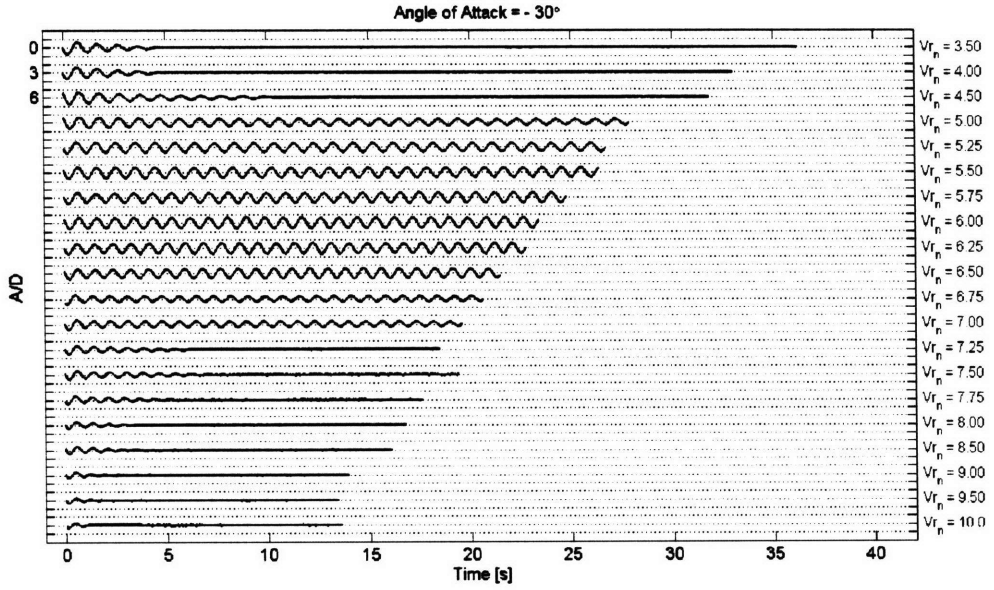

(a)

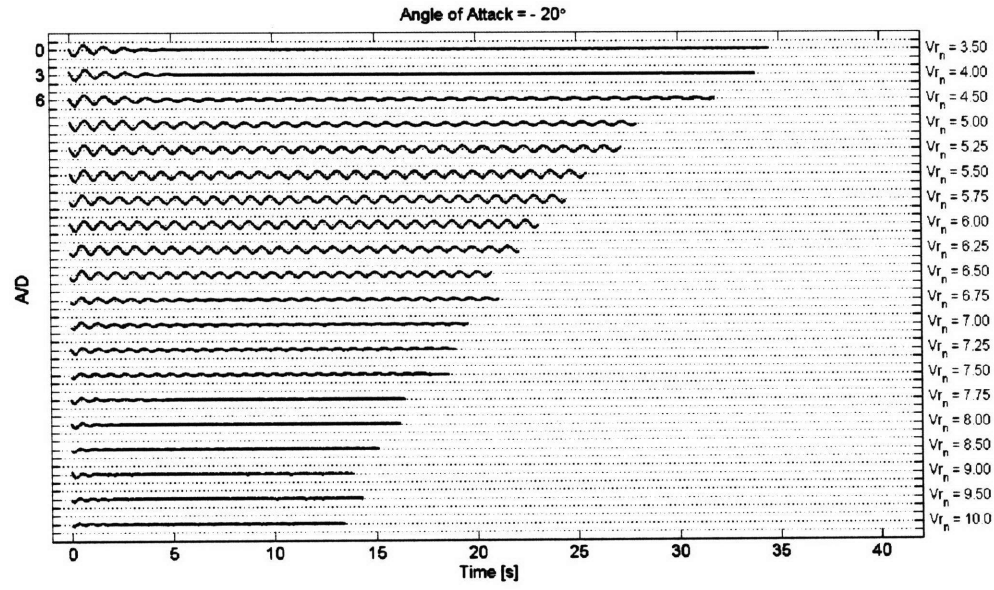

(b)

Figure D-5: Time traces of the oscillatory behavior exhibited by a cylinder modified with delta wings with a leading edge angle of 75° and angle of attack of (a) $-30°$ and (b) $-20°$.

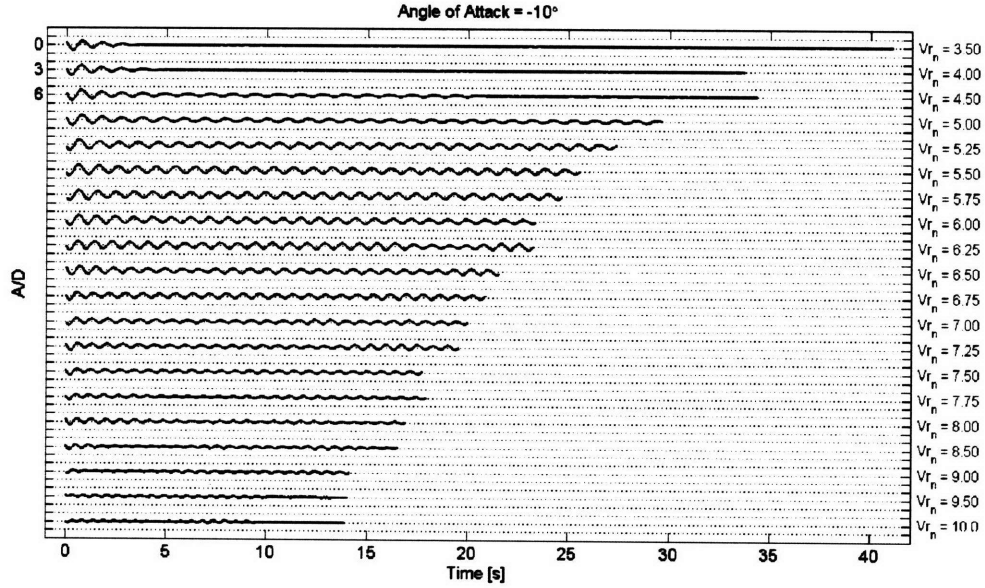

(a)

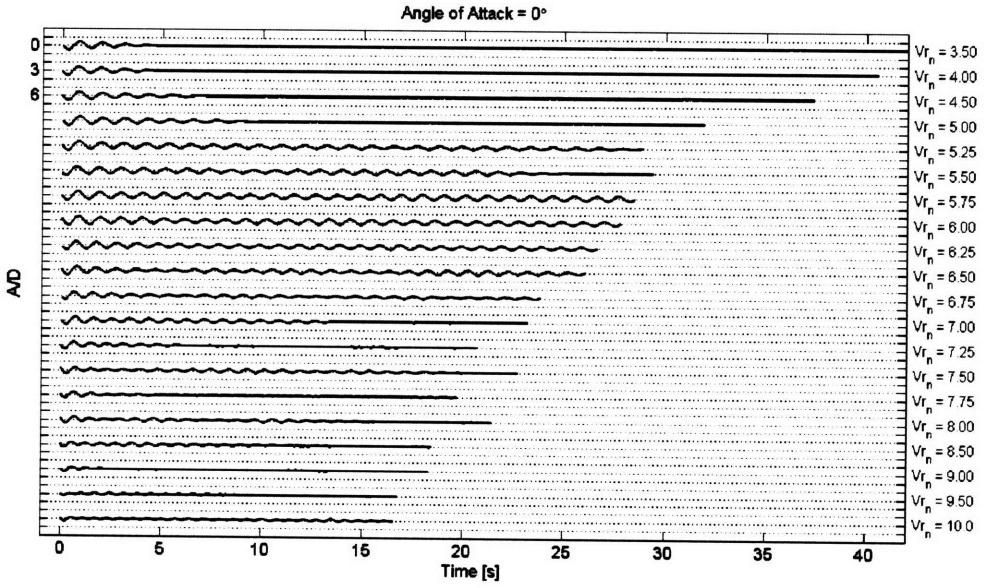

(b)

Figure D-6: Time traces of the oscillatory behavior exhibited by a cylinder modified with delta wings with a leading edge angle of 75° and angle of attack of (a) $-10°$ and $0°$.

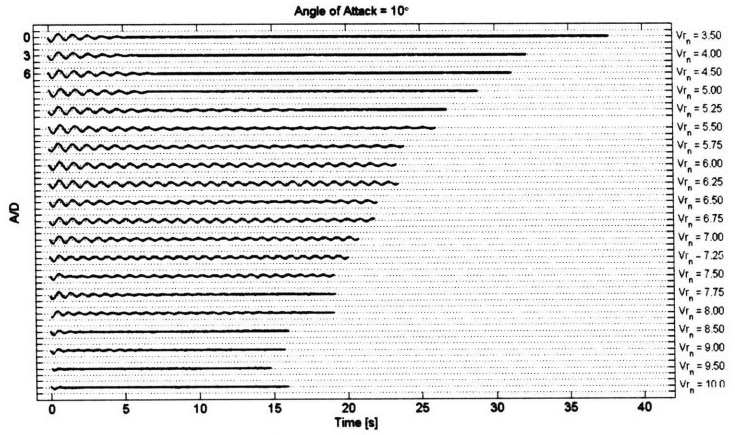

(a)

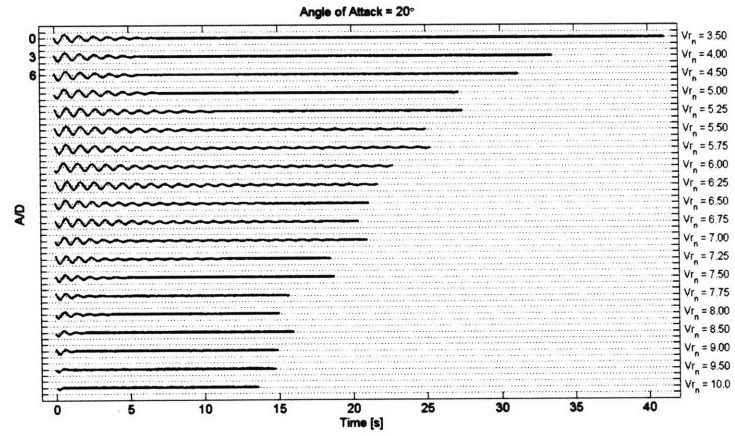

(b)

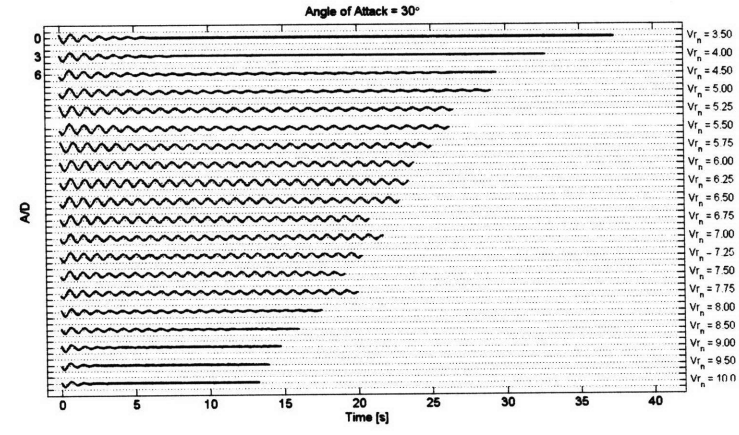

(c)

Figure D-7: Time traces of the oscillatory behavior exhibited by a cylinder modified with delta wings with a leading edge angle of 75° and angle of attack of (a) 10°, (b) 20° and (c) 30°.

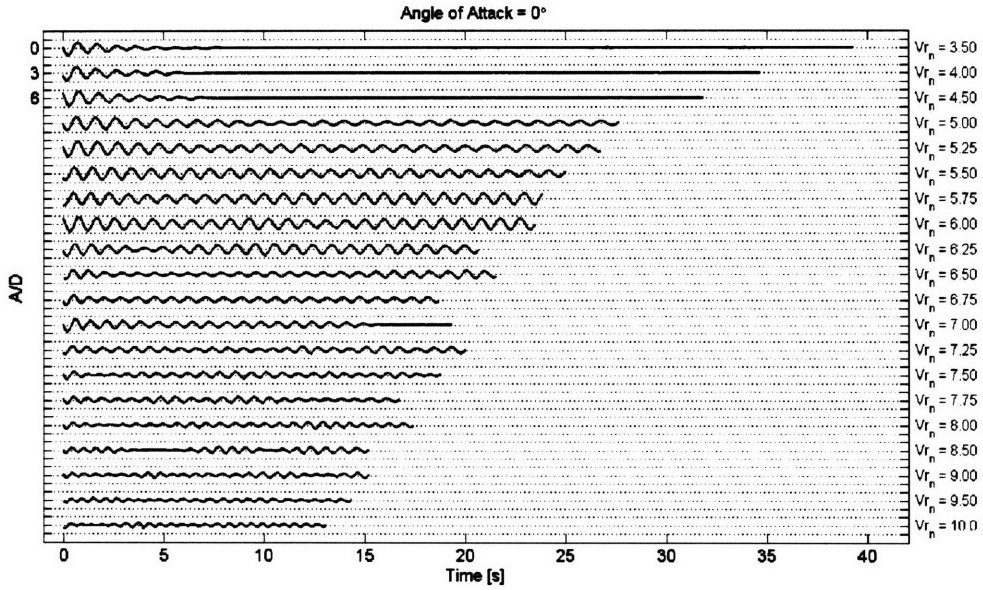

(a)

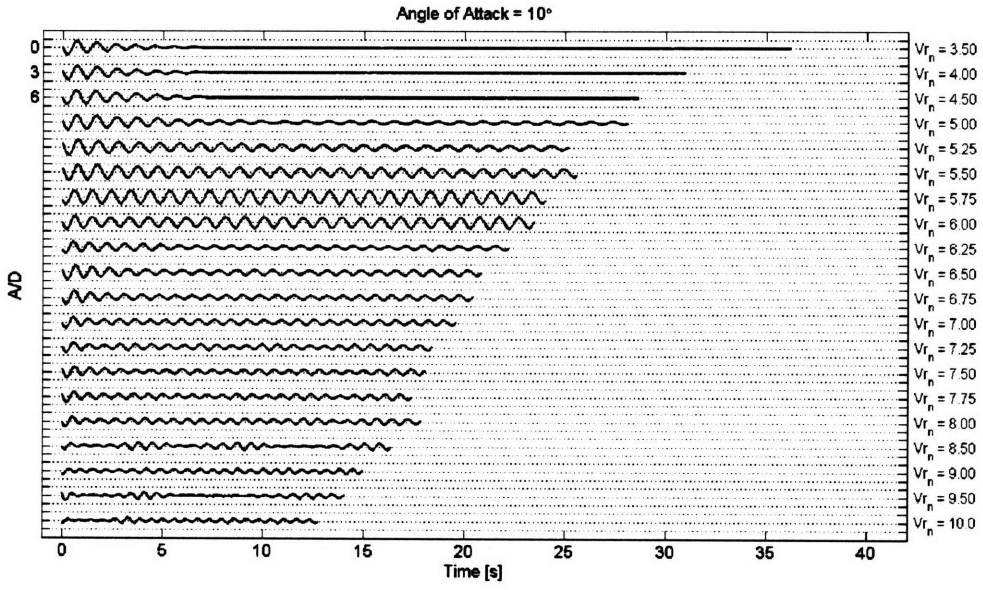

(b)

Figure D-8: Time traces of the oscillatory behavior exhibited by a cylinder modified with delta wings with a leading edge angle of 45°, trailing edge length of 1D and angle of attack of (a) 0° and 10°.

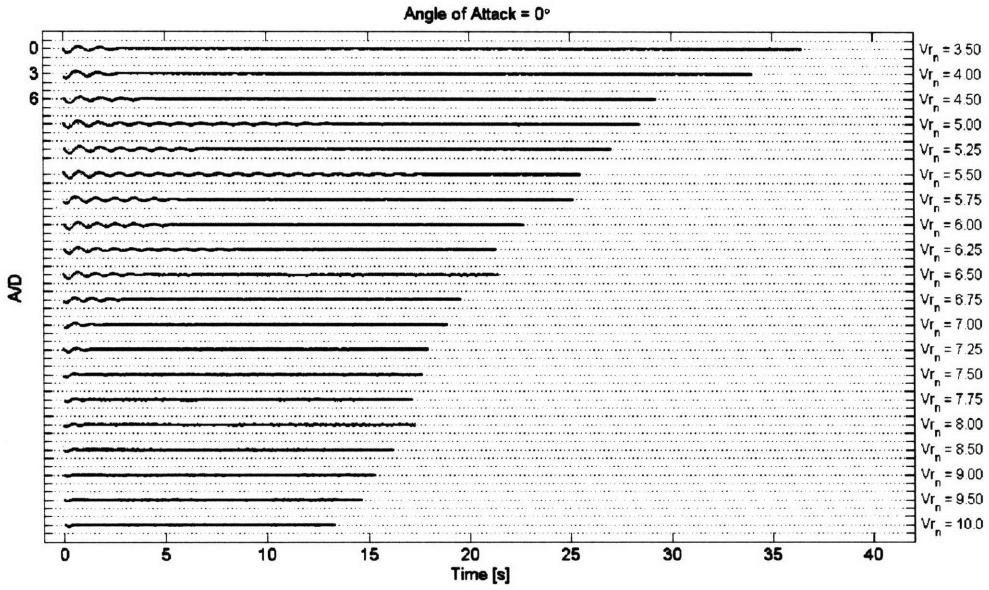

(a)

Figure D-9: Time traces of the oscillatory behavior exhibited by a cylinder modified with delta wings with a leading edge angle of 45°, trailing edge length of 2D and angle of attack of 0°.

Appendix E

Time Traces for Vortex Generating Tab Modified Cylinder

The transverse position over time for tests of a cylinder modified with the vortex generating tabs described in Chapter 5. The result for a bare cylinder is also provided for comparison purposes.

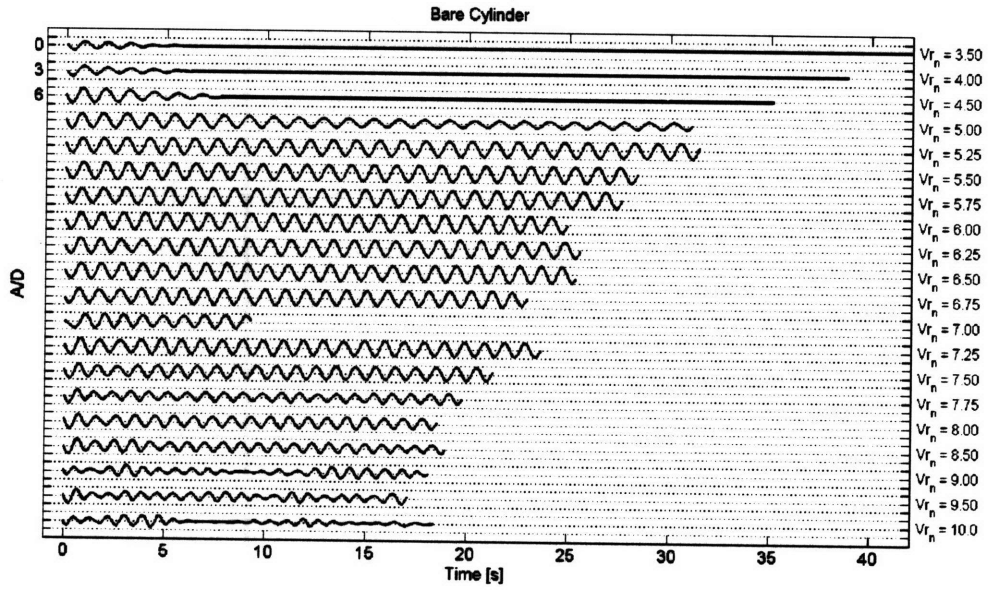

Figure E-1: Time traces of the oscillatory behavior exhibited by a bare cylinder.

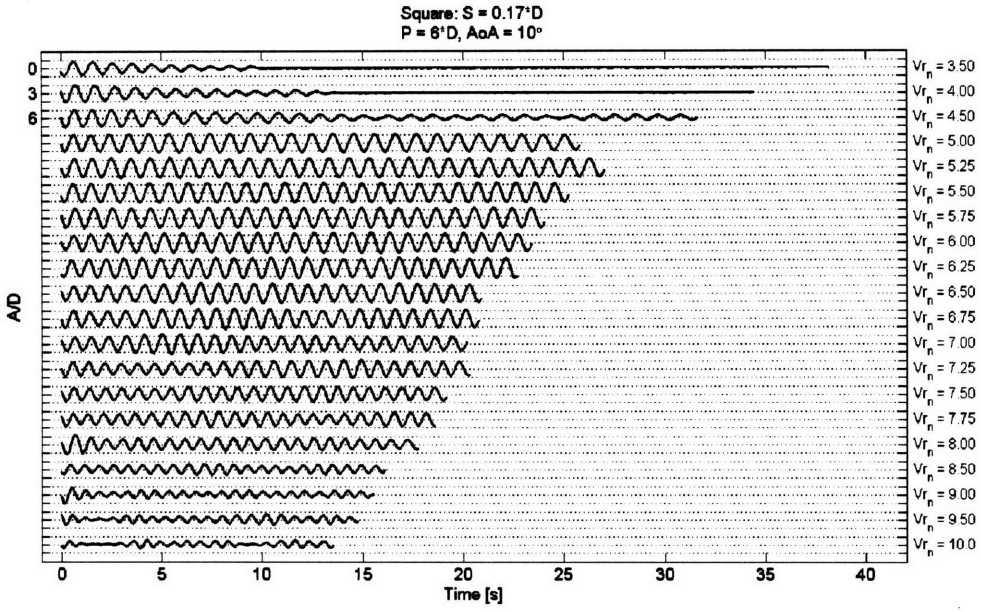

(a)

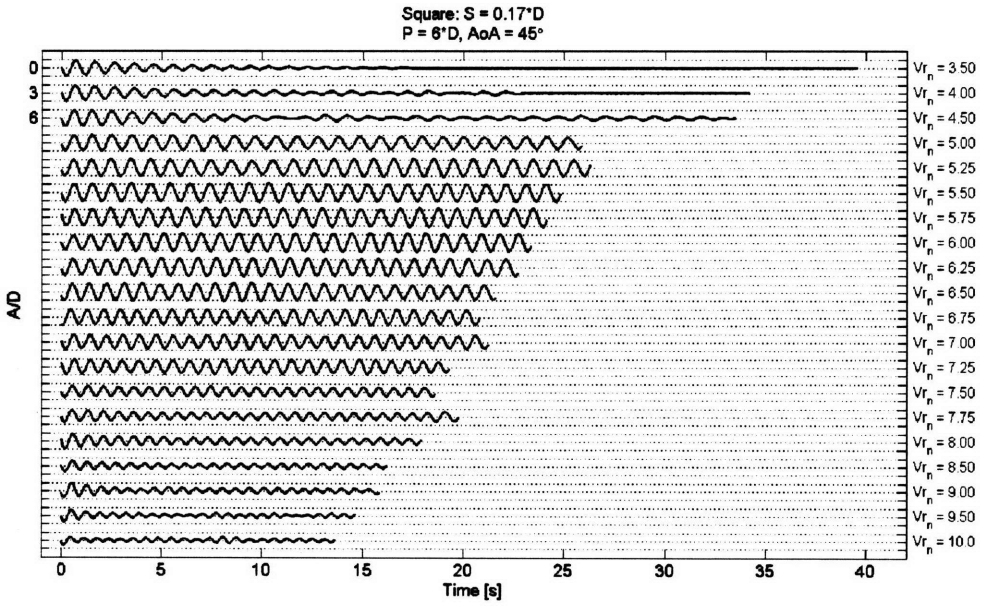

(b)

Figure E-2: Time traces of the oscillatory behavior exhibited by a cylinder modified with vortex generating tabs.

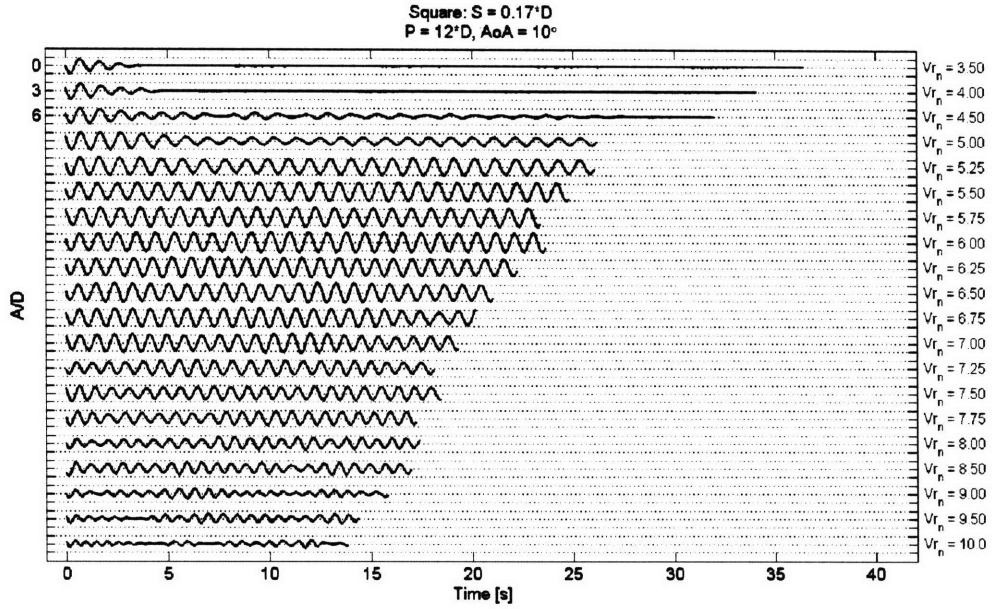

(a)

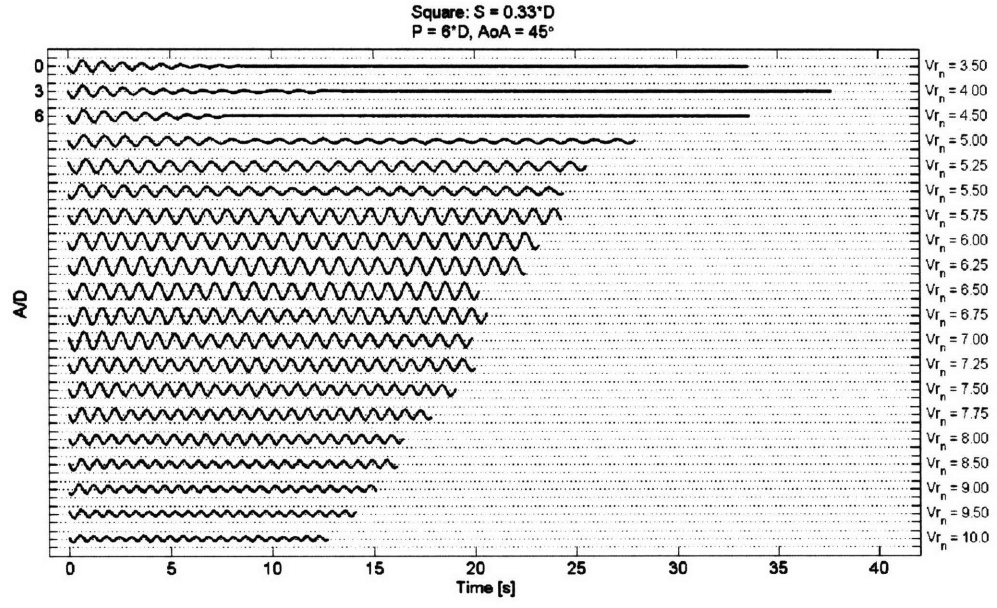

(b)

Figure E-3: Time traces of the oscillatory behavior exhibited by a cylinder modified with vortex generating tabs.

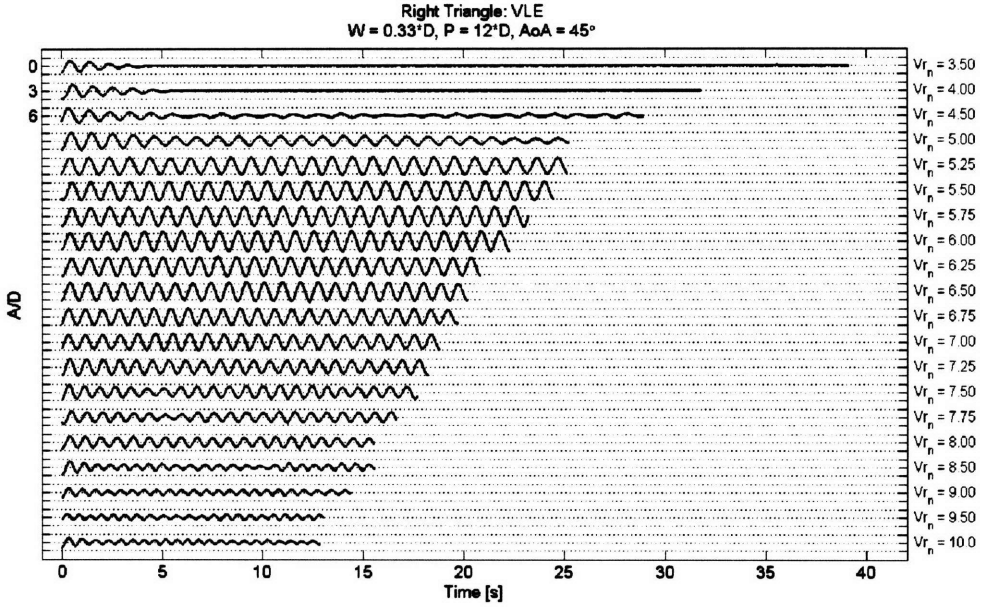

(a)

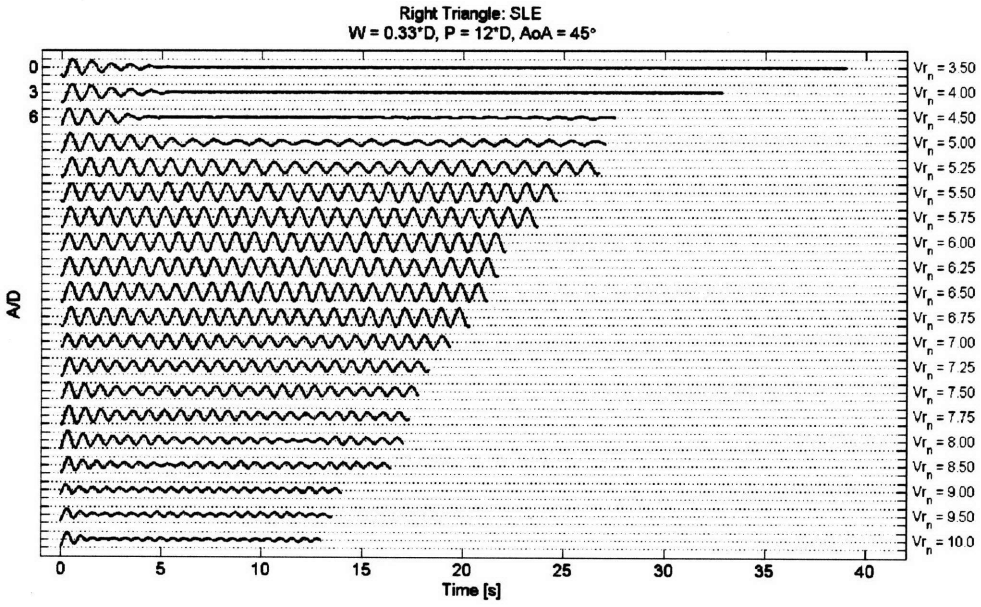

(b)

Figure E-4: Time traces of the oscillatory behavior exhibited by a cylinder modified with vortex generating tabs.

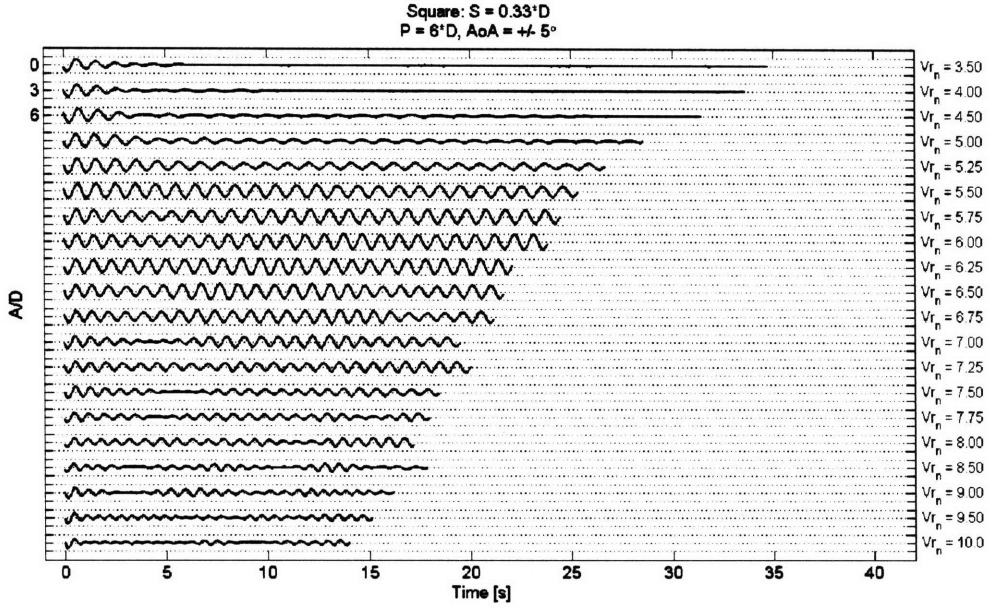

(a)

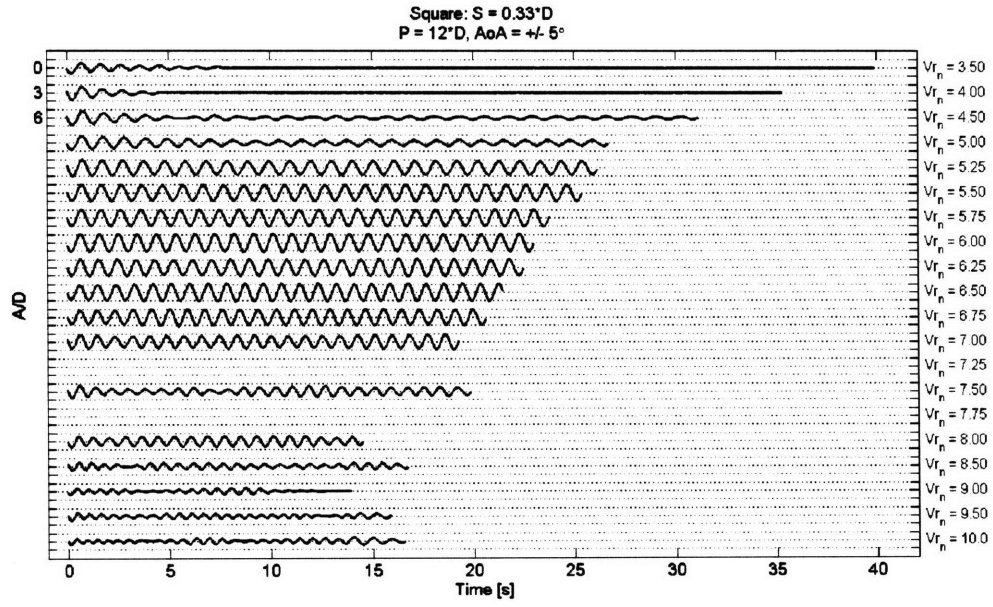

(b)

Figure E-5: Time traces of the oscillatory behavior exhibited by a cylinder modified with vortex generating tabs.

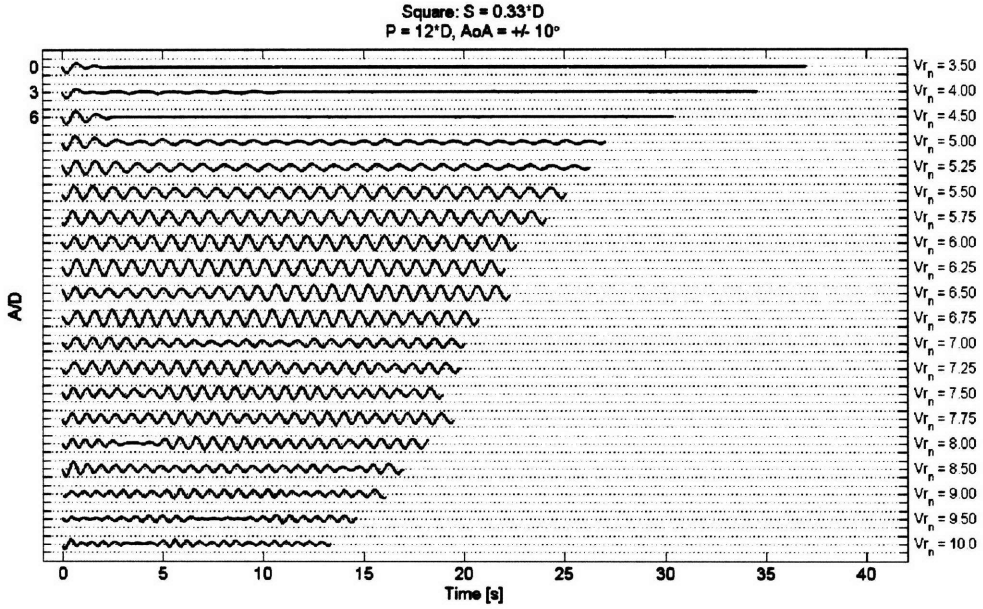

(a)

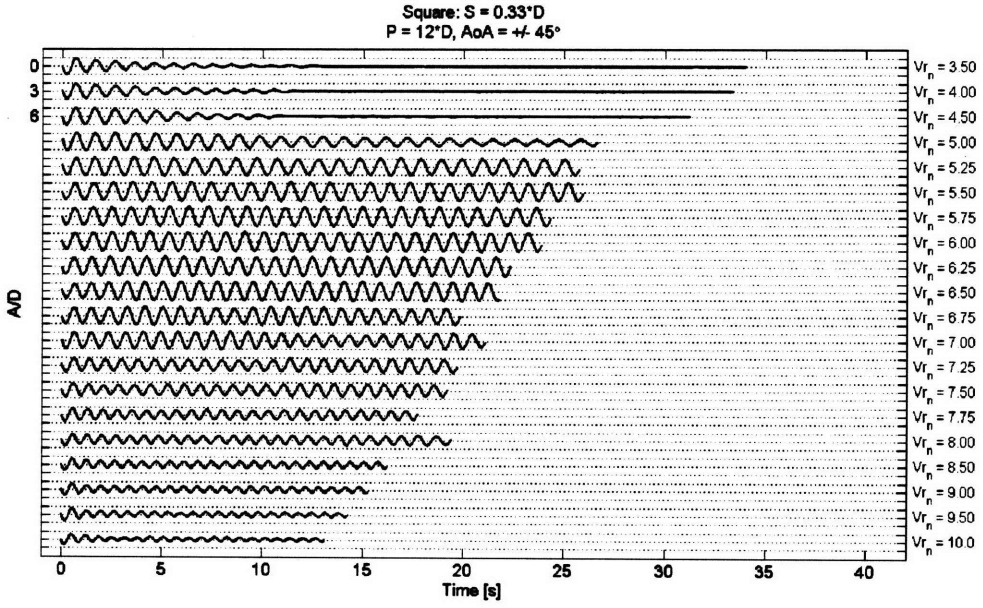

(b)

Figure E-6: Time traces of the oscillatory behavior exhibited by a cylinder modified with vortex generating tabs.

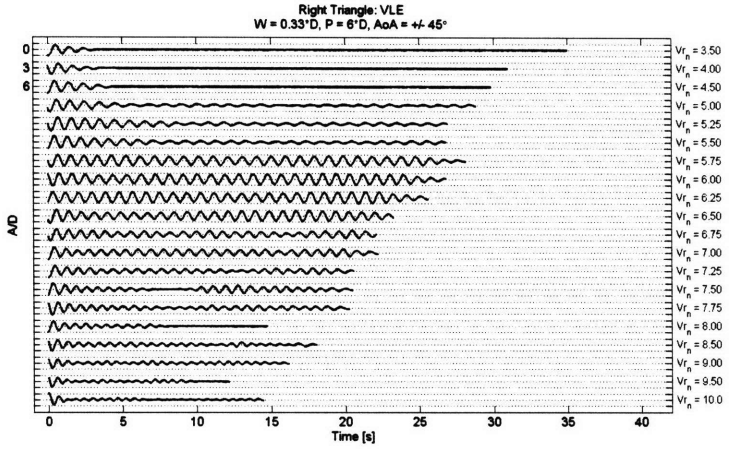

(a)

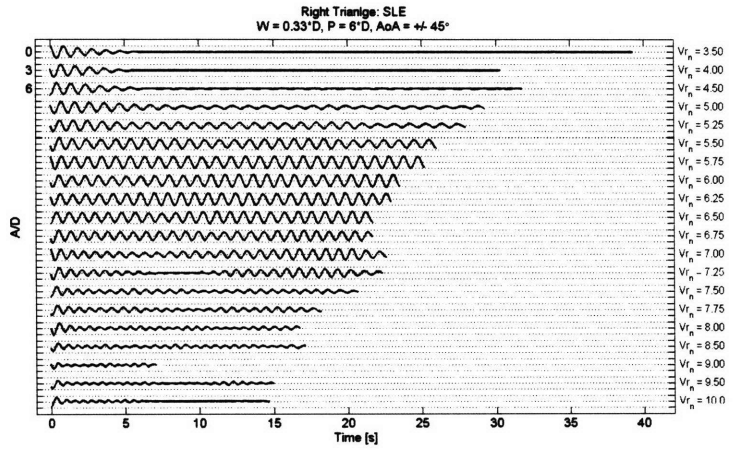

(b)

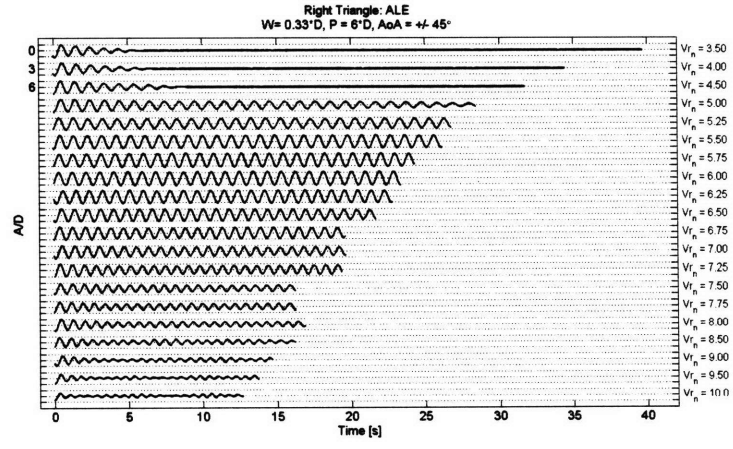

(c)

Figure E-7: Time traces of the oscillatory behavior exhibited by a cylinder modified with vortex generating tabs.

Appendix F

Time Traces for Vortex Generating Tab Modified Cylinder

The transverse position over time for tests of a cylinder modified with the "Rabbit Ear" configuration described in Chapter 4. The result for a bare cylinder is also provided for comparison purposes.

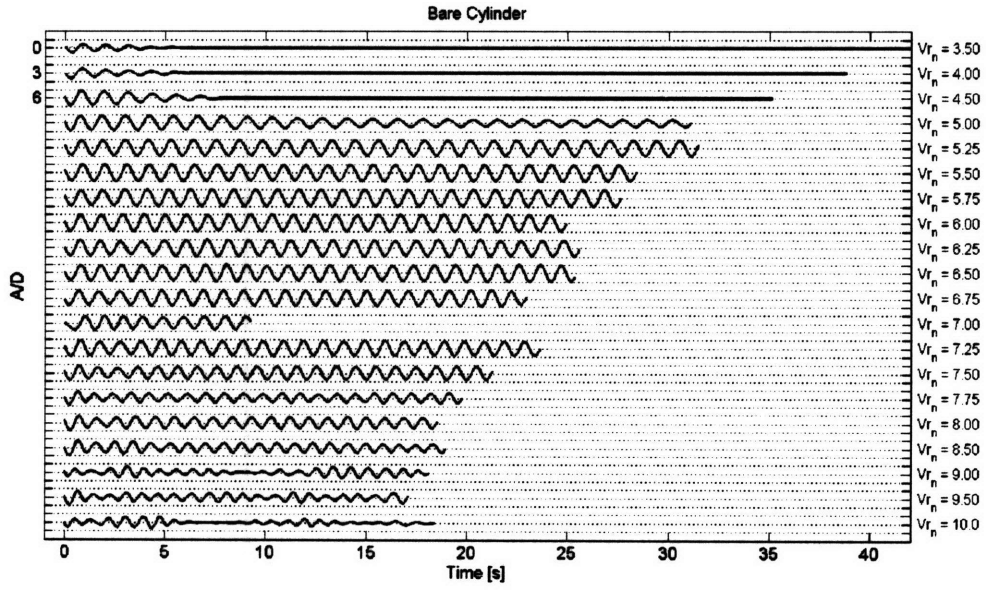

Figure F-1: Time traces of the oscillatory behavior exhibited by a bare cylinder.

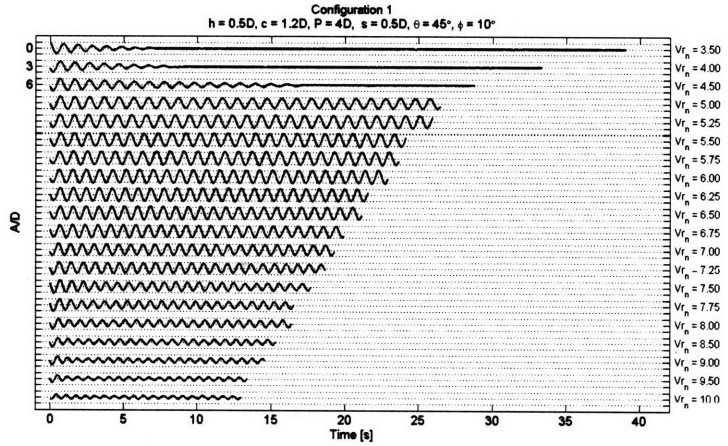

(a)

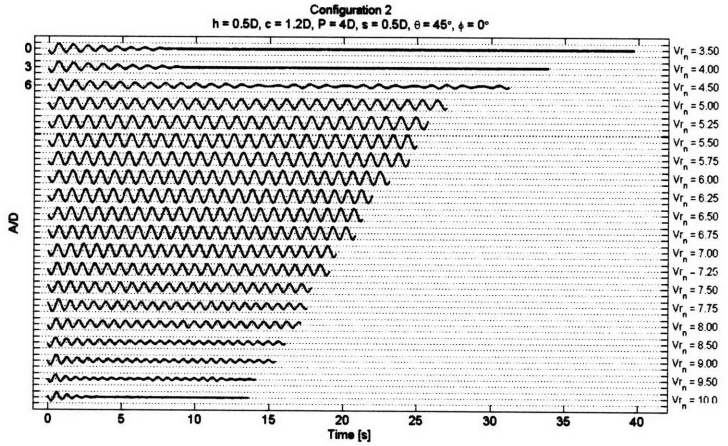

(b)

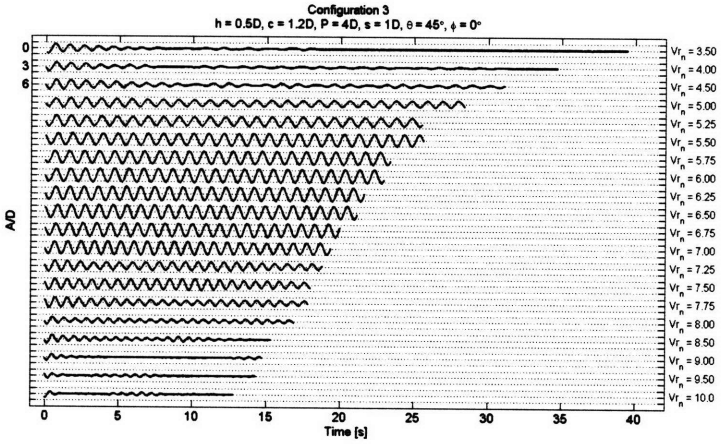

(c)

Figure F-2: Time traces of the oscillatory behavior exhibited by a cylinder modified with "Rabbit Ears".

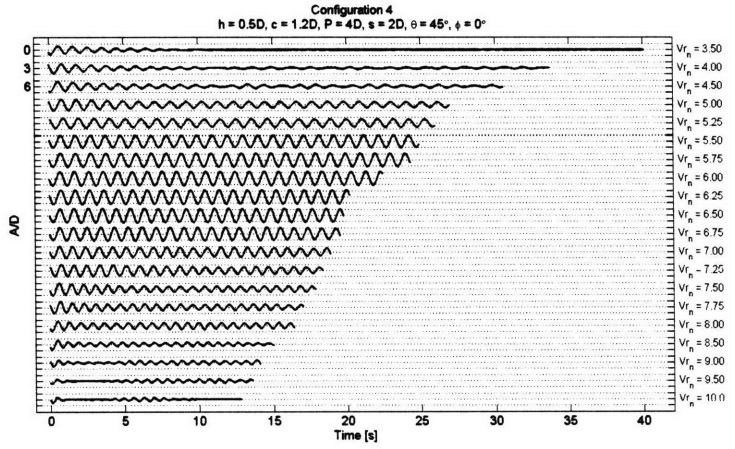

(a)

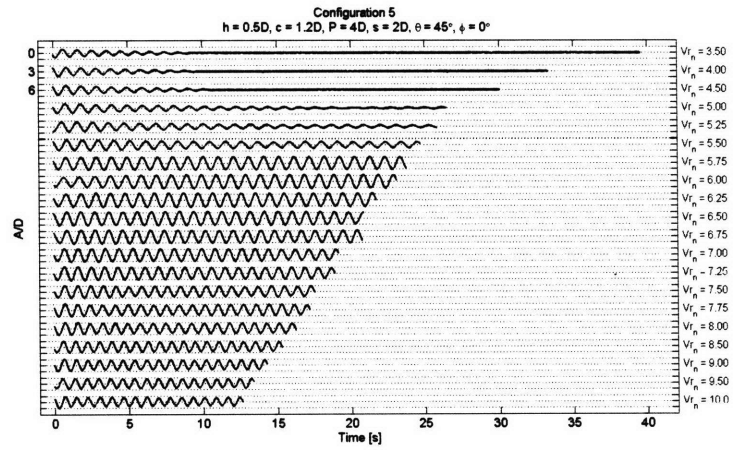

(b)

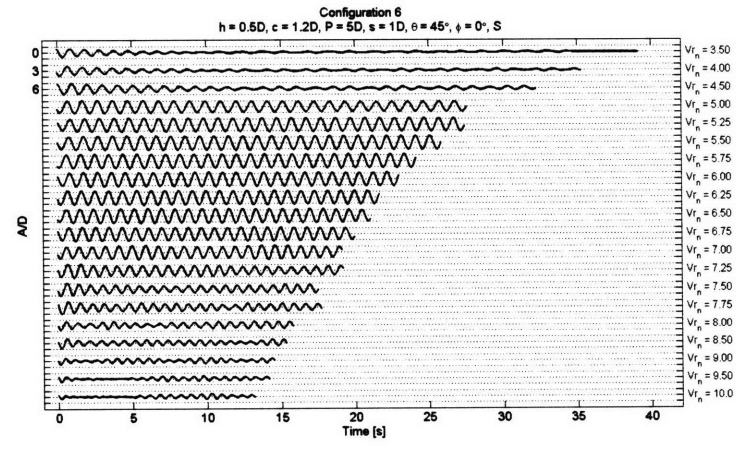

(c)

Figure F-3: Time traces of the oscillatory behavior exhibited by a cylinder modified with "Rabbit Ears".

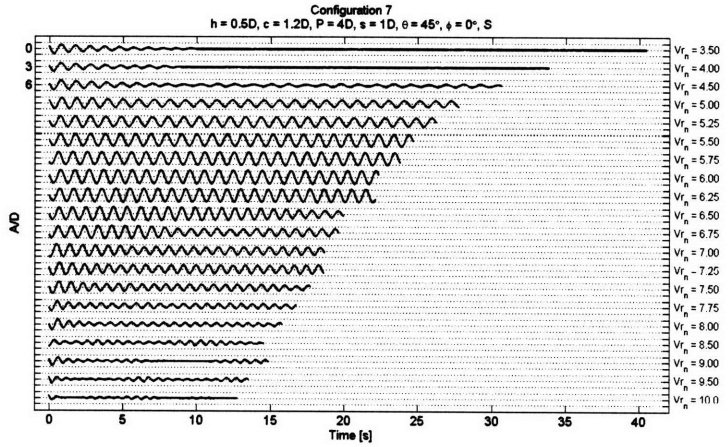

(a)

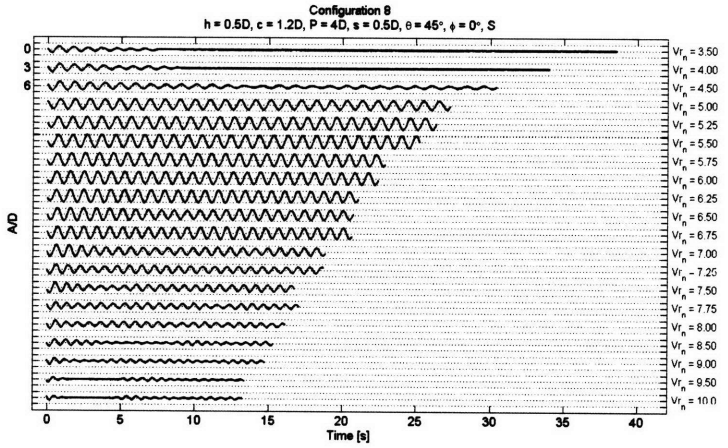

(b)

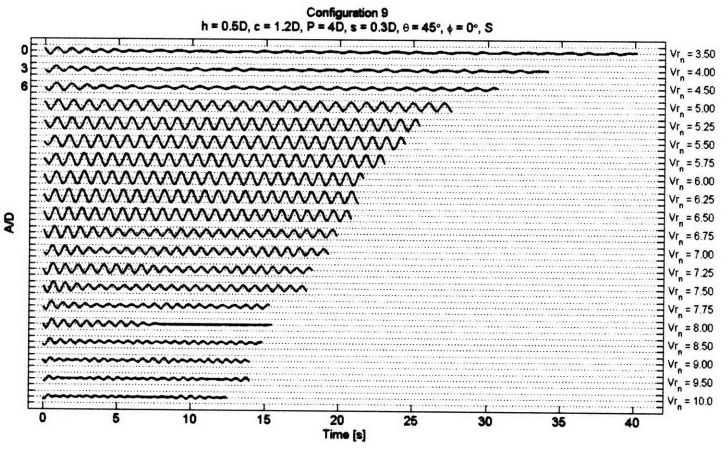

(c)

Figure F-4: Time traces of the oscillatory behavior exhibited by a cylinder modified with "Rabbit Ears".

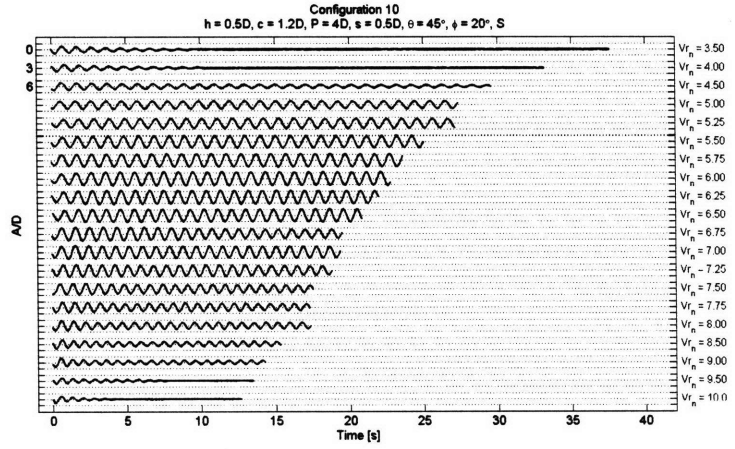

(a)

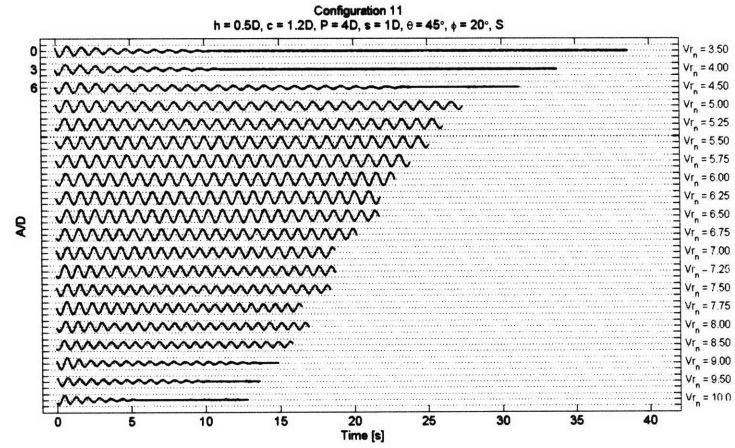

(b)

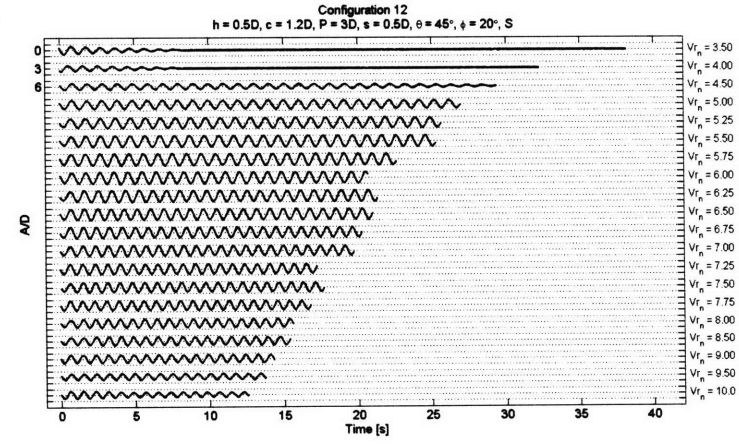

(c)

Figure F-5: Time traces of the oscillatory behavior exhibited by a cylinder modified with "Rabbit Ears".

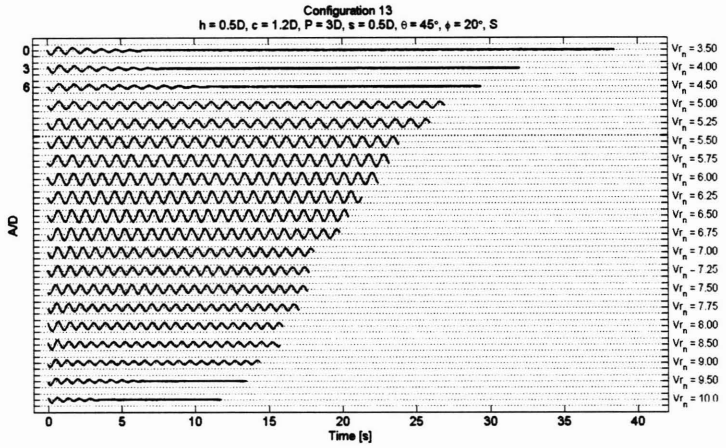

(a)

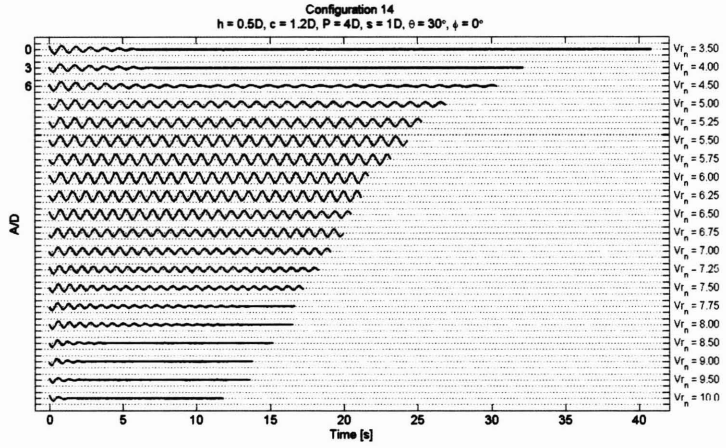

(b)

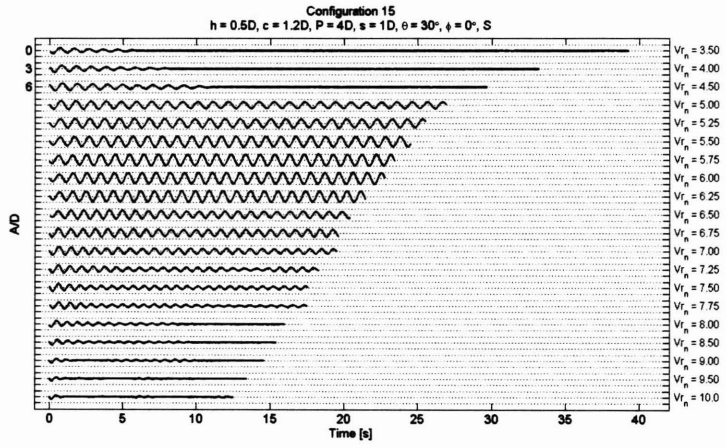

(c)

Figure F-6: Time traces of the oscillatory behavior exhibited by a cylinder modified with "Rabbit Ears".

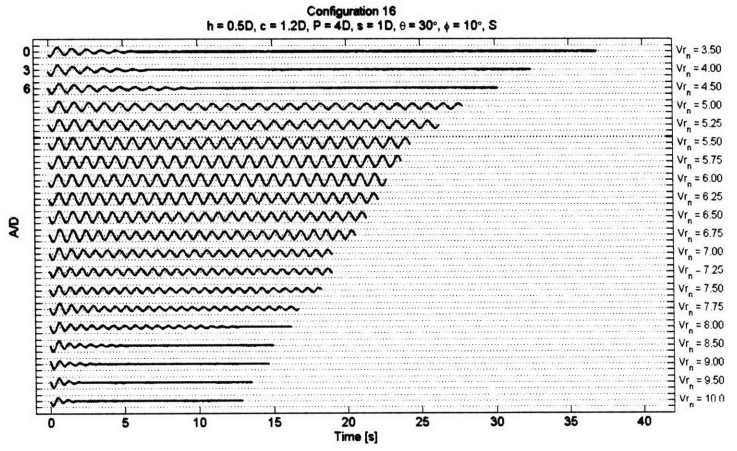

(a)

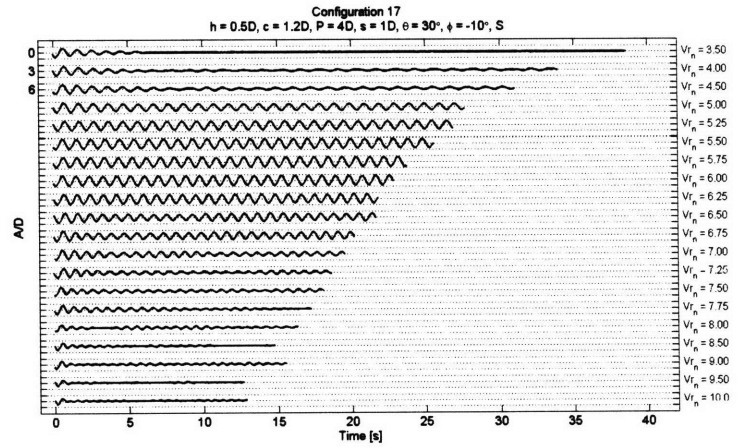

(b)

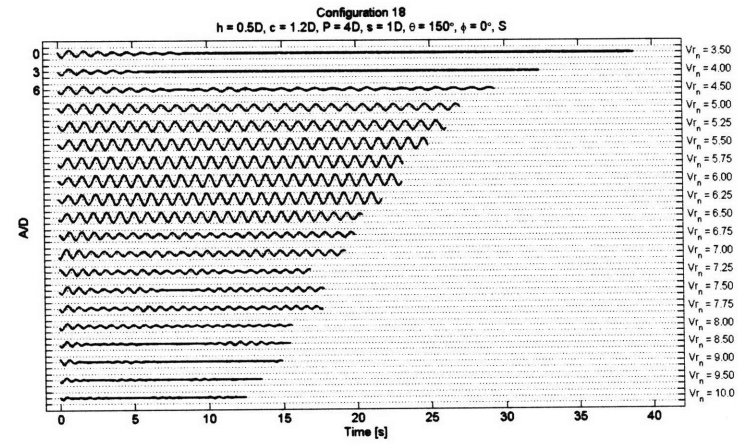

(c)

Figure F-7: Time traces of the oscillatory behavior exhibited by a cylinder modified with "Rabbit Ears".

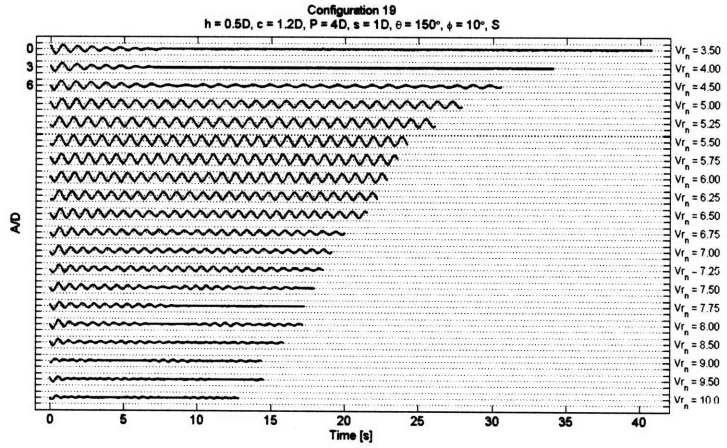

(a)

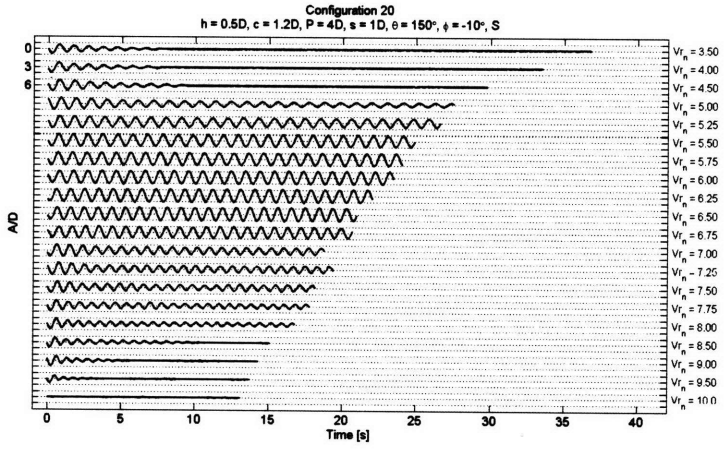

(b)

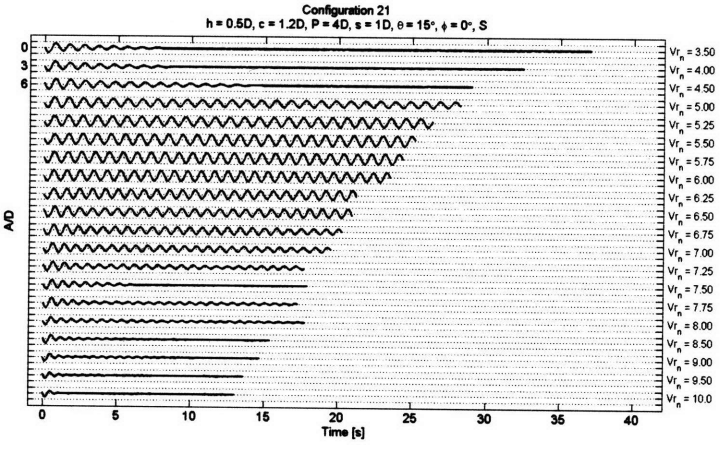

(c)

Figure F-8: Time traces of the oscillatory behavior exhibited by a cylinder modified with "Rabbit Ears".

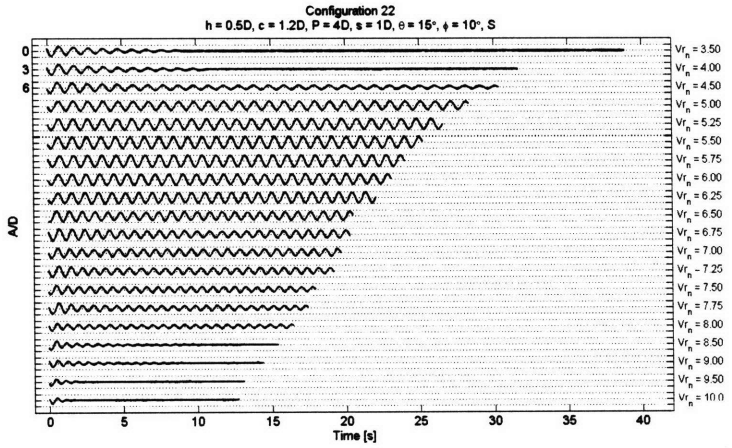

(a)

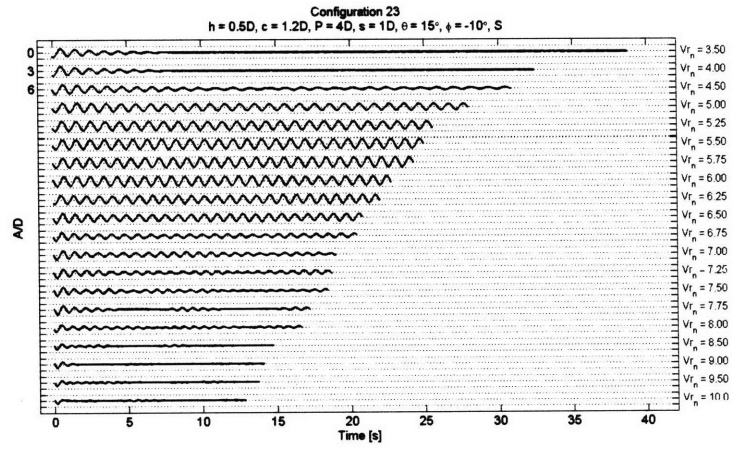

(b)

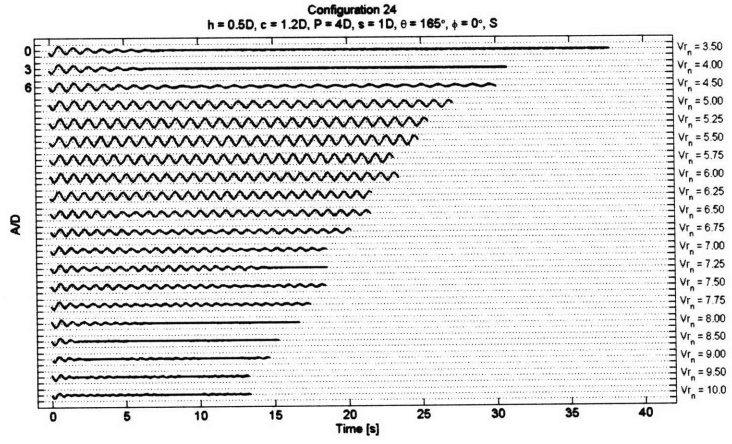

(c)

Figure F-9: Time traces of the oscillatory behavior exhibited by a cylinder modified with "Rabbit Ears".

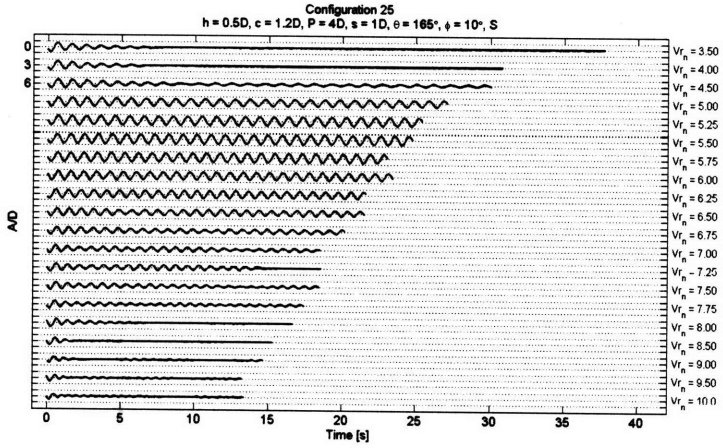

(a)

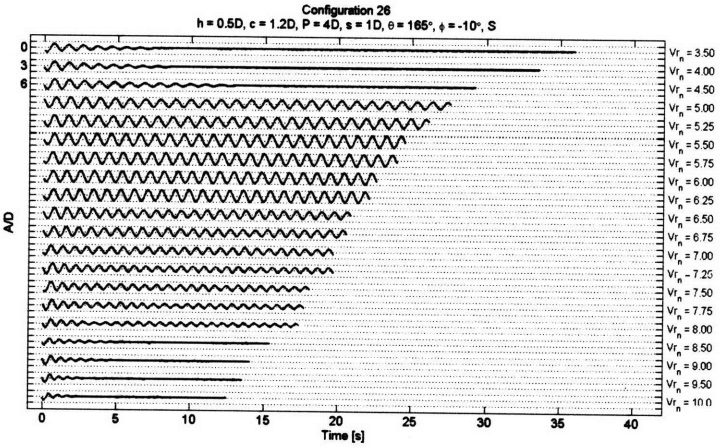

(b)

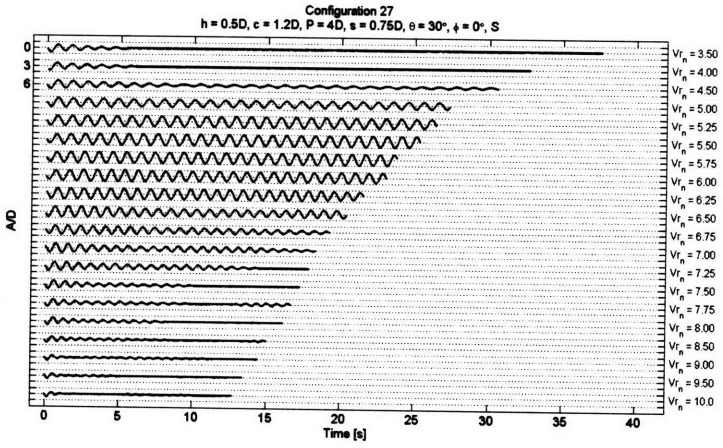

(c)

Figure F-10: Time traces of the oscillatory behavior exhibited by a cylinder modified with "Rabbit Ears".

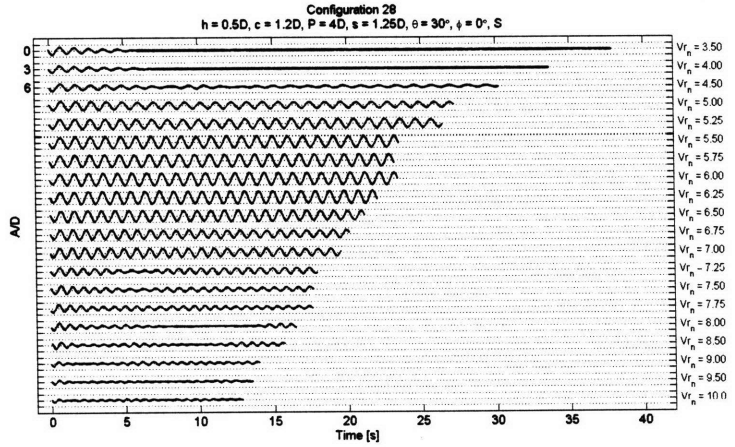

(a)

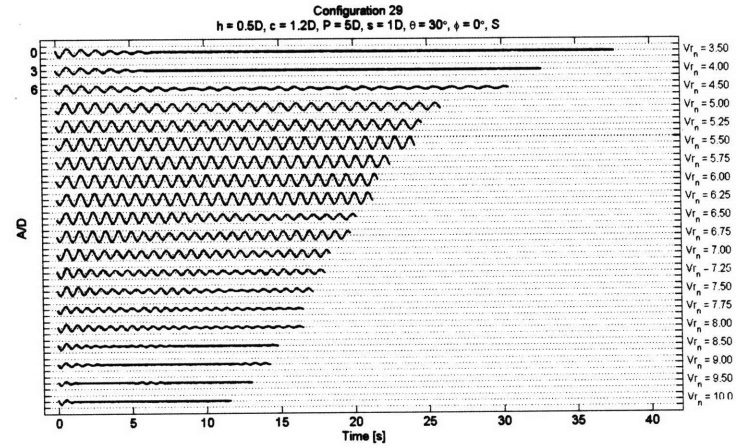

(b)

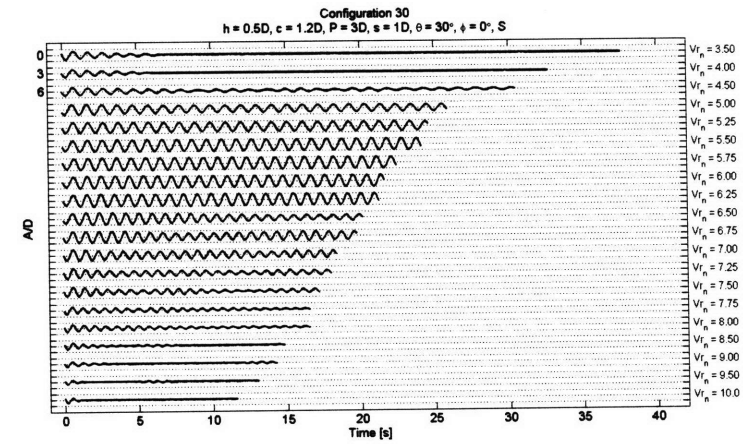

(c)

Figure F-11: Time traces of the oscillatory behavior exhibited by a cylinder modified with "Rabbit Ears".

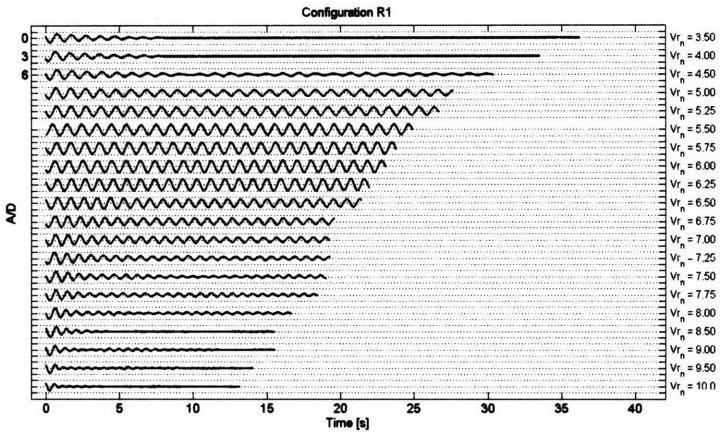

(a)

Figure F-12: Time traces of the oscillatory behavior exhibited by a cylinder modified with "Rabbit Ears".